

## ABSTRACT

Title of Dissertation: THE ATTACHMENT AND  
CHARACTERIZATION OF DNA PROBES ON  
GaAs-BASED SEMICONDUCTOR SURFACES

JoonHyuk Yang, Doctor of Philosophy, 2007

Dissertation directed By: Professor Mohamad I. Al-Sheikhly, and  
Professor Lourdes Salamanca-Riba  
Department of Materials Science and Engineering

Immobilization of nucleic acid molecules on solid surfaces is the core of numerous important technologies in the genomics, disease diagnostics and biosensors applications. The architecture and density of immobilized probe molecules depend on the type of the solid surface on which they are anchored. Even though many different types of surfaces have been studied as substrates for deoxyribonucleic acid (DNA) attachment, the development of a new type of substrate, which is reproducible, stable, highly controlled and easily transferred to practical applications, is still needed. Recent studies have shown that As terminated GaAs-based semiconductors can be used as substrates for immobilized DNA layers.

In this study, I aim to understand the attachment of nucleic acid onto the surfaces of As-terminated GaAs- based semiconductors and focus on improving the “brush-structure”, which is essential for high quality of biochip based on a DNA layer. Attachment of 8-base and 100-base thiolated ssDNA layers on arsenic terminated GaAs(001) was achieved and characterized. The covalent bonds between the thiolated oligonucleotides with As atoms on the GaAs surface were investigated using x-ray photoelectron spectroscopy (XPS), and the surface morphology was obtained using atomic force microscopy (AFM) and field emission scanning electron microscopy (FESEM). In addition, I studied the effect of DNA length and the presence of a good solvent, such as water, on the oligonucleotides on a GaAs surface. I also investigated the effects of the thiol-based spacer and electrolyte concentration to improve the brush-like structure of the DNA layer. Finally, irradiation effects and AlGaAs resonators have been studied for the applications of DNA brush layer on GaAs as biosensor during the change of attachment probe DNA and hybridization to target DNA.

For the 8-base thiolated ssDNA case, AFM results showed that the layer thickness was about ~2.2 nm in dry mode and increased in wet mode. Replacement reaction from N- , O- As bonds to S-As bonds was observed with addition of MCH as indicated by analysis of XPS spectra. The concentration of electrolyte affected the brush like layer structure. In the case of the longer, more flexible DNA with 100 bases, the DNA molecules strongly interacted with each other and formed big cluster, of 330~440nm in diameter on the surface. Finally, for the applications, a high level of

radiation destroyed the brush layer. An AlGaAs resonator used as proof of concept a change in mass by a change in resonance frequency under hybridization reaction with complementary target DNA. This result shows that the design is viable and has a deflection of  $\sim 25\text{pg}$ .



THE ATTACHMENT AND CHARACTERIZATION OF DNA PROBES ON  
GaAs-BASED SEMICONDUCTOR SURFACES

By

JoonHyuk Yang

Dissertation submitted to the Faculty of the Graduate School of the  
University of Maryland, College Park, in partial fulfillment  
of the requirements for the degree of  
Doctor of Philosophy  
2007

Advisory Committee:

Professor Mohamad Al-Sheikhly, Chair / Advisor  
Professor Lourdes Salamanca-Riba, Co-Advisor  
Professor Emeritus Joseph Silverman  
Professor Aaron Barkatt  
Associate Professor Don DeVoe

© Copyright by  
JoonHyuk Yang  
2007

## Acknowledgements

I would like to express my gratitude to the many people whose support and assistance enabled me to complete my dissertation.

I'm deeply grateful to Dr. Mohamad Al-Sheikhly for his tremendous commitment, support, and patience not only during the dissertation phase but throughout the Ph.D. process. Without his guidance, I could not have achieved such a goal. Special thanks are due to Dr. Lourdes Salamanca-Riba for giving me an incredible guidance and for her incessant encouragement. I sincerely thank Dr. Joseph Silverman for providing valuable comments and insights. I would also like to extend my thanks to Dr. Aaron Barkatt and Dr. Don DeVoe for their helpful suggestions.

I thank my fellow doctoral students for their support throughout my graduate school experience, helping me to believe in myself despite difficulties along the way. I also wish to thank Mr. Tim Zhang who is an engineer in Microanalysis center for many technical supports.

I would like to express my heartfelt thanks to my parents and brother, without their support and encouragement this long journey would not have been possible. Finally, I truly thank especially my wife, Soojung Kim, and my daughter, Jennifer, for their unconditional love and patience.

# Table of Contents

Abstract	
Acknowledgements.....	ii
List of Tables.....	v
List of Figures.....	vi
List of Abbreviations.....	xiv
Chemical Nomenclature.....	xv
Greek Letters.....	xv
Chapter 1 Introduction and Background.....	1
1.1 Overview.....	1
1.2 Polymer Brush Structure on Planar surface and the Effects of Electrolytes.....	5
1.2.1 Tethered Neutral Polymer Chains on Planar Surface.....	6
1.2.2 Tethered Polyelectrolyte Chains on Planar Surface.....	14
1.3 DNA monolayer.....	22
1.4 Immobilization of DNA onto Solid Surface.....	23
1.4.1 Immobilization of Thiolated DNA on Gold Surface.....	25
1.4.2 Immobilization of DNA on Siliceous Substrate.....	26
1.4.3 Immobilization of Thiolated DNA by Covalent Bonding on GaAs-based Semiconductors.....	26
1.5 DNA Hybridization.....	30
1.6 Applications using Immobilization of DNA.....	33
1.6.1 Electrochemical Biosensor.....	33
1.6.2 Optical Biosensor.....	34
1.6.3 Piezoelectric Biosensor.....	36
Chapter 2. Experimental Approach.....	40
2.1 Materials and Sample Preparation.....	40
2.2 Characterization Techniques.....	41
2.2.1 Atomic Force Microscopy (AFM).....	41
2.2.2 X-ray Photoelectron Spectroscopy (XPS).....	44
2.2.3 Field Emission Scanning Electron Microscopy (FESEM).....	48
2.2.4 Grazing Incidence X-ray Scattering.....	48
2.3 Linear Accelerator Facilities.....	49
Chapter 3. Immobilization of Oligonucleotides on GaAs Surface.....	51
3.1 Introduction.....	51
3.2 Experimental Materials.....	53
3.3 Thiol Modification Effects for Immobilization.....	55
3.3.1 Attachment of Non-Modified DNA.....	55
3.3.2 Attachment of Thiol-Modified DNA.....	60
3.3.2.1 Sonication Cleaning Method.....	61

3.4 Spacer Effects to Immobilization DNA layer on GaAs Surface.....	68
3.5 Effects of DNA and MCH Concentration on the Immobilization of a DNA layer on GaAs Surface .....	80
3.6 Environmental Effects on Immobilization of DNA layer on GaAs Surface.....	83
3.7 Electrolytes Effects on Immobilization of DNA layer on GaAs Surface.....	88
3.8 Attachment of Longer Oligonucleotides on GaAs Surface.....	94
Chapter 4. Toward Development of DNA Biosensors.....	102
4.1 Introduction.....	102
4.2 Effects of Irradiation on an Immobilization DNA layer on GaAs.....	103
4.3 AlGaAs Resonator Biosensor.....	107
4.3.1 Introduction.....	107
4.3.2 Detection of Hybridization Using AlGaAs Resonator.....	109
Chapter 5. Discussion and summary.....	112
Chapter 6. Suggestions for Future Work.....	118
Appendices.....	121
References.....	128

## List of Tables

Table 3.1	Sequences of oligonucleotides.....	54
Table 3.2	Statistical measurements of ssDNA probe dimensions.....	93
Table A.1	Quantification report before (a) and after (b) immersion acetone for 30 minutes of the immobilized 8-base ssDNA (60 $\mu$ M) layer on GaAs substrate.....	125

## List of Figures

Figure 1.1	Schematic of tethered neutral polymer chains on a planar surface. $L$ is the layer thickness, $d$ is the average spacing between neighbor tethered points, and $\epsilon$ is the blob size. The graph shows the monomer density, $\rho$ , as a function of distance, $z$ , from the surface.[1] .....8	8
Figure 1.2	Mushroom regime and brush regime of tethered polymer layer.[2]...11	11
Figure 1.3	Schematic representation of two different regimes for polyelectrolyte brush: (a) osmotic regime ( $L \geq \xi$ ) and (b) charged regime ( $L < \xi$ ) [2].....16	16
Figure 1.4	Logarithm dependence of the osmotic pressure between two identical polyelectrolyte brushes plotted as a function of the surface separation normalized to the brush height for fully extended chains. The filled squares are for no added electrolyte while the open squares are for 5mM monovalent salt. The pressure is in arbitrary units. The parameters used for this calculation are $L_0 = 10^4 \text{ \AA}$ , $d = 10^3 \text{ \AA}$ , and $f = 1$ [2].....21.	21.
Figure 1.5	The schematic of immobilization of probes and hybridization with target strands.....24	24
Figure 1.6	DNA immobilization (i) silanization of the solid support with APTES, (ii) reaction of cross linker (PMPI, MBS, or sulfo-MBS) with APTES	

	to generate a maleimide surface, and (iii) reaction of thiol end-groups on DNA with surface maleimides.....	27
Figure 1.7	(a) simulated STM image of the (2x4) reconstructed surface of As-terminated GaAs using a filled-state bias of 0.3 V below the valence band maximum; (b) structural model of the reconstructed surface; (c) height cross-section across a dimer trench along the [1 1 0] direction[68].....	29
Figure 1.8	(a) The primary structure of DNA (b) complementary hydrogen bonded base-pairs as proposed by Watson and Crick(c), (d) a schematic representation of DNA hybridization and denaturation.[3] .....	32
Figure 1.9	The schematic of Surface Plasmon Resonance biosensor [92].....	35
Figure 1.10	Quartz Crystal Microbalance (QCM) [102].....	38
Figure 1.11	The SEM images of the different types of AlGaAs resonator used in this work.....	39
Figure 2.1	Schematic of Atomic Force Microscopy.....	42
Figure 2.2	X-ray excite core shell electrons.....	45
Figure 2.3	XPS spectrum of C 1s with curve fitting.....	47
Figure 2.4	Top schematic of Major Fictional Components of a Varian Linear Electron Beam Accelerator (LINAC) (bottom) at the University of Maryland.....	50
Figure 3.1.	Schematic of tightly packed monolayer of long-chain thiol molecules on Au (111) [21].....	52

Figure 3.2	AFM images of the bare GaAs (001) plane surface (500 nm X 500 nm) and cross-sectional line profile.....	57
Figure 3.3	AFM images of single stranded DNA without thiol-modification layer on GaAs (001) surface imaged in (a) height mode, (b) three dimensional view, and (c) cross-sectional line profile. The schematic in (d) illustrates the preferred orientation of DNA on the GaAs surface. ....	59
Figure 3.4.	Schematics of immobilized DNA probes and the bonds of the desired S-As and undesired O-As and N-As DNA to As of the As-terminated GaAs.....	61
Figure 3.5	AFM images of the immobilized thiolated ssDNA layer on GaAs surface (a) after rinsing with DI water without sonication and (b) after ultrasonic cleaning. Dimensions are 2 X 2 $\mu\text{m}$ , z scale is 5 nm. (c) is high resolution scan (500 X 500 nm) of (b) and the cross sectional line profile.....	64
Figure 3.6.	(a) Force calibration plot in terms of signal deflection as function of Z. AFM topographic images of (a) a sample containing 60 $\mu\text{mol L}^{-1}$ DNA on As-terminated GaAs (001) substrate. The scan is 1,000 x 1,000 $\text{nm}^2$ and the vertical scale is 5 nm/div. The scan was obtained from a dried sample in tapping mode after removing the DNA from a region of 500 nm x 250 nm using the AFM tip in contact mode with a force of approximately 70 nN. (b) three dimensional view, (c) plan view, (d) and phase image.....	65

Figure 3.7	AFM image of plane view and height profiles from the scratched area in Figure 3.6(b).....	66
Figure 3.8	Schematics of immobilized DNA probes with the treatment of the short length of thiol molecule (spacer) and the bonds of the desired S-As DNA and spacer to As of the As-terminated GaAs.....	70
Figure 3.9	AFM image of $60 \mu\text{mol L}^{-1}$ DNA and post treated mercaptohexanol (MCH) on As-terminated GaAs (001) substrate. Plane view (a), three dimensional view (b), and line profile (c).....	71
Figure 3.10	Surface morphology of FESEM images (a) non-modified ssDNA layer, (b) thiolated ssDNA layer, and (c) treated MCH of (b) Sample .....	72
Figure 3.11	(a) X-ray scattering scans for DNA in solution (squares), DNA dry with the MCH spacer (triangles) and DNA dry without the MCH spacer (circles). The DNA in solution and the DNA dry with the MCH spacer were taken using X-ray scattering (perpendicular) whereas the DNA dry without the MCH spacer was taken using GIXS (parallel). (b) The X-ray scans for the DNA dry with MCH and the DNA in solution showing the fits to Lorentzian curves.....	76
Figure 3.12	Comparison of Oxygen (1s) XPS peaks from the DNA/GaAs samples (a) without MCH and (b) with MCH spacer and for Nitrogen (1s) XPS peaks from the DNA/GaAs samples (c) without MCH and (d) with MCH spacer.....	79

Figure 3.13	Normalized atomic ratios of S-As, O-As, and N-As from XPS spectra as a function of concentration of ssDNA.....	81
Figure 3.14	Normalized atomic ratios of S-As, O-As, and N-As from XPS spectra as a function of treated concentration of MCH to 60 $\mu$ M DNA sample.....	82
Figure 3.15	Schematic of experimental setup for liquid cell AFM study of ssDNA probes layer on GaAs. In the zoom circle area, the schematic represents that counterions are localized within the DNA brush layer .....	84
Figure 3.16	AFM image of 60 $\mu$ mol L <sup>-1</sup> DNA on As-terminated GaAs (001) substrate in DI water.....	85
Figure 3.17	AFM image of 60 $\mu$ mol L <sup>-1</sup> DNA and post treated mercaptohexanol (MCH) on As-terminated GaAs (001) substrate in DI water.....	86
Figure 3.18	AFM tapping mode topography images in (a) DI water and (b) NaCl 1M solution after attachment 60 $\mu$ M DNA on GaAs substrate. Scan area in images is 500 x 500 nm. The cross-sectional analysis of each image is also provided.....	91
Figure 3.19	AFM tapping mode topography images in air (a) bare GaAs surface, (b) before and (c) after soaking in NaCl 0.1 M solution for two hours after attachment 200 $\mu$ M DNA. The samples rinsed and sonication with deionized water, and dried with Ar gas. Scan area in images is 500 x 500 nm.....	92

Figure 3.20	AFM image in dry of $60 \mu\text{mol L}^{-1}$ 100-base DNA on As-terminated GaAs (001) substrate. Plane view ( $10 \times 10 \mu\text{m}$ ) (a), line profile (b), three dimensional view (c), and plane view ( $2 \times 2 \mu\text{m}$ ).....	97
Figure 3.21	AFM image in dry of $60 \mu\text{mol L}^{-1}$ 100-base DNA and post treated MCH on As-terminated GaAs (001) substrate. Plane view ( $2 \times 2 \mu\text{m}$ ) (a), line profile (b), and plane view ( $500 \times 500 \text{ nm}$ ).....	98
Figure 3.22	Surface morphology of FESEM images (a) thiolated 100-base ssDNA layer (b), and treated MCH of (b) sample.....	99
Figure 3.23	AFM image in dry of $60 \mu\text{mol L}^{-1}$ 100-base DNA on As-terminated GaAs (001) substrate in DI water (a) , and in 1M NaCl solution (b): Plane view ( $2 \times 2 \mu\text{m}$ ), ( $500 \times 500 \text{ nm}$ ) and line profile for each image are shown in the middle and bottom of the figure, respectively. ....	100
Figure 3.24	X-ray scattering scans for 100 bases ssDNA ( $60\mu\text{M}$ ) on GaAs. ....	101
Figure 4.1	Formula of the C(5)-C(5) linked dihydrodimer of thymidine.....	102
Figure 4.2	AFM images of immobilized ssDNA layer on GaAs after irradiation by e-beam with 47MGy dose level. (a) is scanned in air and (b) is scanned in water. Dimensions are $500 \times 500 \text{ nm}$ , z scale is $5 \text{ nm}$ ...	106
Figure 4.3	Cross-sectional schematic of an AlGaAs microresonator.....	110
Figure 4.4	(a) is the AFM plane view image of immobilized ssDNA layer on $\text{Al}_{0.3}\text{Ga}_{0.7}\text{As}$ surface. (b) image is after hybridization of (a) sample	

	with complementary DNA (cDNA). Dimensions are 500 X 500 nm, z scale is 20 nm.....	111
Figure 4.5	SEM images and frequency shift ( $\Delta f=16.773$ kHz) before (a) and after (b) hybridization with complementary DNA on disk type of AlGaAs resonator. The SEM images have schematics of the ssDNA (a) and hybridization DNA (b) on the resonator.....	112
Figure A.1	High resolution XPS As 3d spectrum before (a) and after (b) immersion in acetone for 30 minutes of the immobilized 8-base ssDNA layer on GaAs substrate. No appreciable change is observed.....	121
Figure A.2	High resolution XPS S 2p spectrum before (a) and after (b) immersion acetone for 30 minutes of the immobilized 8-base ssDNA (60 $\mu$ M) layer on GaAs substrate. No appreciable change is observed.....	122
Figure A.3	High resolution XPS S 2p spectrum before (a) and after (b) immersion acetone for 30 minutes of the immobilized 8-base ssDNA (60 $\mu$ M) layer on GaAs substrate. Some change is observed in the relative intensities of the high and low energy peaks.....	123
Figure A.4	High resolution XPS O 1s spectrum before (a) and after (b) immersion acetone for 30 minutes of the immobilized 8-base ssDNA (60 $\mu$ M) layer on GaAs substrate. A new peak is observed at $\sim 536$ eV after immersion in acetone. This peak is probably due to C=O bond of acetone.....	124

Figure B.1	Schematic representation of the procedure followed for preparing edge specimens.....	126
Figure B.2	High resolution TEM image of the immobilized 8-base ssDNA (60 $\mu$ M) layer on GaAs substrate. Diffraction pattern shows extra spot besides the GaAs spots. The Fast Fourier Transforms show two different line spacing.....	127

## **List of Abbreviations**

DNA	Deoxyribonucleic acid
ssDNA	Single stranded deoxyribonucleic acid
MCH	Mercaptohexanol
DTT	Dithiothreitol
DI water	De-ionized water
PBS	Phosphate buffer solution
A	Adenine
G	Guanine
C	Cytosine
T	Thymine
AFM	Atomic force microscopy
XPS	X-ray photoelectron spectroscopy
FESEM	Field emission scanning electron microscopy
GIXS	Grazing incident X-ray scattering
LINAC	Electron liner accelerator

## Chemical Nomenclature

GaAs	Gallium arsenide
AlGaAs	Aluminum gallium arsenide
HCl	Hydrochloric acid
HS(CH <sub>2</sub> ) <sub>6</sub> OH	6-Mercapto-1-hexanol
HS(CH <sub>2</sub> ) <sub>n</sub> X	Long chain thiols (X is the end group)
KCl	Potassium chloride
KH <sub>2</sub> PO <sub>4</sub>	Potassium phosphate
Ar	Argon gas
Na <sub>2</sub> HPO <sub>4</sub>	Sodium phosphate dibasic
NaCl	Sodium chloride

## Greek Letters

$2\theta$	Scattering angle
$\alpha$	Grazing angle
$\chi$	Chi- angle
$\varphi$	Rotation angle about surface normal
$\lambda$	X-ray wavelength
$\rho$	Density

# **Chapter 1**

## **1. Introduction and Background**

### **1.1 Overview**

Immobilization of DNA probes on a variety of semiconductor surfaces has become an important area of research over the past few years due to its potential application in the fields of molecular electronics[4-6] and future computer architectures and massive memories[7]. The fundamental understanding of the chemical interactions and properties of dry-wet interfaces has become a key scientific issue in nanoscience. Hence, the understanding of the attachment of organic molecules to inorganic semiconductor surfaces has relevance to the future development of nanoelectronics and related technologies. The initial attachment of organic molecules to surfaces was reported in 1992[8, 9], and the self-assembly of DNA bases on crystalline gold in an ordered two dimensional lattice was achieved in 1994[10, 11] and has been a key step in this technology. The observed two-dimensional order is a superlattice that is enhanced whenever the regular structure of the absorbed molecules corresponds to the structure of the underlying gold. The self-assembly process was described as consisting of three stages: (1) the initial appearance of random clusters of ordered molecules at the gold reconstruction sites, (2) occupation of all reconstruction sites by clusters, and (3) rearrangement of the molecules to cover the remaining gold surface with a 2-D lattice[10]. The use of alkanethiol self-assembly methods to fabricate DNA modified gold surfaces has also

been previously reported[12-16]. Attempts have also been made to attach DNA on oxidized silicon and silicon surfaces.[17-20]

The attachment of single stranded DNA (ssDNA) to a semiconductor is a vital step towards the development of a biochip. We have recently started to investigate the surface attachment chemistry and physics of DNA on GaAs[21]. Our group had previously demonstrated, the chemical attachment of the thiol-derivatized DNA monolayers on arsenic terminated GaAs (001). The sulfur-As-based covalent bonds of the thiolated oligonucleotides on the arsenic terminated GaAs (001) were observed using x-ray photoelectron spectroscopy (XPS). The purpose of this work was to investigate the self-assembly of thiol-derivatized single-stranded DNA oligonucleotides (probes) on As terminated GaAs substrate. Our group also demonstrated that both the S-H group in the thiolated single-strand DNA, and the N-H group in the DNA bases are functional groups that can be utilized to anchor the DNA molecule, or other biological molecules, on the arsenic-terminated GaAs surface. We have performed additional experiments on the attachment using Grazing Incidence X-ray Scattering (GIXS) on the 8 base pair DNA to determine the orientation of the strands with respect to the GaAs surface. These results provide a solid foundation for the understanding of the attachment and surface chemistry and physics of DNA probes on GaAs.

Several studies have used organic molecules terminated with a thiol group to enhance the attachment on the surfaces. The formation of long chain  $\omega$ -terminated

dialkyldisulfide molecules on a gold substrate was first reported in 1983.[22] Alkyl thiols resulted in formation of monolayers on gold.[23] Bain and Whitesides presented a model system consisting of long-chain thiols,  $\text{HS}(\text{CH}_2)_n\text{X}$  (where X is an end group such as  $\text{NH}_2$ ,  $\text{COOH}$ , or  $\text{OH}$ ), that adsorb from a solution onto gold and form densely packed, oriented monolayers.[24-26] The bonding of the sulfur head group to the gold substrate is in the form of a metal thiolate, which is a very strong bond ( $\sim 44$  kcal/mol) and hence the resulting films are quite stable and suitable for surface attachment of functional groups. The DNA molecule can be functionalized with a thiol (S-H) or disulfide (S-S) group at the 3' or 5' ends. Upon immersion of clean gold surfaces in a solution of thiol derivatized oligonucleotides, the sulfur adsorbs on the gold forming a single layer of molecules, where the hydrocarbon is now replaced with a single stranded DNA (ssDNA) molecule.

Ratner and co-workers at the University of Washington studied the self-assembly of purines and pyrimidines bases from solution on crystalline gold surface. They concluded that mercaptopurine, purine, adenine, thymine, and cytosine self-assemble on crystalline gold in an ordered two-dimensional lattice similar to that in the bulk crystal. This study showed the possibility of attaching DNA to metal surfaces in an ordered monolayer. Tarlov and coworkers at the National Institute of Standards and Technology (NIST) also focused on the surface characterization of thiol-derivatized ssDNA monolayer immobilized on gold surfaces with mercaptohexanol (MCH)[27, 28]. The MCH spacer prevents the nonspecific attachment of DNA to the surface (through the C=O and NH groups of the bases) and enhances the specific

attachment (through the thiolated group). The specific attachment via the thiol group to the gold surface enhances the vertical alignment.

In this work, I performed a series of investigations which target the understanding of the mechanisms involved in the attachment of ssDNA oligomers on GaAs, and related compound semiconductor surfaces such as AlGaAs, InGaAs, and InAlAs. In particular the selective attachment of DNA to GaAs-based semiconductors was studied. I investigated the mechanisms of attachment via a complete understanding of the interface chemistry and physics between the DNA molecules and the semiconductor substrate surface. Preliminary studies of the application of immobilized DNA on GaAs for radiation detection and for hybridization detection using AlGaAs were performed using DNA probes attached to GaAs and target molecules in aqueous media.

Hybridization is the hydrogen-bonding interaction between two DNA strands that obey Watson-Crick complementary rules[3]. DNA strands can be very long, thread-like polynucleotides, made up of a large number of deoxyribonucleotides. The purine and pyrimidine bases of DNA carry genetic information, whereas the sugar and phosphate groups perform a structural role. The variable part of DNA is the sequence of its bases. DNA contains four kinds of bases, two purines and two pyrimidines. The two purines are adenine (A) and guanine (G). The two pyrimidines are thymine (T) and cytosine (C). A double strand helix will be formed through hydrogen bonding between the bases of two single strands. The hydrogen bonding

occurs between A and T, and G and C to produce complementary base pairs when two single strands form one double helix. This process is called annealing or hybridization. Ligation is the process in which the free 5' end of one strand reacts with the free 3' end of another strand to create a longer chain. Although the structure of DNA helices is extremely rigid, it can be changed under certain conditions. Several nucleic acid based technologies (e.g. genome arrays, Northern and Southern blotting analytical techniques, etc.) utilize hydrogen bond hybridization between complementary strands. Also, enzyme-based extensions of nucleic acid hybridization are widespread e.g., polymerase chain reaction, PCR and applications such as DNA-based computing. Hence, understanding the fundamental mechanisms of both the attachment is a vital step to building a chip which can be used in all these advanced Biotechnology applications.

## **1.2 Polymer Brush Structure on Planar surface, and the Effects of Electrolytes**

DNA is a polyelectrolyte due to a negative charge in the phosphate backbone. To understand the properties of monolayers of immobilized DNA, although DNA layer structure is a polyelectrolyte brush, it is necessary to review the theoretical background of tethered neutral polymer chains.

### **1.2.1 Tethered Neutral Polymer Chains on Planar Surface**

Tethered neutral polymer chains have been studied for a long time and are well understood compared to the polyelectrolyte case. A number of studies on the structure of tethered neutral polymer chains on planar surfaces have been carried out using various theoretical means and computer simulations, such as scaling theories, self consistent field (SCF) theory, molecular dynamics, and Monte Carlo simulations. Although a tethered polyelectrolyte chain is more complex, the same concepts for tethered neutral polymer chain can be applied to polyelectrolyte system. Alexander demonstrated scaling theories that determine the structure of a grafted polymer chains in a good solvent with the assumption that the polymer chains are uniformly stretched and the segment concentration is constant through the layer. The scaling theories indicate that tethered neutral polymer chains on a surface are subjected to a deformation from equilibrium configurations. The deformation is the outcome of the competition between excluded volume interactions and the entropic elastic energy of the system. Uniform stretching of the chains is a basic assumption for the scaling theory. Another basic assumption is that the monomer density is constant up to a height (  $L$  ) from the surface. Figure 1.1 shows a schematic of tethered neutral polymer chains on a planar surface used for scaling theory [1].

Under this condition, the volume fraction of a segment is

$$\Phi = N a^3 / (Ld^2) \quad (1.1)$$

d : Average distance between polymer grafting points

L: Equilibrium brush height

N: Number of repeat units

a: Statistical segment length

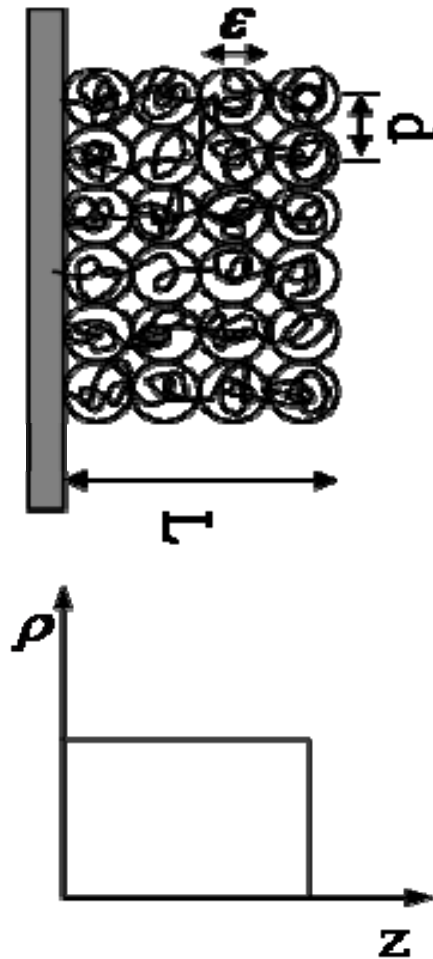


Figure 1.1 Schematic of tethered neutral polymer chains on a planar surface.  $L$  is the layer thickness,  $d$  is the average spacing between neighbor tethered points, and  $\epsilon$  is the blob size. The graph shows the monomer density,  $\rho$ , as a function of distance,  $z$ , from the surface.[1]

The free energy per chain,  $F_{\text{chain}}$ , in the brush is the sum of osmotic excluded volume interactions,  $F_{\text{os}}$ , and the elastic stretching energy of Gaussian chains,  $F_{\text{el}}$ , that measures the entropic penalty of chain stretching :

$$\frac{F_{\text{chain}}}{kT} = \frac{F_{\text{os}}}{kT} + \frac{F_{\text{el}}}{kT} \approx \frac{\nu\Phi^2 d^2 L}{a^3} + \frac{L^2}{R_{g0}^2} \quad (1.2)$$

Where  $\nu$  is a dimensionless excluded volume parameters(  $\nu \rightarrow 1$  for a good solvent),  $R_{g0}^2$  is the radius of gyration ( $\sim Na^2$ ),  $d$  is the average distance between polymer tethering sites,  $L$  is the equilibrium layer height, and  $\Phi$  is volume fraction of segments( $\sim Na^3/Ld^2$ ) . Minimizing the free energy  $F_{\text{chain}}$  with respect to  $L$  leads to the equilibrium coverage for overlap,  $L$  is

$$L \approx Na\nu^{1/3} \left( \frac{a^2}{d^2} \right)^{1/3} \sim Na\sigma^{1/3} \quad (1.3)$$

where  $\sigma$  is the ( number of chains per unit area)  $\sigma = a^2/d^2$ . For the polymer chain in a good solvent, the radius of gyration of a polymer coil  $R_g$  is  $R_g \sim aN^{3/5}$ . The results of  $L$  ( $\sim N$ ) and  $R_g$ ( $\sim N^{3/5}$ ) indicate that the tethered chains are highly stretched compared to the untethered case.

Genes demonstrated two regimes based on the tethering density, so-called mushroom and brush regime [29]. The mushroom regime refers to the limit of low  $\sigma$ , where the chains do not overlap and  $R_g$  ( $\sim aN^{3/5}$ ) less than the distance ( $d$ ) (see Figure

1.2). Thus,  $R_g < d$  leads to  $\sigma < N^{-6/5}$ . In the brush regime which corresponds to overlap between stretched chains,  $\sigma$  is larger than  $N^{-6/5}$ . (see Fig 1.2)

In the mushroom regime, the polymer coils have an equilibrium height  $L \approx R_g$ . In the brush regime, the equilibrium brush height ( $L$ ) can be calculated by the number of blobs per chain and the blob size.

$$L = (\# \text{ blobs per chain})(\text{blob size}) = (N/g) \zeta = (N/g) d = Na\sigma^{1/3} \quad (1.4)$$

Where  $\zeta$  is the correlation length, or the blob size,  $g$  is the number of monomers per blob  $((d/a)^{5/3})$ , and  $N/g$  is the number of blobs. Even though correlations are included in the calculation, the brush height ( $L$ ) is still the same as for the case of poor solvent. When the polymer is contained between two plates separated by a distance less than twice the brush thickness ( $D \leq 2L$ ), compression forces apply on the chains. Gennes derived the equation for the surface pressure ( $\Pi$ ) as function of the separation distance ( $D$ ). [29]

For  $D \leq 2L$ ,

$$\Pi(D) \cong \frac{kT}{d^3} \left[ \left( \frac{2L}{D} \right)^{9/4} - \left( \frac{D}{2L} \right)^{3/4} \right] \quad (1.5)$$

For low surface coverage, mushroom regime, the chains do not overlap sufficiently to cause stretching. The interaction between the chains confined to two

plates will increase when the separation distance is less a twice the extension of the chains and the chains are under compression because of their confinement.

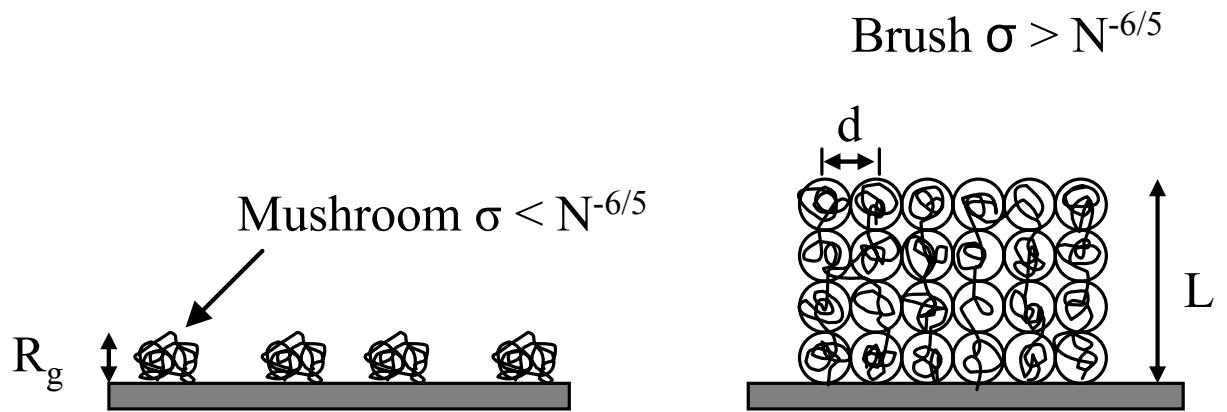


Figure 1.2 Mushroom regime and brush regime of tethered polymer layer.[2]

To compare the scaling assumptions, self consistent field (SCF) theory [1] was applied to consider that the monomer density is not uniform along the polymer layer thickness. This assumption is realistic and describe in the intrinsic layer structure. If the chains strongly stretch, the chains fluctuate a little bit near the most favorable configuration which minimizes the energy of the system. The mean field energy of a strongly stretched layer can be calculated by

$$E(L) = \frac{1}{2} \left( \frac{\pi^2}{12} \right) \frac{NkTv^{\frac{2}{3}} \mathcal{G}^{\frac{1}{3}}}{\sigma^{\frac{5}{3}}} \left[ \frac{L}{D} + \left( \frac{D}{L} \right)^2 - \frac{1}{5} \left( \frac{D}{L} \right)^5 \right] \quad (1.6)$$

Where  $\mathcal{G}$  is a concentration dependent materials parameter with dimensions of inverse length squared and  $v$  is the excluded volume parameter. The brush thickness at equilibrium is obtained as:

$$L(d) = \left( \frac{12}{\pi^2} \right)^{\frac{1}{3}} Nv^{\frac{1}{3}} \mathcal{G}^{\frac{-1}{3}} d^{\frac{-2}{3}} \quad (1.7)$$

Therefore, in SCF theory the brush height has the same dependence on  $N$  and  $d$  as obtained by scaling theory, even though the numerical coefficient is slightly larger.

The monomer density in the SCF theory can be determined by the distance  $z$  between the tethered polymer molecules on the surface in a good solvent as:

$$\rho(z) = \frac{3N\sigma a}{2L} \left[ 1 - \left( \frac{z}{L} \right)^2 \right] \quad (1.8)$$

This density value is valid only for very large  $N$  and moderate  $\sigma$  where binary interactions dominate. Unlike the scaling theory, the specific points of the free ends of the chains are at the outer boundary of the brush in SCF theory. The SCF approach revealed that the end chain of a has the maximum probability of being located at a distance of around  $0.7L$  away from the flat substrate surface, and the free ends of the chains are distributed throughout the entire brush layer.

In contrast to a good solvent environment, the conditions for layers in a poor solvent have not been investigated in much detail. In a poor solvent, the polymer segments tend to attract each other. In a poor solvent, the chains try to isolate from the solvent, by coiling of the polymer coil, i.e., the radius shrinks below  $R_g$ . The coiling is the result of the attraction by *van der Waals* or the salvation forces within the polymer. The coils, however, do not collapse completely because of the monomer-monomer repulsive that still dominates for smaller radius. When the distance between two faced flat surfaces containing tethered chains is reduced in a poor solvent, steric overlap repulsions become dominate. Under poor solvent conditions, Pincus derived the forces between planar polymer brush surfaces. The forces are attractive in long range and repulsive in short range. The polymer chains can forms bridges between two faced surfaces depending on the properties of

interaction between the polymer and the surfaces. The net interaction is the sum of segment-segment forces and segment-surface interactions and depends on the probability for the segments to approach to binding sites on the opposite surface. A strong bridging formation is the result of the strong attraction between the polymer and the surface which exceeds *van der Waals* attraction within the polymer as the thickness of the brush increases beyond polymer length, the bridging attraction is reduced.

### **1.2.2 Tethered Polyelectrolyte Chains on Planar Surface**

A polyelectrolyte brush is an end-grafted charged polymer attached to a surface. Unlike the neutral polymer brush case, due to the long range electrostatic interactions, the polyelectrolyte brush has more complexity. These electrostatic interactions between charged polymers are not fully understood yet and the correlation of the chains is difficult to explain because of the complexity of the system. The configuration of the charged layers depends on the ionic strength of the solution and the degree of ionization of charged group along the polymer backbone as well as the molecular weight, tethering density, and solvent quality found for neutral brush system. In a tethered polyelectrolyte brush system, the structure of the brush depends not only on the entropic and elastic interaction but also the degree of ionicity of the polymer ( $f$ ) and the concentration of salt ( $C_s$ ) in solution. Using an energy balance technique, Pincus described the structure of polyelectrolyte chains as a function of counterion osmotic pressure and the chain elasticity with different

grafting densities and charge density [2]. He studied two cases, one without added salt ions and one with added salt.

### **Without Added Salt**

Pincus assumed that inside the blob, which is the repeated unit along the polymer chain, of the dimension of the chain scales in a similar way to neutral polymers. He also disregarded local chain stiffness due to of local electrostatic interactions. Another basic assumption is a uniform monomer concentration throughout the brush thickness ( $L$ ) like for neutral polymer brush. Pincus divided two possible different behavior regimes dominated by electrostatic interaction for tethered polyelectrolyte brush in the absence of salt in the solution. The counterion density ( $\rho_c$ ) decreases as a power law of the distance from the surface. The counterions are limited near the surface over the Gouy-Chapman length  $\xi$  (neutralization length):

$$\xi = \frac{1}{2\pi\rho_c l_B} \quad (1.9)$$

Where  $l_B$  is *Bjerrum length*.

The neutralization length  $\xi$  is the distance over which the charge of the counterion is neutralized. Then two possible regimes are identified: the  $L > \xi$  regime, and  $L < \xi$  regime (see Figure 1.3). where,  $L$  is the brush height.

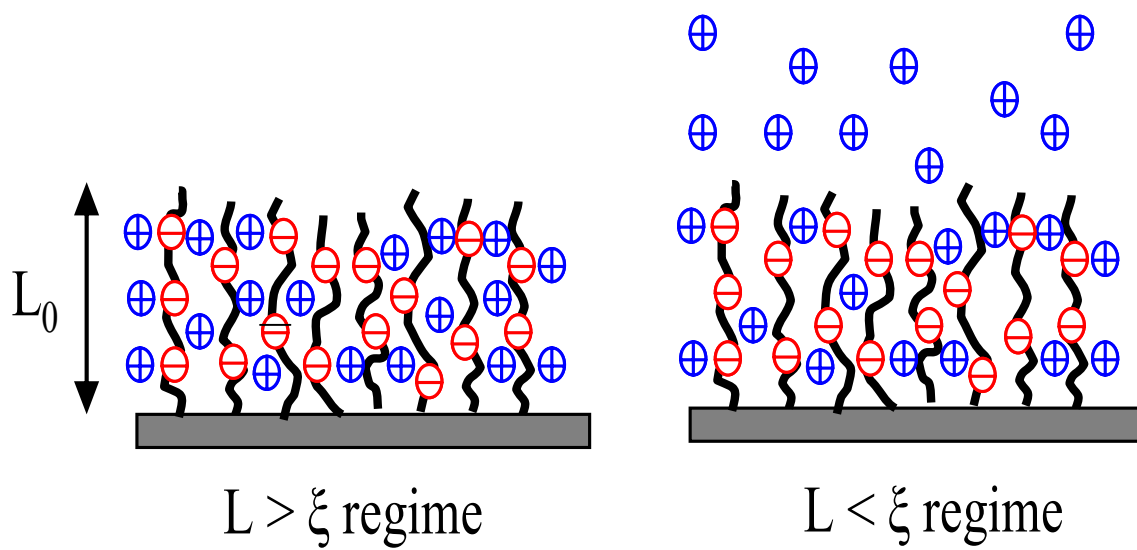


Figure 1.3 Schematic representation of two different regimes for polyelectrolyte brush: (a) osmotic regime ( $L \geq \xi$ ) and (b) charged regime ( $L < \xi$ ) [2].

In the  $L \geq \xi$  regime, called osmotic regime, for relatively dense and strongly charged polymer brushes, the mobile counterions are distributed within the brush height, and there is balance between the swelling effect of counterion entropy and the chain elasticity. The osmotic pressure produced by the counterions trapped inside the brush would make the brush swell. The thickness of the brush does not relate to the strength of the electrostatic interaction since the stretching of the chain is only due to counterion pressure in this regime. The counterion osmotic pressure  $P$  is  $P \approx fcT$ . Where  $f$  is the fixed fraction of counterions,  $c$  is the counterion concentration, and  $T$  is the temperature. Thus, the brush height  $L$  is given by

$$L \cong f^{1/2} Na \quad (1.10)$$

$L$  is proportional to the chain length  $N$  (number of repeating units) as in the case of neutral brush, and  $a$  is characteristic dimension of each repeating unit. In this case,  $L$  does not depend on the tethering density  $\sigma$  and the chains are strongly stretched for limited charging.

In the  $L < \xi$  regime, called charged regime, for relatively low degree of ionization, the counterions distribute beyond the outer ends of the brush. This system is not locally charge as the charge in the brush is balanced by the cloud of mobile counterions. The pressure on the stretching chains applies only partially to the chains. In this case, both electrostatic interaction and entropic contribution determine the height of the brush. In this regime, the brush is similar to a simple charged surface

with charge density,  $fN / d^2$ . The neutralization length  $\xi$  is  $d^2/2\pi l N f$ , where  $l$  is the Bjerrum length. The counterion osmotic pressure,  $P$ , is reduced by the fraction of remaining within the brush region,  $L/\xi$ . Thus,  $P$  is given by

$$P \cong fc(L/\xi)T \cong kL/d^2 \quad (1.11)$$

Thus,

$$L \cong 2\pi l N^3 (fa/d)^2 \quad (1.12)$$

This shows the unusual  $N^3$  dependence of the brush height as well as its dependence on the tethering density  $\sigma$ .

Similar to the case of neutral polymer chains on planar surface case, we take into account two different cases ( $D \leq 2L$ , and  $D > 2L$ ) about surface pressure when two opposing surfaces with tethered polyelectrolytes approach each other. When the distance is larger than twice of the thickness, the brush behaves as a highly charged surface. The surface pressure can be calculated by disjoining pressure.

$$P(D) \approx \frac{2kT}{\pi l_B D^2} \quad (1.13)$$

$k$  : Boltzman constant,  $T$  : temperature,  $l_B$  : Bjerrum length

When the two surfaces are close enough, the brush is under compression by the counterion osmotic pressure.

$$P(D) \approx \frac{2fN_B kT}{d^2 D} \quad (1.4)$$

In this case, the osmotic pressure is higher than for a neutral polymer brush with the same condition of grafting density and molecular weight.

### **With Added Salt**

Adding monovalent, completely ionized salt gives rise to screening of the electrostatic interactions within the polymer. The screening is related to a Debye screening length  $k_S^{-1}$  given by,

$$k_S^{-1} = 8\pi l_B C_S N_{av} \quad (1.15)$$

Where  $C_S$  is the salt concentration, and  $N_{av}$  is Avagadro's number.

The structure of the polyelectrolyte brush is affected by the salt only when the concentration of salt is high enough such that the corresponding Debye screening length  $k_S^{-1}$  is comparable to the neutralization length  $\xi$ . When  $k_S^{-1} > \xi$ , the a screening limit, the structure of the polyelectrolyte brush can be determined similarly to the  $L > \xi$  regime described above. When the salt concentration is increased  $k_S^{-1} < \xi$ , the Debye screening reduces the counterion osmotic pressure, causing the polyelectrolyte chains to stretch. Witten and Pincus studied this case. They have proposed the osmotic pressure of a semi-dilute polyelectrolyte solution to be

$$P \cong cT(k_0/k)^2 \quad (1.16)$$

Where  $k_0$  : the Debye length associated with the counterions alone ( $k^2 = k_0^2 + k_s^2$ )

By balancing osmotic pressure and entropy loss of the polymer, one can obtain:

$$P \cong cT(k_0/k)^2 \cong LT[N(ad)^2]^{-1} \quad (1.17)$$

$$L \cong Na \left( \frac{2a}{d^2} C_s \right)^{-1/3} \quad (1.18)$$

This result indicates that the polyelectrolyte brush shrinks with increasing salt concentration with a relatively weak power law  $C_s^{-1/3}$  (see Figure 1.4). Hariharan extended Pincus model to obtain the height of the polyelectrolyte brush for the case when a less sensitive dependence of  $L$  on the concentration of added salt ( $L \approx C_s^{-1/6}$ ) [30, 31].

In summary, Pincus predicted that for an electrolyte in a solvent containing salt the counterions are mostly located in the polyelectrolyte brush layer. Therefore, the thickness of the brush depends on the balance of the osmotic pressure of the counterions within the layer and the configurational elasticity of the chains. At no or low ionic strength, the polyelectrolyte brush is nearly stretched to almost full length. In contrast, when a large concentration of salt is added, the brush collapses because

the electrostatic interactions are apparently insufficient and screened to maintain an extended rodlike conformation.

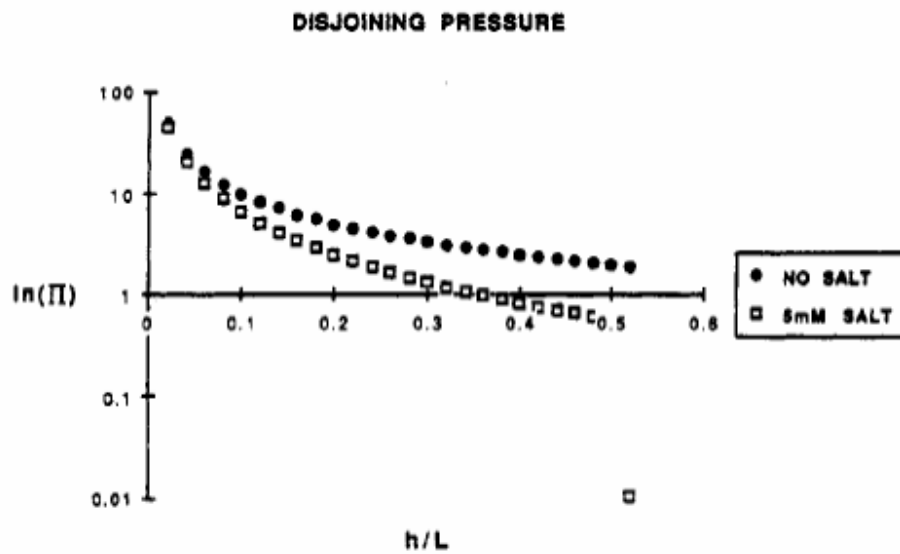


Figure 1.4 Logarithm dependence of the osmotic pressure between two identical polyelectrolyte brushes plotted as a function of the surface separation normalized to the brush height for fully extended chains. The filled squares are for no added electrolyte while the open squares are for 5mM monovalent salt. The pressure is in arbitrary units. The parameters used for this calculation are  $L_0 = 10^4 \text{ \AA}$ ,  $d = 10^3 \text{ \AA}$ , and  $f = 1$  [2].

### **1.3 DNA monolayer**

DNA monolayers are of great interest both for fundamental research and for application in sensing, medical diagnostics, and bioengineering applications where specific recognition is required. Hybridization is the binding of two complementary DNA strands together with A:T and G:C pairing. This specific binding allows identification and detection of un-known single strand DNA (target) by binding to known sequence DNA (probe) immobilized on a surface (see Figure 1.5). For this process, first, probe DNA is immobilized on the surface. The common candidate substrate could be either gold, glass slide, silica, or silicon wafer. Second, the substrate together with the immobilized probe DNA is immersed or dropped in the solution containing the target ssDNA. Hybridization will occur only if the complementary strand is present in the solution. This system needs to give some kind of detectable signal to indicate that hybridization has taken place. The detectable signal could be electrical or optic. Fluorescent tags on target DNA are usually used for detection of successful hybridization. However, the fluorescent molecules which are incorporated into the probe layer may interfere with hybridization. Therefore, different detection system is recently being considered from other type of signal, such as, electrical signal due to the change of mass upon hybridization.

For better sensing, it is necessary to understand the physical and chemical properties of the DNA monolayer and to develop new substrates that could make a more sensitive biochip. Another possible advantage is the reusability of the substrate.

This possibility has increased the interest in the bonding stability between probe DNA and the substrates.

## **1.4 Immobilization of DNA onto Solid Surface**

Adsorption is the simplest way for immobilization of DNA on a solid surface because it does not need pretreatments or modifications. The substrate could be nylon membranes, polymer films, carbon electrodes or metal oxide surfaces. For example, Nylon membranes can bind to both DNA and RNA [32-34]. The palladium oxide surface also could bind nucleic acids through palladium-nitrogen or palladium - hydrogen bonds [35-37]. However, this adsorption method has poor efficient binding with short length nucleic acids, is time consuming and has poor sensitivity. Also, probe DNA might desorbs from the surface during the hybridization or washing process. Because the binding is weak, the main disadvantage of the binding is that individual probe molecules may attach to the surface at several points, so that the possibility of hybridization is dramatically reduced. Other case of immobilization by non covalent bonding is based on using a protein layer, such as, avidin and streptavidin which bind very tightly to biotin [38-40]. The biotinylated DNA binds with a relatively high strength to an avidin/streptavidin layer on the substrate [41]. The formation of a avidin/streptavidin layer is hard to control and the protein also can play a role as a site for non-specific recognition.

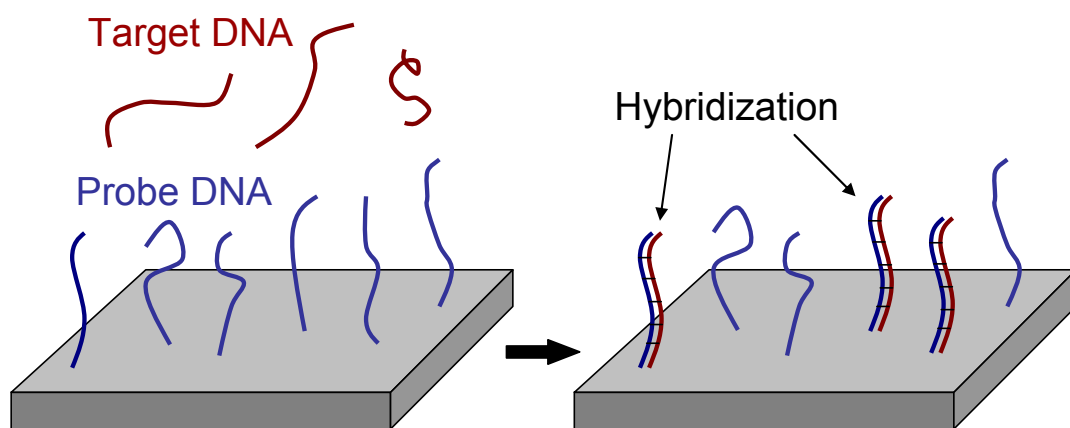


Figure 1.5 Schematic of immobilization of probes and hybridization with target strands

Covalent binding of the DNA probe to a substrate surface has recently been the focus for oligonucleotide immobilization because it can enhance stability of the probe and increase the surface density of the immobilized probes. A DNA biosensor that uses covalent attachment method can be easily refreshed remove the probe and reuse. One example is *in situ* synthesis of the oligonucleotide directly on a solid substrate. The photoresist techniques can allow to synthesize more than 90,000 different oligonucleotides. This method, however, has two big drawbacks which are: limitation of probe length synthesized and a high possibility of making faulty sequences during the processing. Another method for immobilization is by applying pre-synthesized oligonucleotides which have functionalized groups, such as, amine, carboxyl, carbonyl, and thiol groups at the 3' or 5' end. Immobilization of a DNA layer can be achieved on substrates, such as, siliceous, gold and GaAs-based semiconductors.

#### **1.4.1 Immobilization of Thiolated DNA on Gold Surface**

Gold substrates for immobilization of DNA have been used because of its electrochemical properties of gold [16, 42-44]. Single stranded DNA with modified thiol- endgroup is attached on gold metal surface directly by the gold-thiol bond. Another approach for good quality of DNA monolayer with gold substrate is using alkanethiol molecule, such as mercaptohexanol [13, 27, 45-47]. Mercaptohexanol

serves to block physical adsorption of the oligonucleotide to the metal surface to ensure specific attachment via the thiol end group.

### **1.4.2 Immobilization of DNA on Siliceous Substrate**

Glass and silicon are other common substrates for immobilization of nucleic acids [48-50]. Silanol (-Si-OH) groups are the active sites used to bond nucleic acid to [17, 18, 48, 51-60]silicon and silica substrates. Siliceous substrates have also been researched with other modified surface. Jin L. and coworkers have investigated aminopropyltriethoxysilane (APTES) treated silica with heterobifunctional crosslinkers *p*-maleimidophenylisocyanate (PMPI) for immobilization of thiolated ssDNA [61]. This study showed that the probes on the PMPI activated surface are able to bind complementary strands from solution at yields of up to 40%. Figure 1.6 shows the procedure of pretreatment and immobilization.

### **1.4.3 Immobilization of Thiolated DNA by Covalent Bonding on GaAs-based Semicnductors**

Miniaturization and integration of the detecting system into the sensor is a very important factor for applications, in the field of biosensors. Therefore, the use of other substrates, which are able to be fabricated into a micro or nano-scale chip, is another area of research in this field. Metal based substrates, such as, gold are not suitable for the fabrication of devices semiconductor technology. In the Si-based

semiconductor, complex layers on Si substrate are not desirable for the design of DNA chip.

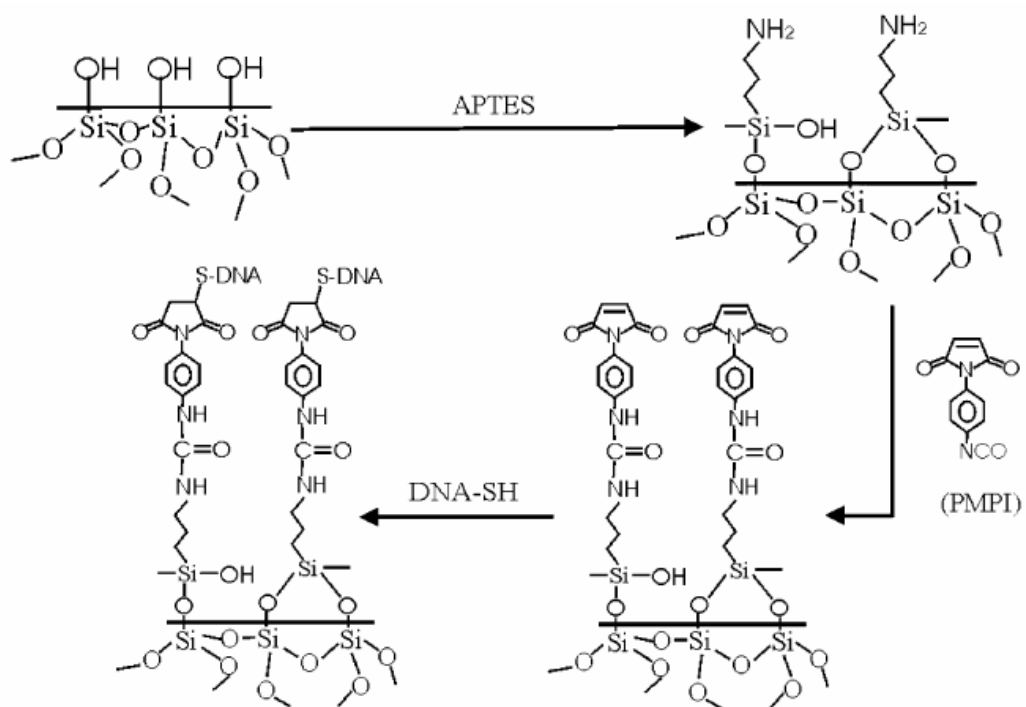


Figure 1.6 DNA immobilization (i) silanization of the solid support with APTES, (ii) reaction of cross linker (PMPI, MBS, or sulfo-MBS) with APTES to generate a maleimide surface, and (iii) reaction of thiol end-groups on DNA with surface maleimides [61].

Gallium arsenide (GaAs) is a semiconductor with direct band-gap ( $E_g = 1.42\text{eV}$ ) and unique crystal structure. Also, GaAs is a desirable material for optoelectron VLSI circuits, sensors and systems requiring emitters such as lasers or light emitting diodes(LED). In addition, GaAs is a promising material for the fabrication of intergrated sensor using its piezoelectric properties [62-64]. Figure 1.7 shows the As-rich (2 X 4) reconstructed surface of GaAs (001). Unlike Si-based semiconductors, As-terminated GaAs attaches to the thiolated-DNA directly through As-S covalent bonds without need of an oxide or gold layer. The attachment of DNA on Si requires predeposition an oxide layer that causes the DNA molecules to lay-down on the surface reducing its efficacy for hybridization in a biochip. Another crucial advantage is that GaAs-based semiconductors have a much higher resonant frequency over silicon. This is important for the fabrication of microresonators that were used in this work for detection of hybridization with very high sensitivity,

L. M. et al demonstrated that thiolated single stranded DNA can be successfully covalently anchored to GaAs and utilized X-ray photoelectron spectroscopy to show evidence that the thiol group can be used to form the attachment on an As-terminated surface [21, 65-67].

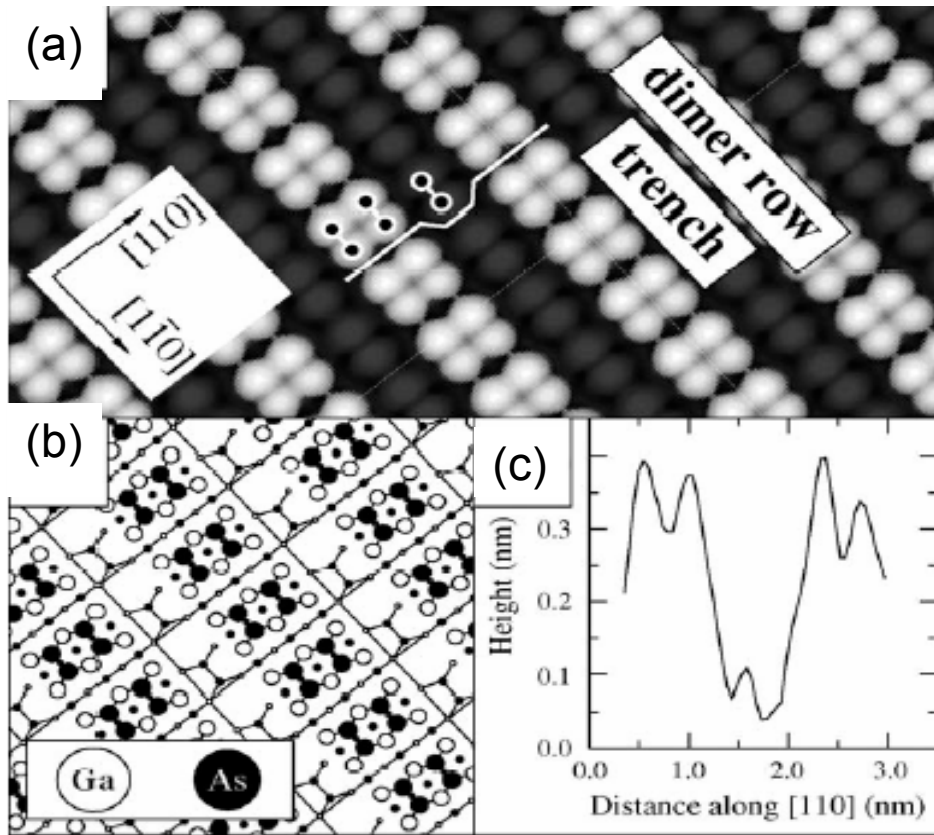


Figure 1.7 (a) simulated STM image of the (2x4) reconstructed surface of As-terminated GaAs using a filled-state bias of 0.3 V below the valence band maximum; (b) structural model of the reconstructed surface; (c) height cross-section across a dimer trench along the [1 1 0] direction [68] .

## 1.5 DNA Hybridization

Deoxyribonucleic acid (DNA) is a polymer composed of 5-carbon sugar(deoxyribose), a nitrogen containing base and a phosphate group. The sugar in the DNA binds the hydrophilic phosphate group. On the other hand, bases are hydrophobic. The bases are divided by their chemical structure into purines, composed of adenine (A) and guanine (G), and pyrimidines, composed of thymine (T) and cytosine (C).

DNA hybridization is a reaction between two complementary single strands of DNA that bind with each other through hydrogen bonding (see Figure 1.8). Only very specific bonds between a purin and a pyrimidine base pair can form upon hybridization. A-T and G-C are the only possible purin-pyrimidine base pairs because only these base pairs have the right position for bonding to occur in the double helix at the right hydrogen bonding distance. Once hybridization has taken place, the pyrimidine-pyrimidine ring pairs would be too far for the formation of double helix and the purine-purine ring pairs would be too big. The hydrophilic phosphates are located in the outer side of the helix structure while the inner region is occupied by the hydrophobic bases. The hybridization efficiency and stability of the hybrid depend on several factors, such as, salt concentration, length of target DNA, composition of DNA, mismatch percentage, and temperature. Monovalent cations , manly  $\text{Na}^+$ , electrostatically interact with the phosphate group in the nucleic acid. The concentration of the cations in the hybridization buffer affects the rate of

hybridization because of the electrostatic interaction between probes and targets. If the concentration of probes on the surface of a substrate is larger than the concentration of target, the diffusion of target controls the hybridization rate. Consequently, short targets would have a faster hybridization rate. The hybridization rate increases with increasing temperature. The melting temperature ( $T_m$ ) is defined as the temperature at which 50 % of the oligos are hybridized.  $T_m$  is given by

$$T_m = 81.5^\circ\text{C} + 16.6(\log_{10}[4]) + 0.41(\%G+C) - 600/L \quad (1.19)$$

Where,  $M$  is the molal concentration of a monovalent cation,  $(\%G+C)$  is the percentage of G and C nucleotides in the DNA and  $L$  is the length of the duplex in base pairs.

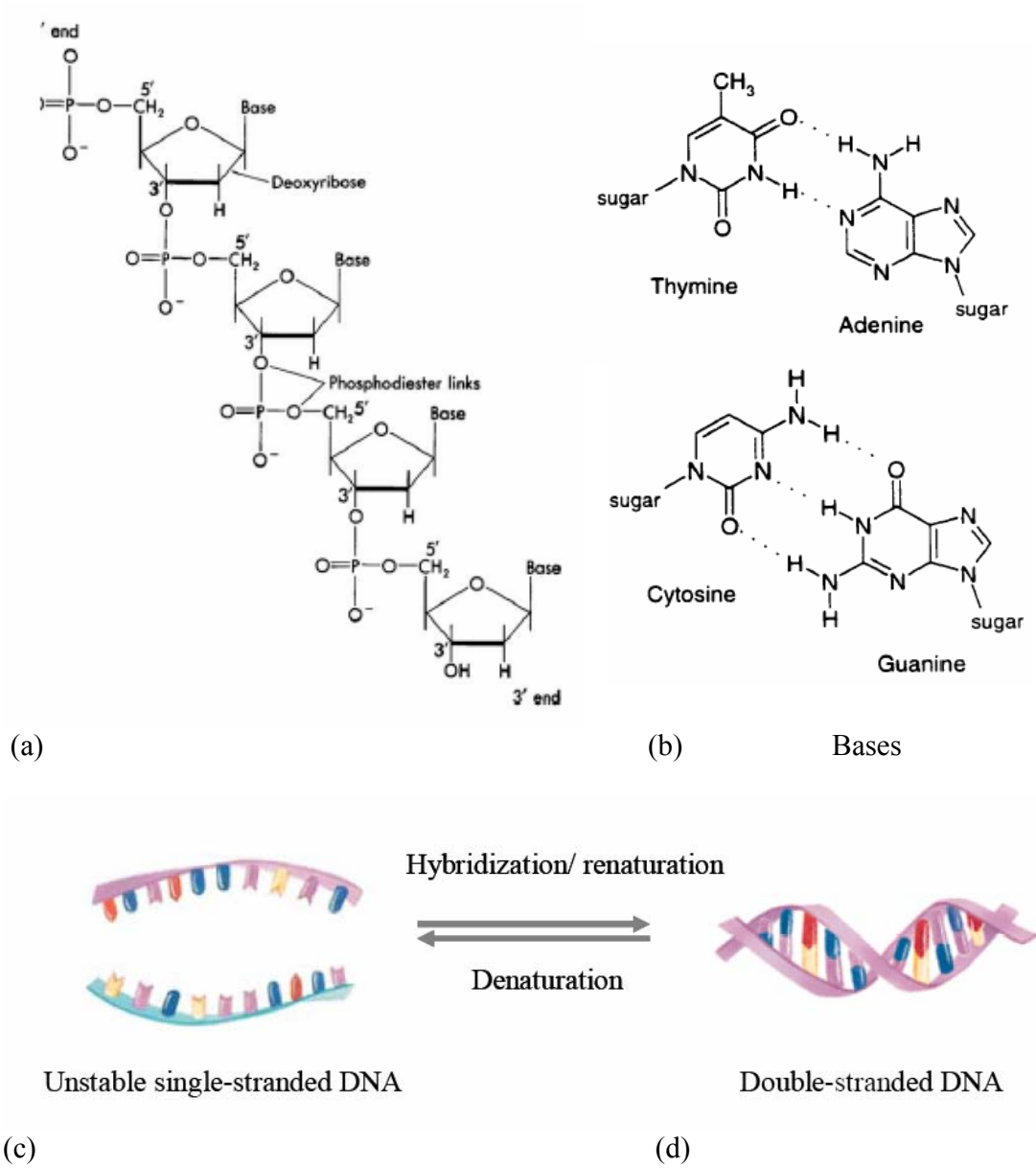


Figure 1.8 (a) The primary structure of DNA (b) complementary hydrogen bonded base-pairs as proposed by Watson and Crick(c), (d) a schematic representation of DNA hybridization and denaturation.[3]

## **1.6 Applications using Immobilization of DNA**

A good design for a biosensor should have high specificity and sensitivity for the purpose of analyzing specific targets. The signal response should be accurate, rapid, and precise. The biosensor system should also be small, cheap, and preferably reusable. A small amount of sample needed is preferred for analysis as long as it is enough to obtain an effective signal within a short response time. Other requirements of this type of biosensor are that it uses direct, i.e., label free, methods to avoid any pretreatment and unwanted reaction of sample with the attached labels, and to allow for *in situ* monitoring. There are several sensors that satisfy these requirements; electrochemical, optical, and piezoelectric.

### **1.6.1 Electrochemical Biosensor**

Electrochemical sensors are based on voltametric, potentiometric, or electrogenerated measurements [16, 69-73]. In voltametric measurement, hybridization between probe and target DNA can be detected by measuring changes in the peak current potential of the redox active molecule bound to the probe DNA. Potentiometric biosensors, usually made from silicon type capacitors, detect pH changes at the surface by using light emitting diodes [74-76]. Electrogenerated chemiluminescence is based on a chemiluminescence reaction initiated by an electrical stimulus.

## 1.6.2 Optical Biosensor

For detection of DNA hybridization, many of the optical biosensors use evanescent wave technology. The evanescent wave is an electromagnetic wave produced when light is reflected within the sensor surface. The sensor uses an optical fiber cable to transmit the excitation light to a fluorescent label and to receive the emission light. Probes are immobilized on the fiber optic cable. Hybridization is detected with a selectable dye on the target DNA [77-84].

Another similar method uses surface Plasmon resonance (SPR) phenomenon (see Figure 1.9) [85-92]. SPR occurs under very specific conditions for which the free electron cloud within a metal film is coupled and resonate with the evanescent wave of the incident light. The change of thickness on the surface due to hybridization can tilt the incident SPR angle. From the change of SPR angle, the degree of hybridization is determined.

## Surface Plasmon Resonance

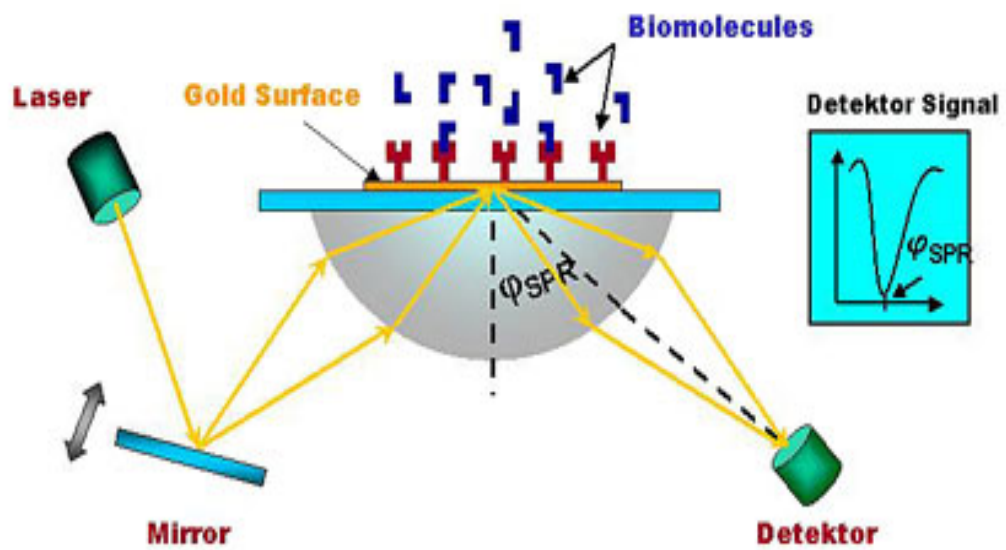


Figure 1.9 Schematic of Surface Plasmon Resonance biosensor [92].

### 1.6.3 Piezoelectric Biosensor

Piezoelectric biosensors have attracted attention because of their high sensitivity, accuracy, and effective signal with small change of mass due to hybridization [44, 93-98]. Piezoelectric substrates vibrate at a regular frequency when changing electric fields are forced upon them. The substrate is characterized by a resonance frequency for which the amplitude of vibration is maximum. The most common example of a piezoelectric biosensor is the quartz crystal microbalance (QCM)[ QCM is a direct, label free, detection approach that involves an oscillating quartz crystal with probe DNA immobilized on the surface. When hybridization proceeds, the increase in mass gives rise to a decrease in the oscillating frequency (see Figure 1.10). The change of oscillation frequency is described by the Saubrey equation.

$$\Delta f = \frac{2 f_0 \Delta m}{A(\mu_q \rho_q)^{1/2}} \quad (1.20)$$

Where;

$\Delta f$  : measured frequency shift

$f_0$  : resonant frequency of the fundamental mode of the crystal

$\Delta m$  : mass change per unit area

A : piezoelectrically active area

$\rho_q$  = density of quartz (2.648 g/cm<sup>3</sup>)

$\mu_q$  = shear modulus of quartz ( $2.947 \times 10^{11} \text{ g/cm} \cdot \text{s}^2$ )

However, QCM are typically large sensors that require large amounts of sample material. Other piezoelectric materials such as Si and GaAs, can be manufactured into micro electromechanical systems (MEMS) using photolithography technology. These materials are expected to have higher sensitivity than QCM resonators. Silicon resonators have several difficulties when exposed to an aqueous environment while most of the biological systems operate in aqueous environments. Also, their sensitivity is limited by the relatively low transduction strength afforded by a capacitive coupling for sensing and actuation of the resonators. Furthermore, relatively high voltages are required, leading to potential electrochemical instabilities which can affect measurement repeatability.

DeVoe and coworkers demonstrated piezoelectric micro- and nano-scale resonators with high amplitude narrow width at the resonance frequency fabricated from AlGaAs materials, which is almost lattice matched to GaAs(see Figure 1.11) [99-101]. This resonator can be used as a new sensor for detection based on a measurement of the change in resonance frequency upon hybridization. By employing piezoelectric transduction and high Q-device designs, the sensitivity is increased by over an order of magnitude compared to silicon devices.

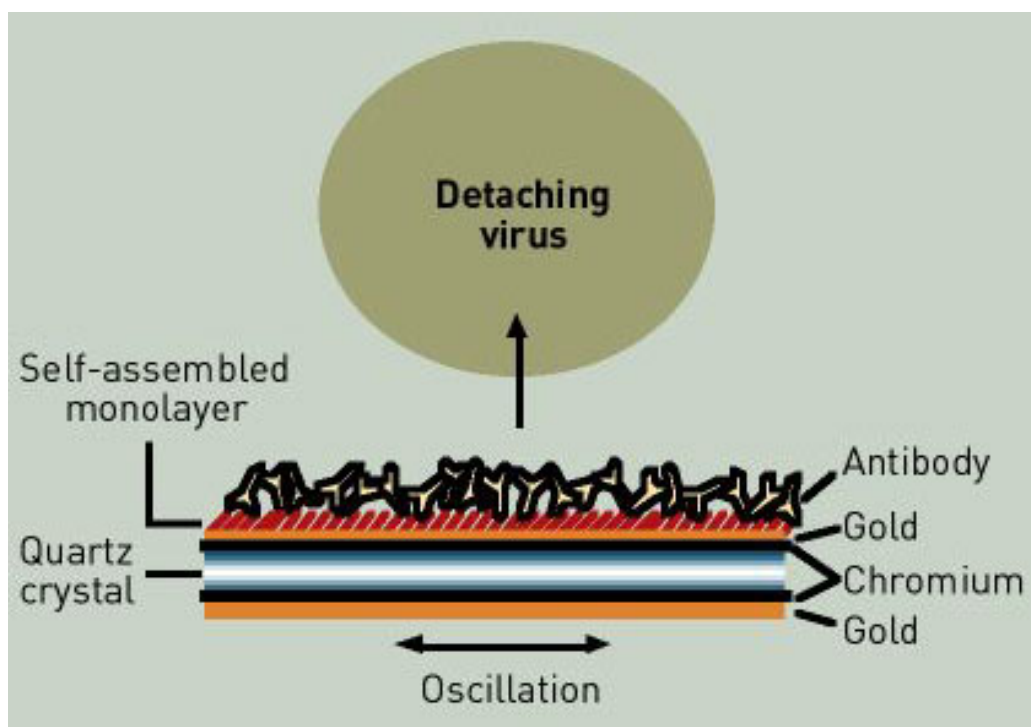


Figure 1.10 Quartz Crystal Microbalance (QCM) [102]

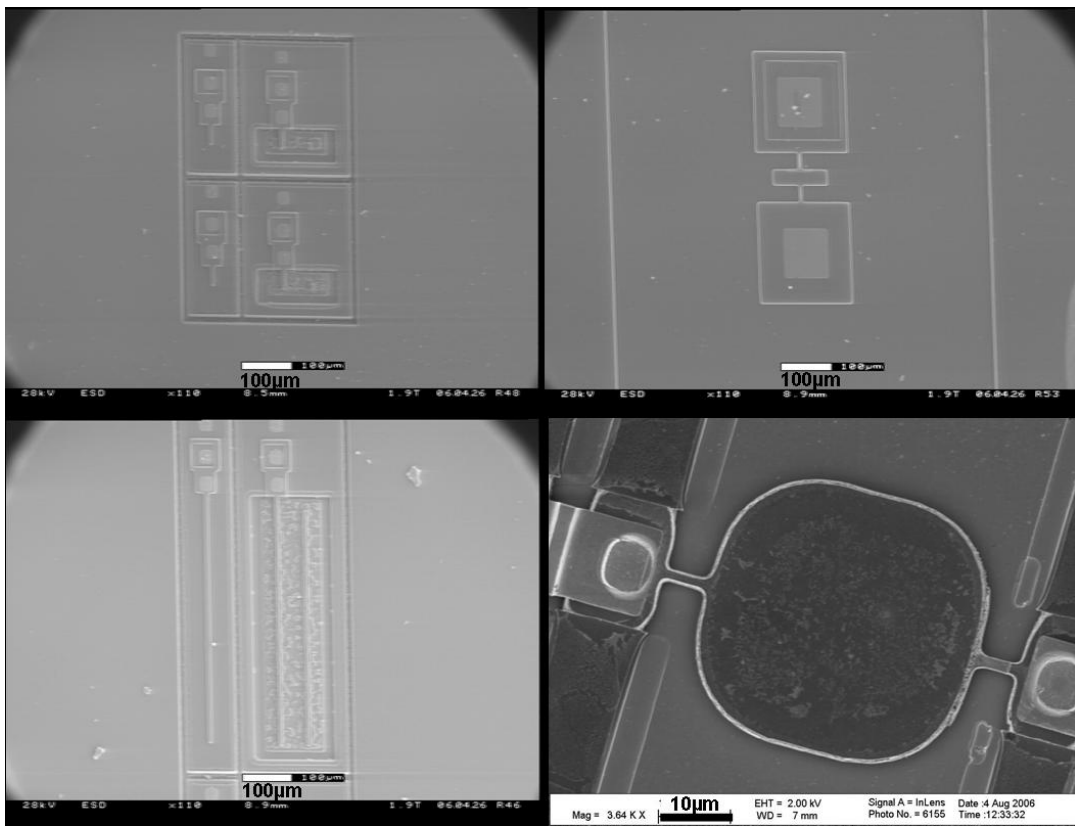


Figure 1.11 The SEM images of the different types of AlGaAs resonator used in this work.

## Chapter 2

### 2. Experimental Approach

#### 2.1 Materials and Sample Preparation

Thiolated eight base single-stranded DNA of sequence SH-(CH<sub>2</sub>)<sub>6</sub>-5''AGTCAGTC3' and 100 base ssDNA of sequence HS-(CH<sub>2</sub>)<sub>6</sub>-5'-(TG)<sub>50</sub>-3' were obtained from Oligos Etc (Wilsonville, Oregon) in the form of lyophilized powder and stored at -85°C. The sequence of DNA was chosen to prevent hybridization of the DNA in the solution. The 100-mers DNA were received in disulfide form which was cleaved by reacted with 0.1 M DTT at room temperature for one hour. After treatment of DTT, DNA was filtered and separated through a NAP-10 gel-filtration columns (Amersham Pharmacia) equilibrated with phosphate buffer solution. GaAs (001) obtained from AXT. Inc. (Fremont, California) was cut into 5 X 5mm squares, successively cleaned in trichloroethylene, acetone, and isopropyl alcohol using an ultrasonic cleaner and then dried with argon gas. To prevent the atmospheric molecular oxygen from reacting with the etched GaAs the whole procedure explained below was carried out using all aqueous solutions saturated with argon prior to use inside an argon filled glove bag. The cleansed substrate was etched in dilute hydrochloric acid to remove the first layer of gallium and the native oxide.

Immediately after etching the GaAs wafers were immersed in an aqueous solution of the desired concentration of DNA with phosphate buffer (0.06 g  $\text{KH}_2\text{PO}_4$ , 0.05g KCl, 2.0g NaCl, 0.36g  $\text{Na}_2\text{HPO}_4$ , and 250ml DI water) at a pH of 7.8 for 24 hours. After DNA attachment some samples were immersed in various concentration 6-mercapto-1-hexanol (MCH) spacer solutions for one hour. In order to remove any DNA oligonucleotides or MCH molecules that were not covalent bonded to the As terminated surface. The samples were cleaned by using ultrasonic cleaner and rinsed in running DI water.

## **2.2 Characterization Techniques**

### **2.2.1 Atomic Force Microscopy (AFM)**

The atomic force microscope (AFM) has become a very important characterization tool in many fields since G. Binnig and co-workers invented it in 1986 . The AFM scans over a surface by using a fine ceramic or semiconductor tip. Typically, the tip is located at the end of a cantilever with a laser beam focused at the end of the cantilever. As the tip is either repelled by or attracted to the sample surface, the cantilever deflects which results in a change of the laser beam position on a photodiode.(see Figure 2.1) The photodiode detects the relative position of the laser on the photodiode face. The photodiode is composed of two major parts which separately detect normal motions and shear motions. The top half and bottom half of the photodiode detect normal and shear motions respectively by the laser

displacement along the x axis of the photodiode. A plot of the laser deflection versus tip position in the x,y, and z directions on the sample surface provides 2 or 3 dimensional surface images. A sensitive piezoelectric element controls the position and motion of the tip over the surface of the substrate.

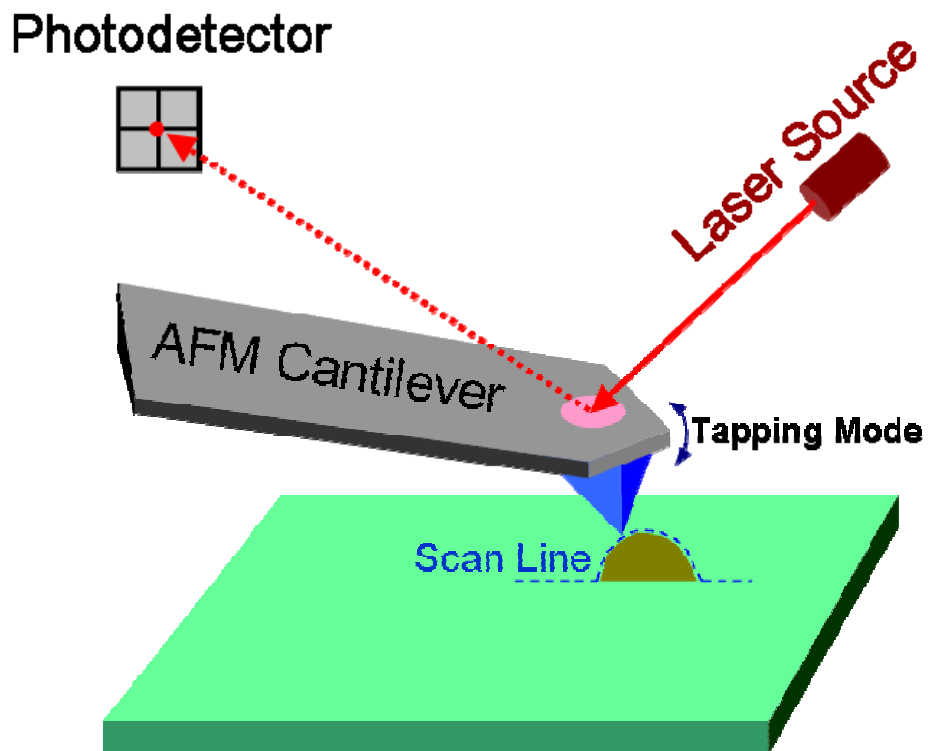


Figure 2.1 Schematic of an Atomic Force Microscope

Atomic force microscopy can be divided into three major modes of operation; contact, non-contact, and tapping mode. In contact mode, the tip is placed in direct contact with the surface. The deflection of the cantilever is generated by a variation of the surface topography. In the case of biological or polymer samples, which are soft and easily damaged, contact mode might not be good characterization method due to tip induced sample damage.

The second technique, non-contact mode, was developed to investigate soft sample surfaces. The AFM tip is held at a distance in the range 3-15 nm above a surface and this space is maintained constant by using the force signal. As the tip is scanned over a sample surface, long range attractive forces acting between the tip and the sample are detected, and a topographic image is recorded.

The last technique is tapping mode. A cantilever is oscillated at its resonant frequency and is in contact with a surface for only a very small fraction of its oscillation period. This is probably the most useful mode of operation for biological applications.

AFM imaging can be performed under vacuum, air, and liquid conditions and it can image biological samples in three dimensions. The AFM has successfully been used to image individual and macro biological molecules, such as amino acids, proteins, and DNA. In this work, AFM ( D-3000 model, Digital Instruments Inc.) was employed as an analytical tool to evaluate the surface morphology and roughness of

the DNA layer attached to the surface of GaAs-based semiconductors in air and liquid conditions utilizing a fluid cell.

### **2.2.2 X-ray Photoelectron Spectroscopy (XPS)**

X-ray Photoelectron Spectroscopy (XPS) provides information on the elemental contents and chemical bonding states at the surface region of a sample up to 20 nm thick (excluding hydrogen and helium). A photon of high energy (short wavelength) can excite an atom, producing an ejected free electron. (see Figure 2.2) The kinetic energy  $E_k$  of the ejected electron (photoelectron) depends on the energy of the photon  $h\nu$  by the Einstein photoelectric law:

$$E_k = h\nu - E_b \quad (2.1)$$

Where,  $E_b$  is the binding energy of the particular electron in the atom being excited. Since  $h\nu$  is known, a measurement of  $E_k$  determines  $E_b$ . Considering the energy loss during the excitation process due to the specific instrument,

$$E_k = h\nu - E_b - \Phi \quad (2.2)$$

Where,  $\Phi$  is the work function of the instrument. The binding energy of the electrons is related to the chemical state of a specific atom. The probability for photoejection

from each orbital of an atom is different and it can be characterized by the photoionization cross section  $\sigma$ . This probability also varies for a given orbital in different atoms and depends on the X-ray energy used. Thus, an XPS spectrum contains a number of peaks according to different  $E_b$ . The position of the peaks directly identifies the orbital of the atom concerned, the intensity of the peaks depends on the number of atoms present and on the  $\sigma$  values for the corresponding orbital.

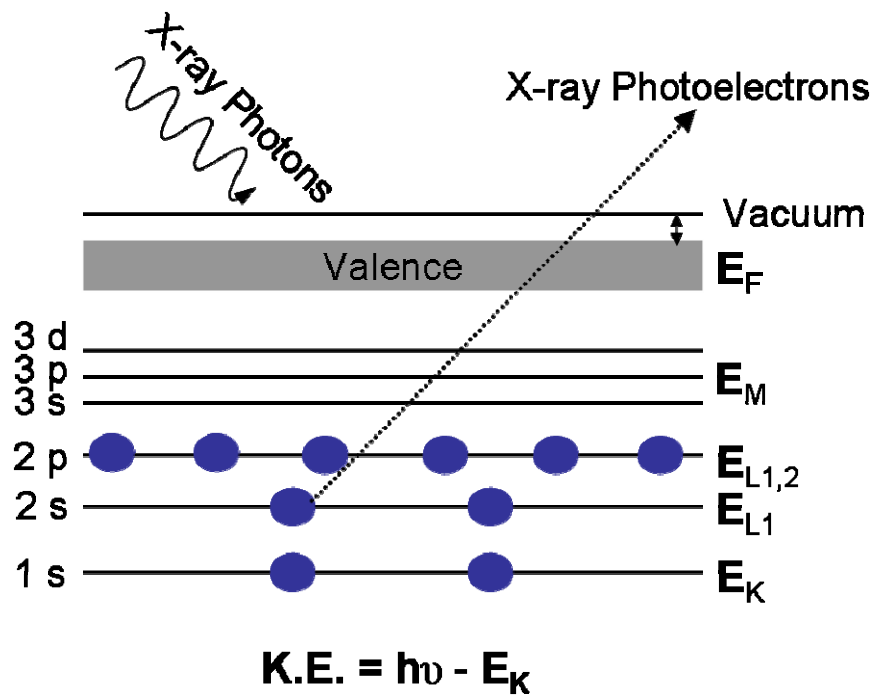


Figure 2.2 X-ray excite core shell electrons

### ***Atomic concentration***

Figure 2.3 shows one example of an XPS spectrum of C 1s peak. The area under the peak can be determined by subtracting the baseline and integrating the area under the curve. The integrated area is the measured photoelectron peak intensity for C 1s in counts per second. To compare the relative quantities of the elements present, a sensitivity factor can be used. This factor relates a number of collected electrons to the amount of a particular element present. It depends on the photoelectron cross section and the instrument response function and is different for each element. The atomic concentration can be calculated as:

$$C_i = \frac{100 N_i / s_i}{\sum N_i / s_i} \quad (2.3)$$

Where;

$C_i$  : Concentration of element  $i$  in %

$N_i$  : Total counts of element  $i$

$s_i$  : Sensitivity factor of species  $i$

In this study, XPS was used to obtain the type of chemical bonding between the DNA oligos and the GaAs substrate in atomic percentage. The measurement was

done using a Kratos AXIS 165 model at UMCP Department of Chemistry and Biochemistry.

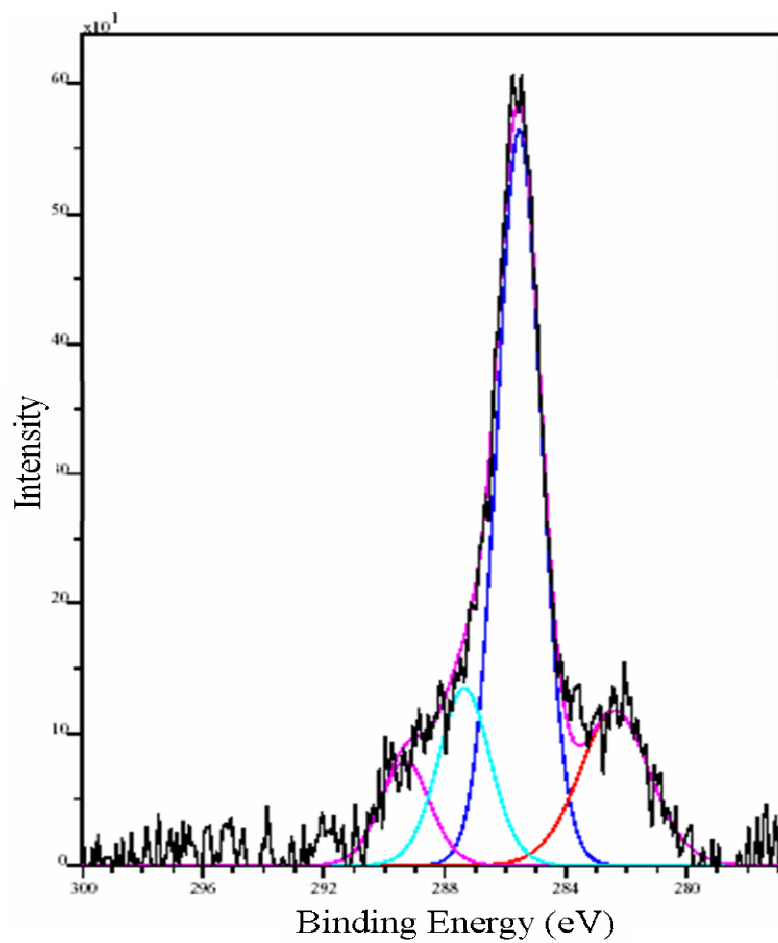


Figure 2.3 XPS spectrum of C 1s with curve fitting

### **2.2.3 Field Emission Scanning Electron Microscopy (FESEM)**

FESEM has a field-emission cathode inside the electron gun chamber. The field emission cathode allows generation of a narrow probing beam at low as well as high electron energy. This improves spatial resolution and minimizes sample charging and damage. Spatial resolution can be as high as 1.0 nm. That is 3 to 6 times better than a conventional SEM. Accelerating voltages range from 0.5 to 30 kV, and low voltage images are obtained with negligible electrical charging of samples, such as insulating materials or biological samples. The surface of the GaAs containing DNA monolayer was investigated by a ZEISS SUPRA 55VP FESEM model at Georgetown University..

### **2.2.4 Grazing Incidence X-ray Scattering**

The X-ray experiments will be performed using a Rigaku rotating anode source operating at 50kV and 100mA, using Cu K radiation (energy 8.8KeV), with a bent graphite monochromator. The resolution used is  $0.017q_0$ . Samples will be mounted in a four-circle diffractometer ( $2\theta, \theta, \varphi, \chi$ ). Two types of experiments will be performed. In the GIXS experiment the substrate and samples will be oriented at  $\chi = 0^\circ$  so that the experiment will be performed in the plane of the GaAs substrate. The tilt of the DNA with respect to the substrate plane,  $\Psi$ , will be determined for DNA base pairs larger than 16 by comparing the observed persistence length,  $R_{obs}$ , to the experimentally determined persistence length,  $\Psi = \arccos(R_{obs}/R_{theor})$  where,  $R_{theor} =$

$0.38(N/3)^{1/2}$ . GIXS is a physical probe, which will complement the findings from the chemical probes.

## **2.3 Linear Accelerator Facilities**

The irradiation to DNA layer was carried out using a Varian electron beam linear accelerator (LINAC) capable of producing 1 to 8 MeV beam energy at the University of Maryland. Electron emission is produced by heating of a filament. The electrons are ejected into an input cavity of the accelerator waveguide structure (~1.5 m in length) in pulses of approximately 3 microsecond ( $\mu$ s) at a continuous variable repetition rate of up to 550 pulses per second at a pulse level of approximately 80 kV. In these experiments, 3  $\mu$ s pulses with 7 MeV beam energy were produced at a dose rate of 30~70 Gy/pulse for the samples. The absorbed dose by a sample was determined by the radiochromic film dosimetry system ( FWT-103, Far-West Technology Inc). The change in optical absorbance of film after irradiation was examined by a spectrophotometer ( Beckman<sup>TM</sup> DU Series 7000 ).

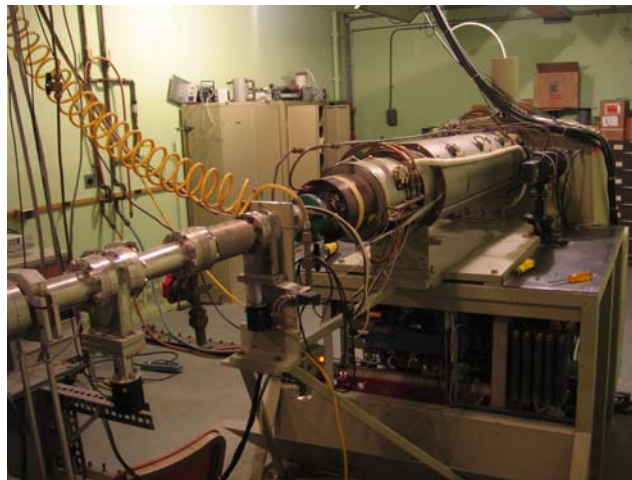
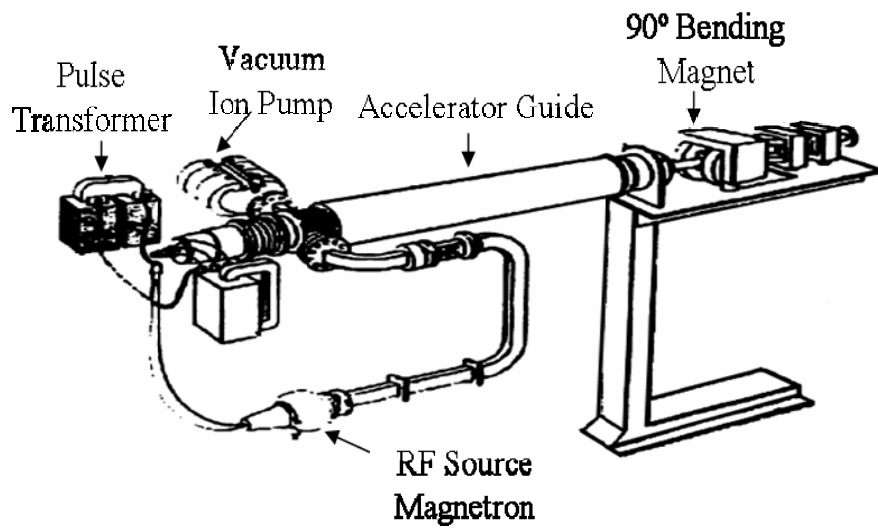


Figure 2.4 Top schematic of Major Fictional Components of a Varian Linear Electron Beam Accelerator (LINAC) (bottom) at the University of Maryland.

## Chapter 3

### 3. Immobilization of Oligonucleotides on GaAs Surface

#### 3.1 Introduction

Recently, immobilization technique is the core for the development of biochips and biosensors. In addition, various substrates have been used including metallic materials, polymer-based materials, silica-based wafer and GaAs-based semiconductors. The first solid-support for DNA was proposed by researchers at University of Wisconsin in Madison in 1996. After that, it developed very quickly with different methods to attach oligonucleotides to a variety of solid substrates. The most effective and widely used method utilizes the covalent bond between 5'-end thiol modified oligonucleotides and the substrates. Many studies have shown that Alkyl thiols, such as,  $\text{HS}(\text{CH}_2)_n\text{X}$  (end group X can be  $\text{NH}_2$ ,  $\text{COOH}$  or  $\text{OH}$ ) form densely packed monolayers with certain orientation published by Bain and Whitesides in 1989 [24]. The monolayers are very stable because of the strong covalent bond ( $\sim 44\text{kcal/mol}$ ) between the sulfur at the head group and the gold atoms. The oligonucleotides can be modified with thiol (H-S) or disulfide (S-S) group at the ends. The thiol molecules adsorb in random clusters during the first stage, and then the molecules assemble over the reconstruction site of gold surface in a similar manner to the bulk lattice. The study of surface chemistry of thiolated ssDNA monolayers on gold surface was researched by Tarlov and co-workers [27]. They also studied the MCH treatment as a spacer to obtain a better organized brush-like

structure. They propose that MCH post treatment could displace the non-specifically adsorbed DNA from the gold surface as well as prevent non-specific adsorption of the DNA.

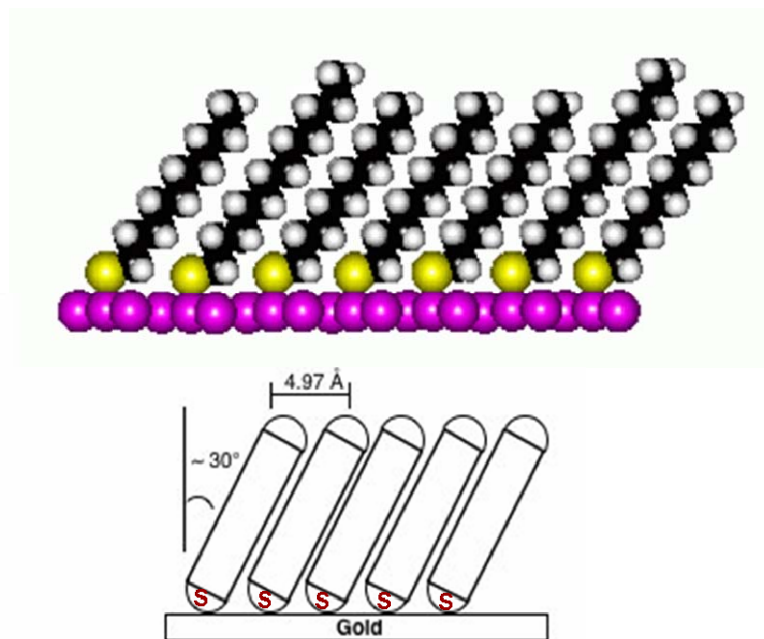


Figure 3.1. Schematic of tightly packed monolayer of long-chain thiol molecules on Au (111) [24]

In this chapter, the use of non-modified and thiol modified oligonucleotides are presented in regards to the attachment on GaAs surfaces. After attachment of DNA, the effects of cleaning method, the presence or absence of spacers, and environmental conditions are explored. AFM and FESEM method for visualizing the DNA layer on GaAs were employed. Moreover, XPS and GIXS techniques are used to examine the structure of the immobilized DNA layer. The results of this work impact upon the development of biosensors using immobilized DNA or protein modified surfaces.

### **3.2 Experimental Material**

All oligonucleotides were purchased from Oligos Etc (Wilsonville, Oregon) in the form of lyophilized powder and stored at -85°C. I used non-modified, 5' thiol-modified 8-mers, and 5' thiol-modified 100-mers for all specific attachment experiments. The specific sequences of each type of DNA listed in Table 3.1. The sequences of DNA were chosen to prevent hybridization of the DNA in the solution.

Table 3.1 Sequences of oligonucleotides

Oligonucleotides	Sequence
8-mers	5'-AGTCAGTC-3'
Thiolated 8-mers	HS-(CH <sub>2</sub> ) <sub>6</sub> -5'-AGTCAGTC-3'
complementary DNA 8-mers	5'-GACTGACT-3'
Thiolated 100-mers	HS-(CH <sub>2</sub> ) <sub>6</sub> -5'-(TG) <sub>50</sub> -3'

### 3.3 Thiol Modification Effects for Immobilization

#### 3.3.1 Attachment of Non-Modified DNA

The GaAs (001) wafers were purchased by customer order specifically for lower surface roughness than commercial products. The smoother surface allows for increasing uniformity of the DNA layer morphology. To investigate the surface changes of attachment the DNA probes, AFM was employed to investigate the surface roughness of a cleaned bare GaAs substrate. GaAs was cut 1 cm X 1 cm size and cleaned and etched with dilute HCl as described before. After that GaAs was rinsed by running DI water and dried by argon gas. AFM scan was carried out at room temperature and under atmospheric conditions. The AFM image of the bare GaAs (001) plane surface and cross-sectional line profile are presented in Figure 3.2. The scan area was 500 nm X 500 nm, and to obtain better statistics on the surface roughness measurement of at least 5 different areas were examined per sample. For each scan, dimension statistical data were extracted from 60 different scan lines of scanned area. The typical expression of roughness is given in terms of the Root mean square (RMS), which was directly determined from the height data.

$$RMS = \sqrt{\frac{\sum (Z_i - Z_{arg})^2}{N}} \quad (3.1)$$

Where  $Z_i$  is the surface height at point  $i$ ,  $Z_{avg}$  is the mean value of  $Z_i$  and  $N$  represents the number of points sampled

Form Figure 3.2, the RMS of the bare GaAs surface is  $0.3 \text{ nm} \pm 0.1 \text{ nm}$ . This result shows that even though the surface was etched to remove the natural oxide layer, slight roughness of the surface still remained. The As-rich dimmer rows and trenches of the  $2 \times 4$  reconstructed GaAs surface were not clearly observed. The reason for this is the thin natural oxide layer formed during the AFM scan in air and depth penetration limit of AFM tip. The  $2 \times 4$  reconstructed surface is only observed in vacuum after desorption of the oxide large at high temperatures.

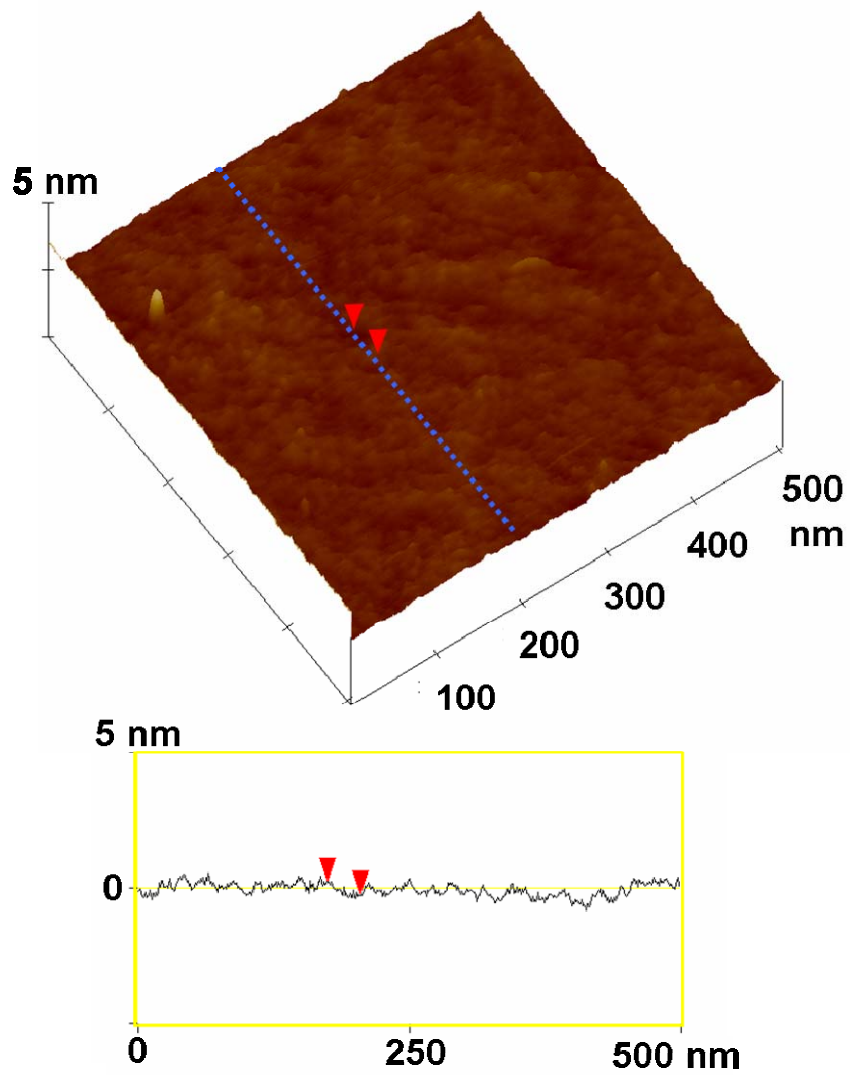


Figure 3.2 AFM images of the bare GaAs (001) plane surface (500 nm X 500 nm) and cross-sectional line profile.

Figure 3.3 is a 500 X 500 nm AFM image of the surface of GaAs after immersion for 24 hours in a 60  $\mu$ M solution of non-modified 8-base DNA (5'-AGTCAGTC-3'). 8-mer single strand DNA behaves like a rigid rod with 3.5 nm contour length and  $\sim$ 1 nm width. The significantly changes in the images compared to the bare GaAs surface (see Figure 3.2) were observed. The surface is covered with ssDNA bundles with distorted round or elliptical shape. The average width of those is about  $\sim 20.4 \pm 5.5$  nm, and the difference in of height difference between the red indicators in Figure 3.3 (c) cross-sectional line profile is 8.2 nm. This value is larger than the dimensions of individual single stranded DNA. Although the AFM tip makes the measured size bigger than the actual size of DNA layer is known as dilatation effect induced by tip radius, this result indicates that along the several DNA strands form the bundles. The AFM image also shows that DNA prefers to deposit along the of the GaAs [110] direction which corresponds to the direction of the As-rich dimer rows. Ladan et al. reported that the nitrogen or oxygen of the bases of DNA also bond with the arsenic atoms on the surface. This suggests that non-modified DNA is preferentially lying down following the As-rich dimer rows through bond between the base of DNA and the arsenic atom on the surface(Figure 3.3 (d)). In addition, the thickness of the DNA layer revealed that some interaction  $\pi$ - $\pi$  interactions existed between DNA molecules to hold each other In DNA,  $\pi$ - $\pi$  interactions occurs between the nitrogen in the bases of the neighbor DNA, oligos consisting of aromatic rings [103, 104]. The faces of aromatic rings will overlap their  $\pi$  orbitals. Even though this interaction is weaker than covalent bonding, the total sum of  $\pi$ -  $\pi$  interaction can not be neglected.

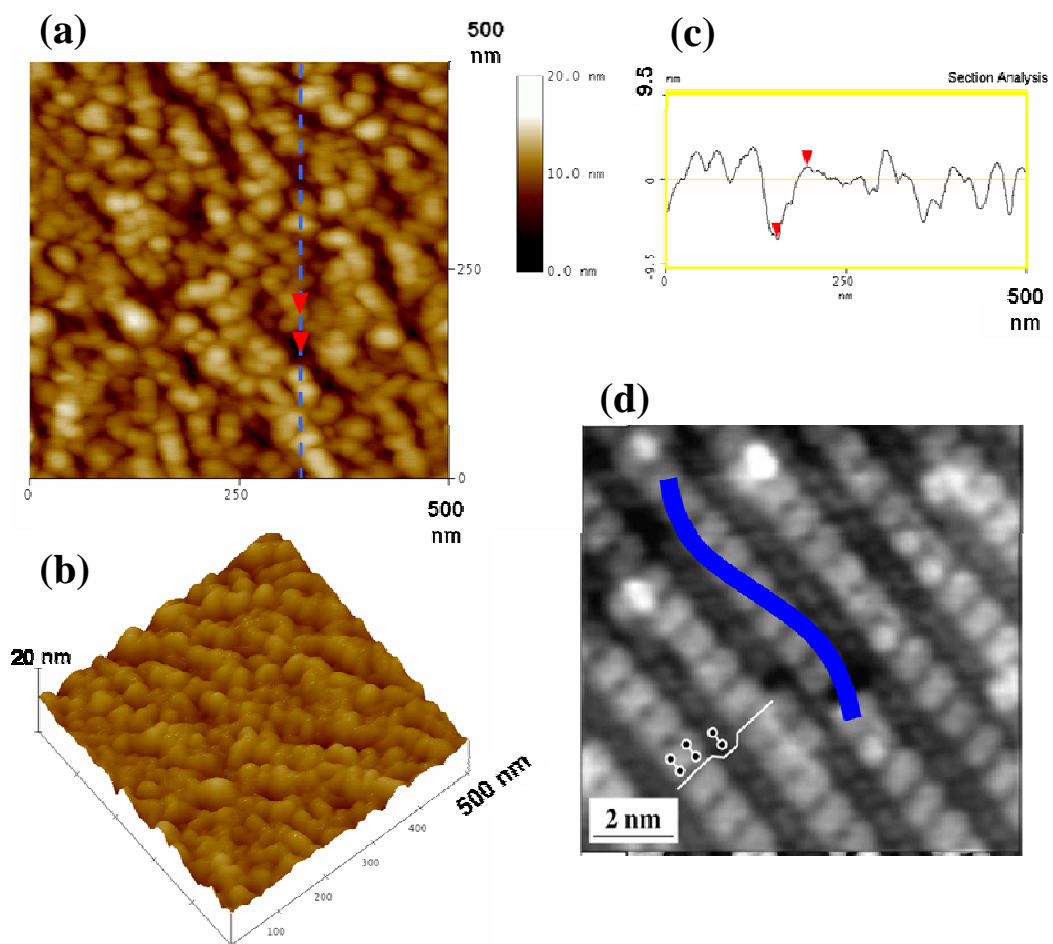


Figure 3.3 AFM images of single stranded DNA without thiol-modification layer on GaAs (001) surface imaged in (a) height mode, (b) three dimensional view, and (c) cross-sectional line profile. The schematic in (d) illustrates the preferred orientation of DNA on the GaAs surface.

### **3.3.2 Attachment of Thiol-Modified DNA**

#### **3.3.2.1 Sonication Cleaning Method**

The 8-base thiolated ssDNA is used to achieve brush like layer structure of DNA probes layer. The sulfur in thiol group is expected to bond covalently with the arsenic atoms on the surface. Figure 3.4 shows schematics of the immobilized DNA probes and the bonds of the desired S-As and undesired O-As and N-As DNA to As of the As-terminated GaAs. During the attachment procedure, non desired bonds and adsorption usually occur both of DNA strands with each other and between DNA and the substrate (see Figure 3.4). The undesired bonds can not be easily removed or broken by simply washing with running water or buffer solution. Several techniques can be applied for better result of cleaning the immobilization surface, such as using heated water or ultrasonic cleaner. However, some reports indicated that the non desired bonds and adsorption would still remain on the surface even after heating to 75°C.

On the other hand, I found that ultrasonic cleaning was more effective to remove the non desired bond and adsorption. AFM observation was carried out to investigate the change in morphology of the rod shape DNA oligos before and after sonication cleaning. Figure 3.5 shows change in the surface morphology before and after ultrasonic cleaning for 60  $\mu$ M DNA sample on the GaAs (001) by AFM tapping mode in air. Before ultrasonic cleaning, the AFM image (2 x 2  $\mu$ m) (Figure 3.5 a)

shows that the surface is covered big by DNA bundles with  $\sim 70$  nm size and  $\sim 5$  nm in height.

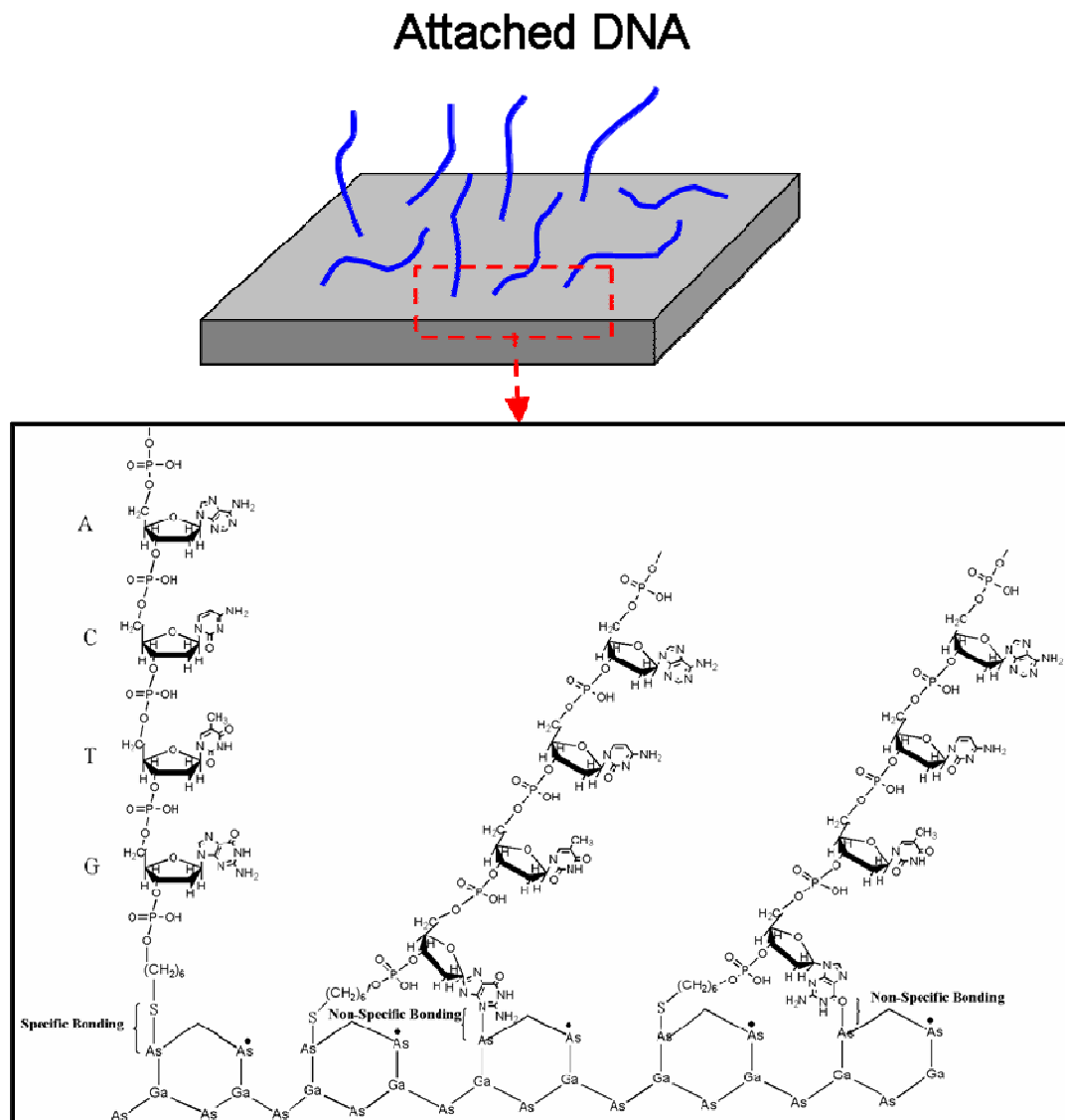


Fig 3.4. Schematics of immobilized DNA probes and the bonds of the desired S-As and undesired O-As and N-As DNA to As of the As-terminated GaAs

Since the contour length of the DNA is only 4.6nm, this result indicates that extra DNA molecules still remain on the surface even after the surface rinsing with running DI water. As shown in Figure 3.5 (b) and (c), the ultrasonic cleaning is more effective at removing the non desired bonds and adsorption. This figure shows that DNA bundle are smaller and their height is greatly reduced and more uniform. The cavitation from ultrasonic and high intensity sound waves through the water or buffer solution removed the weakly adsorbed DNA without removing the strong covalent bonds of the immobilized DNA on the surface. Cavitation is the phenomenon of rapid formation and violent collapse of bubbles and cavities in water and buffer solution. The ultrasonic energy has sufficient intensity to create small water bubbles that collapsed or implode very fast. These events create a very effective force which can help removing the non specific bonded DNA and extra DNA molecules. Inside the bubbles, a pressure and a temperature can be calculated theoretically to be more than 10,000 psi and 20,000 °F [105, 106]. Thus, under such extreme conditions, some non specific bonds on the surface after immobilization could be broken. The ultrasonic cleaning depends on two major factors which are wave frequency and treating time. With increasing wave frequency, the total number of cavities increases. The energy of each collapsing cavity, however, decreases. Consequently, higher frequency provides less energy to the surface. On the other hand, at affixed frequency, longer time of sonication provides more energy to the surface.

Figure 3.5 (b) was taken from a dried sample after ultrasonic cleaning for 20 minutes. The image shows a uniformly array of needle like DNA oligos forming a

layer on the surface. The high resolution image in Figure 3.5 (C) shows the DNA oligos forming a dense array of slightly elliptical shape bundles with an average width of  $\sim 14.6 \pm 2.6$  nm. Because of the shape and size of the AFM tip, however, it is most likely that the tip does not reach the GaAs surface during image acquisition. As a result one would expect the measured height of DNA brush obtained from AFM to be shorter than the real value (Figure 3.5).

In order to determine more accurately the average height of the DNA brush a high force was used on the AFM tip in contact mode to remove the DNA from the surface. For scratching the DNA monolayer, a rectangular area ( $500 \times 250 \text{nm}^2$ ) was selected and then the set point voltage increased until the desired force but low enough was applied to the tip. The force should be high enough to break the S-As bonding to prevent scratching of the GaAs substrate. From a literature review, force required to break covalent bonding is several nano-Newtons. For example, a force of is necessary to break 3.7 nN to break carbon-carbon covalent bonding. In nanoindentation chose experiments of bulk GaAs, a force of the 500nN is typically used for minimum force [107-110]. I chose approximately a force of 50~100nN for removing DNA layer. Figure 3.6 (a) shows a calibration plot for the force in terms of the signal deflection as a function of Z. The force can be calculated from the spring constant of a cantilever and Z using the expression.

$$F = -kZ \quad (3.2)$$

where  $k$  : spring constant of the cantilever (0.9 N/m)

$Z$  : a distance of piezo movement after touching a surface ( $\sim 75\text{nm}$ )

In the present experiment, the force is approximately 67nN.

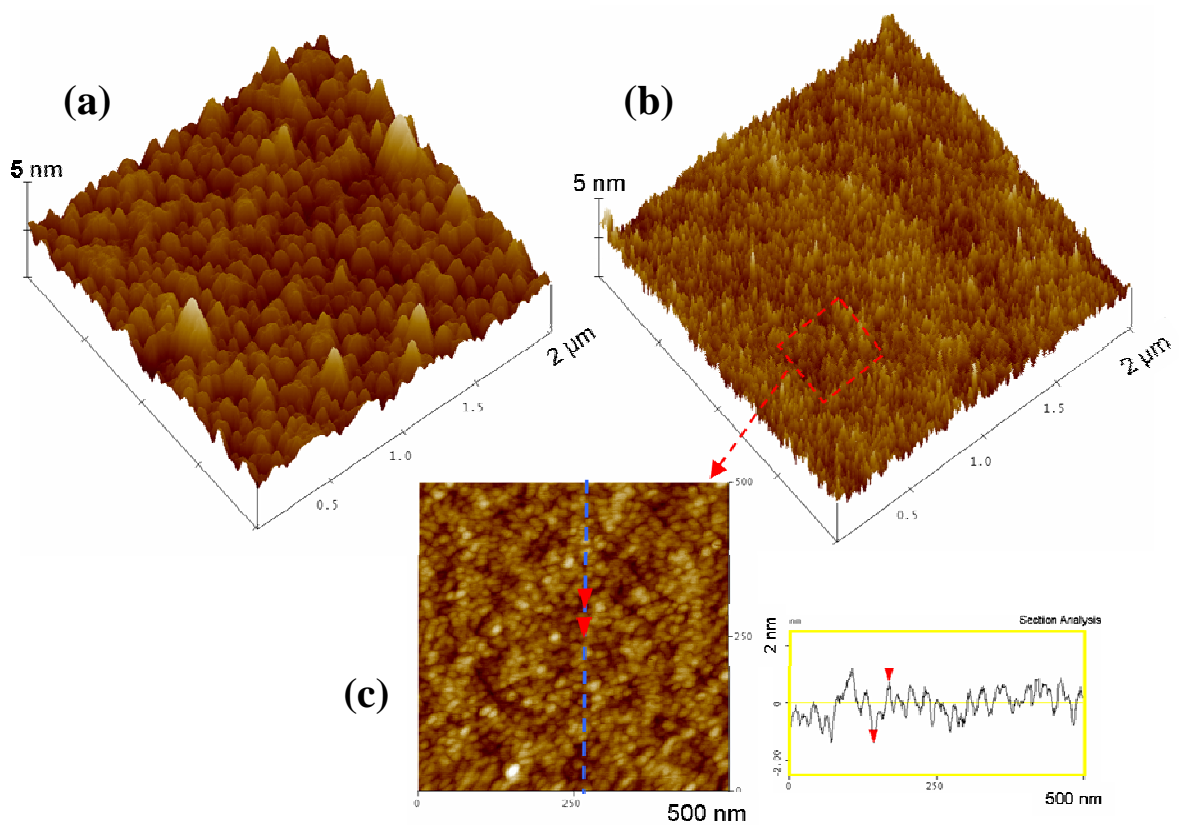


Figure 3.5 AFM images of the immobilized thiolated ssDNA layer on GaAs surface (a) after rinsing with DI water without sonication and (b) after ultrasonic cleaning. Dimensions are 2 X 2  $\mu\text{m}$ , z scale is 5 nm. (c) is high resolution scan (500 X 500 nm) of (b) and the cross sectional line profile.

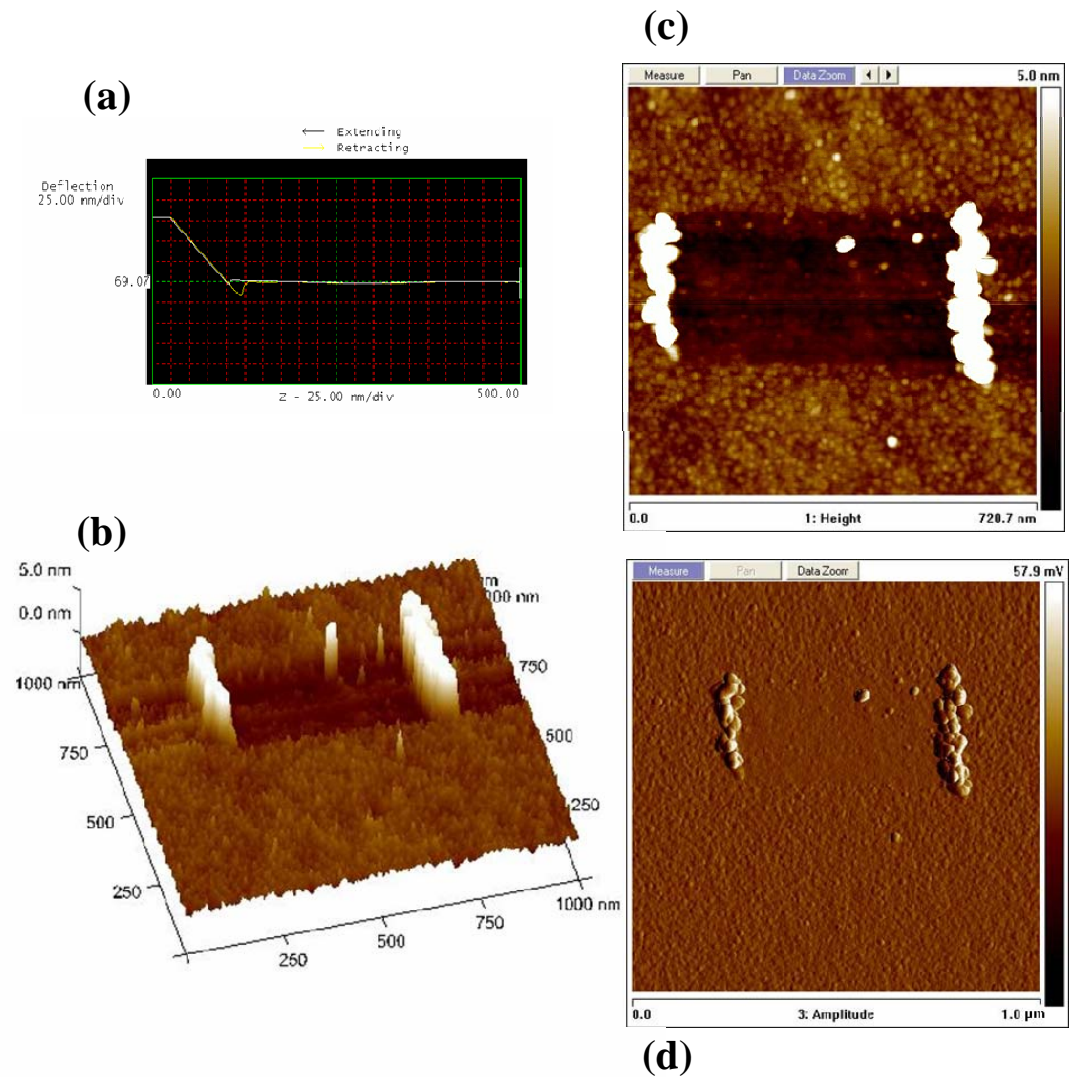


Figure 3.6. (a) Force calibration plot in terms of signal deflection as function of  $Z$ . AFM topographic images of (a) a sample containing  $60 \mu\text{mol L}^{-1}$  DNA on As-terminated GaAs (001) substrate. The scan is  $1,000 \times 1,000 \text{ nm}^2$  and the vertical scale is  $5 \text{ nm/div}$ . The scan was obtained from a dried sample in tapping mode after removing the DNA from a region of  $500 \text{ nm} \times 250 \text{ nm}$  using the AFM tip in contact mode with a force of approximately  $70 \text{ nN}$ . (b) three dimensional view, (c) plan view, (d) and phase image.

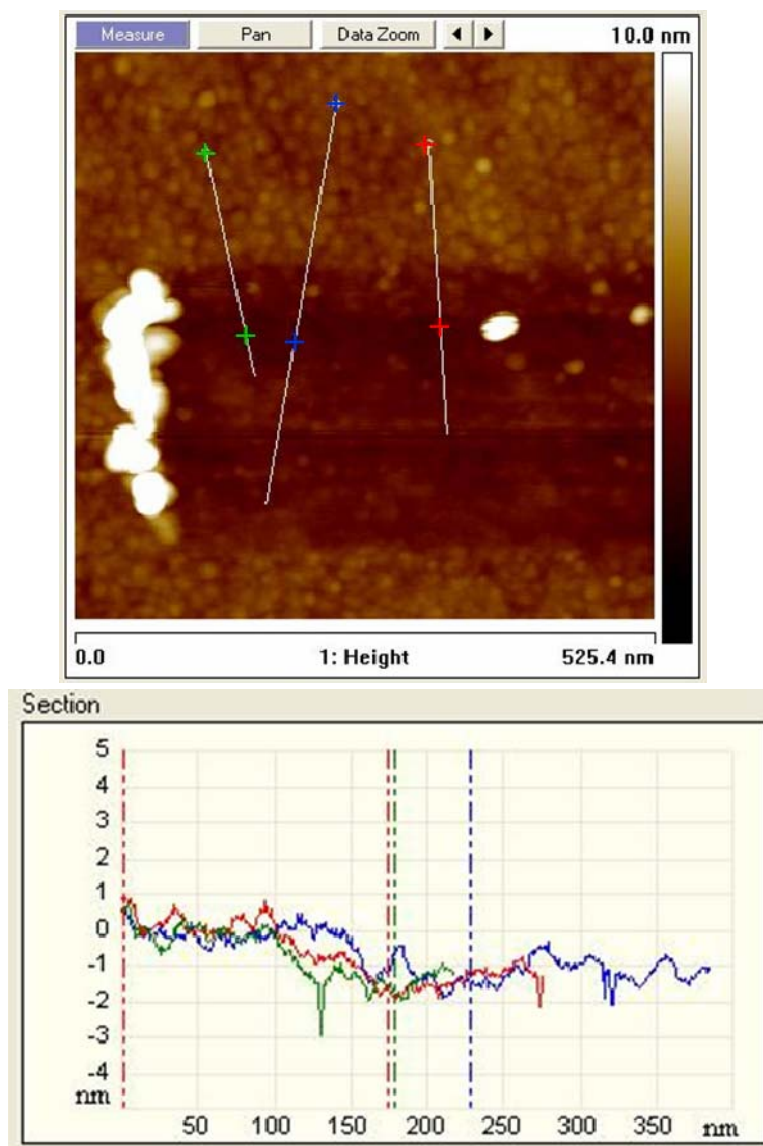


Figure 3.7 AFM image of plane view and height profiles from the scratched area in Figure 3.6 (b)

The AFM image in Figure 3.6 shows the exposed GaAs surface in the region where the DNA was removed surrounded by a fairly regular array of bundles of DNA. Figure 3.6 also shows pile up of the DNA at the two boundaries of the region where the DNA was removed and in the direction of the scanning. In a separate experiment the same force was applied to a bare GaAs sample and no damage was detected. The height of the DNA bundles in Figure 3.6 was measured with respect to the bare GaAs surface with an average of  $\sim 2.2 \pm 0.4$  nm. Based on the contour length of the SH-(CH<sub>2</sub>)<sub>6</sub>-5'AGTCAGTC3' of 4.621 nm this height indicates that the DNA oligos lie at an angle of  $\sim 28.4^\circ$  with respect to the surface of the GaAs. To investigate if the DNA showed any preferred in-plane orientation with respect to the  $\langle 110 \rangle$  directions of the GaAs substrate the sample was mounted with the  $\langle 110 \rangle$  direction (As-As dimer row direction) of GaAs at approximately 45 degrees with respect to the scanning (horizontal) direction of the AFM tip. Figure 3.7 shows that the bundles are elongated along the  $[1\bar{1}0]$  direction of the GaAs. This is in agreement with Ladan et al.'s previous XRD result on the 28 base ss-DNA attached to GaAs which showed that the DNA oligos preferentially align along the 0.7 nm wide trenches of the reconstructed  $2 \times 4$  surface structure of the As-terminated GaAs substrate.

### 3.4 Spacer Effects to Immobilization DNA layer on GaAs Surface

The brush-like structure of the DNA monolayer is essential for biosensor applications. To improve the layer quality, Tarlov's group at the National Institute of Standards and Technology (NIST) have shown that the monolayer formed from mixtures of thiolated DNA and short length thio molecules, such as mercaptohexanol (MCH) form a more uniform brush like structure. MCH leads to displace non-specific interactions of the DNA. A schematic showing the mechanism is presented in Figure 3.8 for DNA attached to GaAs. These mixed monolayers were found to have enhanced hybridization efficiency.

Figure 3.9 shows the dried surface morphology of a 60 $\mu$ M DNA treated with 60mM MCH on the GaAs. The line profile shows that the average height of the DNA bundles is  $3.3 \pm 0.3$  nm, and plane view image shows that the elliptical shape of DNA bundles has an average width of  $\sim 13 \pm 1.8$  nm. Comparing the results of the sample with no MCH Figure 3.6 to the ones with MCH, we see that Figure 3.9, the height increased from  $2.2 \pm 0.4$  nm to  $3.3 \pm 0.3$  nm and the diameter of the DNA bundles slightly decreased from  $14.6 \pm 2.6$  nm to  $13 \pm 1.8$  nm with the addition of MCH. These dimensional changes after addition of MCH indicate that the immobilized ssDNA layer has more brush-like structure because the MCH molecules substituted the N-As and O-As bonds with S-As bonds. A quantitative study of the displacement reaction of MCH is discussed in chapter 3.5 using XPS.

To confirm the AFM results, high resolution FESEM was employed. Figure 3.10 shows the surface morphology of (a) unmodified ssDNA, (b) thiolated ssDNA, and (c) a mixture of thiolated ssDNA and MCH samples. In the un-modified ssDNA sample, no DNA bundles were observed. The image agrees with the AFM image of the same sample in Figure 3.3 which indicated that the DNA molecules laid on the surface. On the other hand, smaller bundles of DNA were observed in the modified DNA samples in Figure 3.10 (b) and (c). For each sample, the size of the bundles are  $13.7 \pm 0.9$  nm for thiolated ssDNA only sample and  $10.5 \pm 0.8$  nm for post treated MCH sample. These results are slightly smaller than AFM results. This can be explained by the convolution of the shape of the AFM tip with the sample profile. It is also possible that during the AFM scan, the AFM tip could compress slightly the top of the DNA bundles.



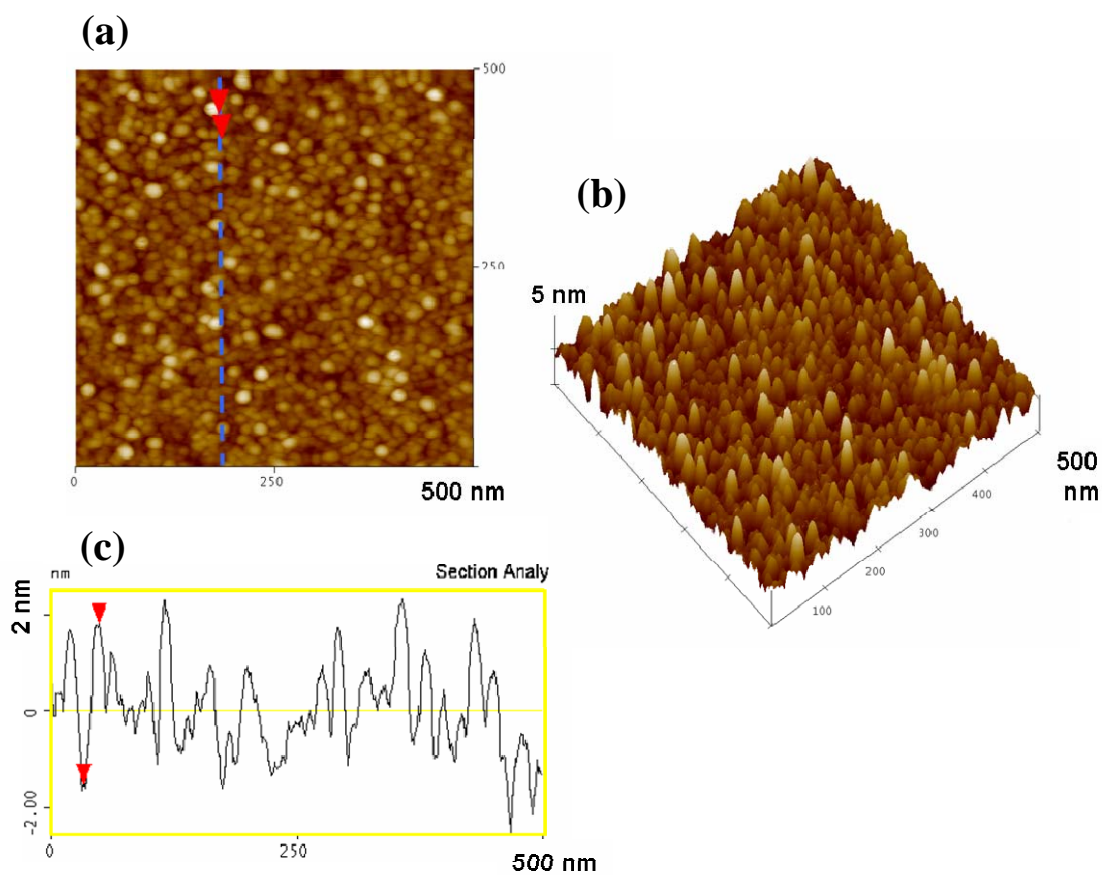


Figure 3.9 AFM image in dry mode of  $60 \mu\text{mol L}^{-1}$  DNA and post treated mercaptohexanol (MCH) on As-terminated GaAs (001) substrate. Plane view (a), three dimensional view (b), and line profile (c).

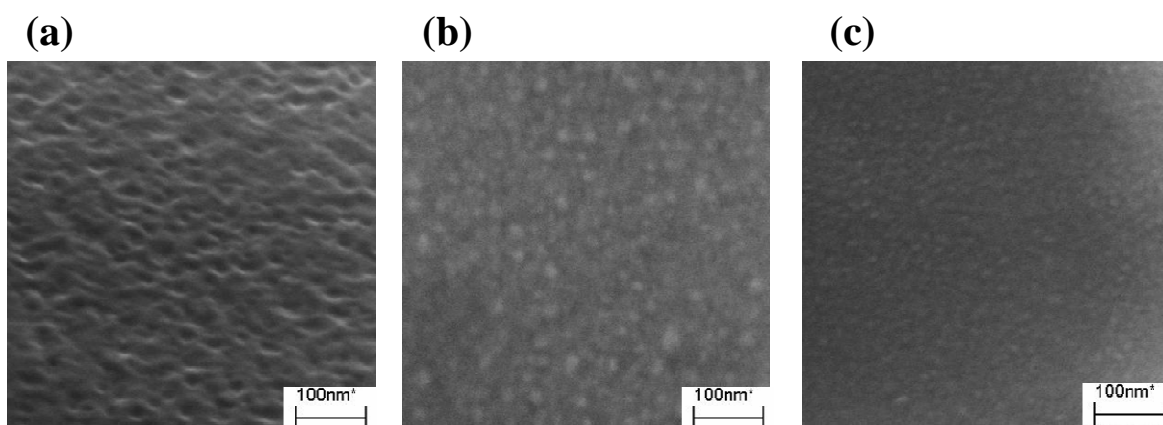


Figure 3.10 Surface morphology of FESEM images (a) non-modified ssDNA layer, (b) thiolated ssDNA layer, and (c) treated with MCH of thiolated ssDNA sample.

To investigate the structure and orientation of the immobilized DNA layer, grazing incidence X-ray scattering (GIXS) was employed. X-ray maps were obtained with a Rigaku 18 kW rotating anode source diffractometer operating at 50 kV and 100 mA, and using Cu  $K_{\alpha}$  radiation and a bent graphite monochromator with a resolution of  $\Delta q = 0.017 \text{ q}_0 \text{ \AA}^{-1}$ . The samples were placed in a four circle Huber goniometer ( $2\theta$ ,  $\theta$ ,  $\phi$  and  $\chi$ ). In these measurements  $\theta$  was kept constant at  $\theta = 0^{\circ}$  and  $\phi$  takes the place of  $\theta$  in both perpendicular and parallel scans. We used both a regular x-ray scattering geometry ( $\chi = 90^{\circ}$ ) and grazing incidence (GIXS) geometry ( $\chi = 0^{\circ}$ ).

The geometrical orientation of the oligos with respect to the surface of the GaAs was determined from  $2\theta$ - $\phi$  x-ray maps in both the out-of plane ( $\chi=90^{\circ}$ ) and in-plane (GIXS,  $\chi=0^{\circ}$ ) orientations (Figure 3.11). We have previously used a similar approach to investigate the orientation of 28-base thiolated ss-DNA on As-terminated GaAs and found that the oligos align preferentially at low angles with respect to the [100] direction of the (2x4) reconstructed surface of the As-terminated GaAs. The 8-base DNA behaves and can be treated as rigid extended chains, with two characteristic dimensions; a length of 4.62 nm and a diameter of 0.6-0.7 nm.

The circles in Figure 3.11 (a) show the in-plane (parallel to the surface of the substrate) scan obtained with GIXS when  $60 \mu\text{mol L}^{-1}$  DNA is deposited on the surface of the GaAs and dried. The squares correspond to X-ray scattering taken in the perpendicular direction when DNA is kept in buffer solution.

We have analyzed the intensity ( $I$ ) of the x-ray peaks in Figure 3.11 using Lorentzians of the form,

$$I(q) = \frac{A}{[1 + \xi^2(q - q_0)^2]} \quad (3.3)$$

where  $A$  is a constant,  $\xi$  is a measure of the size of the cluster,  $q$  is the wavevector, and  $q_0 = 4\pi/\lambda \sin\theta_0$  is the wavevector for which  $I$  is maximum. When the DNA oligos are normal to the surface,  $q_0$  is minimum and inversely proportional to the contour length. The fitted peaks are shown in Figure 3(b) for the perpendicular scans.

The peak of the Lorentzian for the dried DNA corresponds to  $3.97 \pm 0.05$  nm, which suggests that the oligos are at an angle of  $31 \pm 1^\circ$  from the substrate surface. This value agrees fairly well with the value of  $28.4^\circ$  obtained from the AFM images in Figure 3.7. This angle may be due to the way the DNA attaches to the surface as seen in Figure 3.4. The value of  $\xi$  for this sample is below the monochromator resolution, which suggests that the in-plane cluster size is larger than 9 nm for the dried DNA. This result is also in agreement with the AFM results which show a bundle width or  $\sim 14.6$  nm for the dried DNA sample.

Note that for the DNA in aqueous solution the peak of the Lorentzian corresponds to  $4.325 \pm 0.006$  nm, which suggests that the oligos are at an angle of  $20 \pm 1^\circ$  from the normal to the substrate or  $70 \pm 1^\circ$  from the substrate surface. Note also

that  $4.325 \pm 0.006$  nm is close to the calculated contour length of the DNA. For this sample,  $\xi_{\perp}$  is  $3.74 \pm 0.04$  nm. The smaller size,  $\xi_{\perp}$ , compared to  $4.325 \pm 0.006$  nm may be due to incomplete coverage of the DNA on the surface of GaAs. In general, short rod shaped polyelectrolyte molecules such as DNA oligos anchored from one end to a surface stand at right angle in the presence of a good solvent such as water. However, it is not surprising that the DNA oligos on GaAs are not oriented at  $90^{\circ}$  with respect to the GaAs surface because of the attachment of the N and O of the bases and sugar of the DNA with As in addition to the S at the end of the chains as we have previously reported for 28 base ss-DNA.

X-ray scattering was used to investigate the role of MCH in achieving the right-angled brush-like structure. The triangles in Figure 3.11 (a) correspond to X-ray scattering taken in the direction perpendicular to the GaAs substrate surface when  $60 \times 10^{-3}$  mol L<sup>-1</sup> of MCH was added after the attachment of  $60 \mu\text{mol L}^{-1}$  DNA and dried. We note that for the dried DNA with the MCH spacer, the peak of the Lorentzian fit (Figure 3.11(b)) corresponds to a distance of  $3.5 \pm 0.7$  nm, which suggests that the oligos are at an angle of  $41 \pm 1.6^{\circ}$  from the normal to the substrate or  $49 \pm 1.6^{\circ}$  from the substrate surface. For the DNA with the MCH spacer,  $\xi$  is  $5.2 \pm 1.0$  nm. These results indicate that with the addition of MCH the angle between the DNA oligos and the GaAs surface increased from  $31^{\circ}$  to  $49^{\circ}$  even in the absence of water.

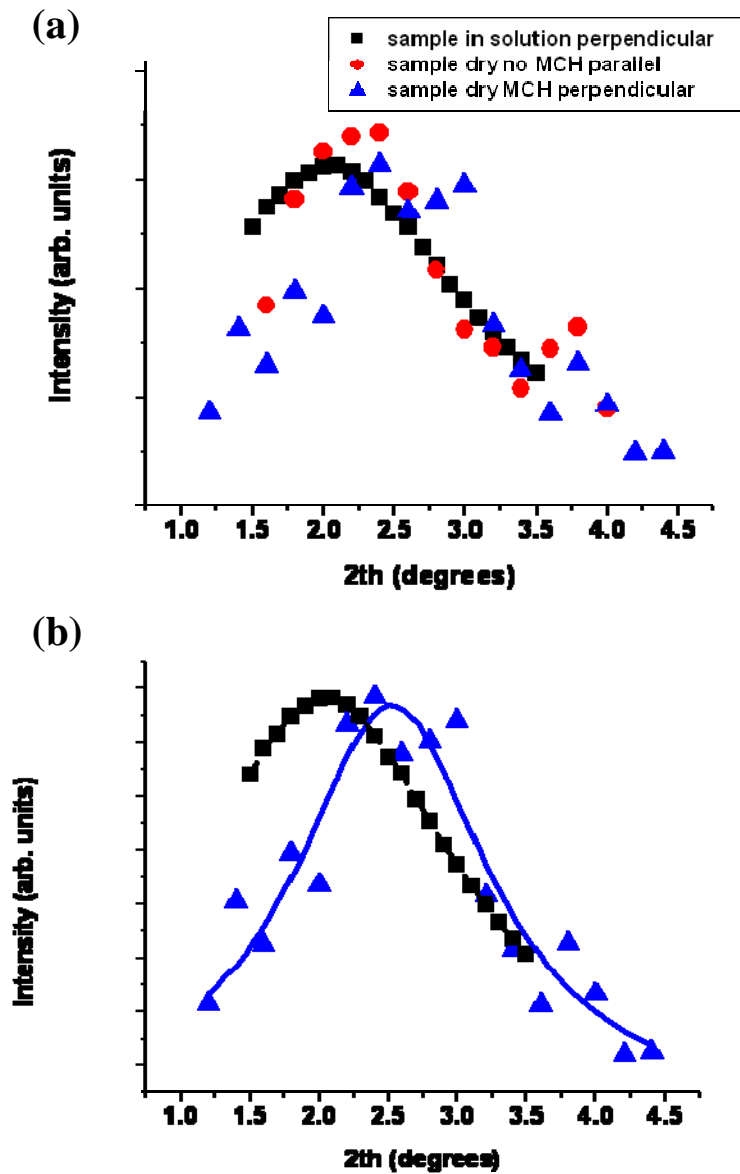


Figure 3.11 (a) X-ray scattering scans for DNA in solution (squares), DNA dry with the MCH spacer (triangles) and DNA dry without the MCH spacer (circles). The DNA in solution and the DNA dry with the MCH spacer were taken using X-ray scattering (perpendicular) whereas the DNA dry without the MCH spacer was taken using GIXS (parallel). (b) The X-ray scans for the DNA dry with MCH and the DNA in solution showing the fits to Lorentzian curves.

O (1s) and N (1s) XPS spectra from a sample with  $60 \mu\text{mol L}^{-1}$  attached to As-terminated GaAs are shown in Figure 3.12 (a) and (c), respectively. The broad O (1s) peak in Figure 3.12 (a) can be resolved into two separate peaks; one at a lower binding energy (peak (b)) of 531.0 eV corresponding to the oxygen in the DNA backbone, i.e. bases, sugar and phosphate moieties, and one at a higher binding energy (peak (a)) of 532.6 eV corresponding to O-As bonds. Similar behavior is observed in the case of N (1s) (see Figure 3.12 (c)), which can also share its electron with arsenic. The two nitrogen peaks at  $400.5 \pm 0.2$  eV and  $399.1 \pm 0.3$  eV, corresponding to two types of nitrogen bonds. The higher binding energy peak at 400.5 eV, peak (a), corresponds to the undesired N-As bond and the peak at 399.1 eV, peak (b) corresponds to nitrogen in the bases of the DNA. It is very well known that short electrolytes have rod shape structure and are expected to form a brush-like morphology perpendicular to the surface when they are anchored at one end. However, these results demonstrate that the N-As and O-As bonds force these rods to bend preventing them from standing at right angle.

In an attempt to achieve the right-angled brush like structure we introduced MCH into the system after the attachment of the DNA as shown in Figure 3.12 (b) and (d). Since the MCH molecules are smaller than the 8 base DNA and, more importantly, they do not have N and only have one O per molecule it is expected that the steric effect will be decreased. XPS data from samples with  $60 \mu\text{mol L}^{-1}$  and different [MCH] showed further reduction in the fraction of N-As and O-As bonds and an increase in the S-As bonds as expected. The O (1s) peak from the sample with

DNA and MCH spacer (Figure 3.12(b)) has two components, one at 531.2 eV corresponding to oxygen in the DNA backbone and the second at 532.5 eV corresponding to undesired oxygen bonding with As. It is also possible that the peak at 532.5 eV has a contribution from bonding between the hydroxyl group of mercaptohexanol with As. A comparison of Figure 3.12 (a) and (b) shows that with the addition of MCH the intensity of the peak at 531.0 eV (peak (b)) increases while the intensity of the peak at 532.6 eV (peak (a)) decreases. The ratio of the integrated intensity under peak (a) to that of peak (b) in Figure 3.12 (a) is 2.83. After the addition of MCH spacer (Figure 3.12(b)), this ratio decreases to 0.64. Similarly, for N (1s) the ratio of the integrated intensity under peak (a) to that of peak (b) in Figure 3.12 (c) is 1.1. After the addition of MCH spacer (Figure 3.12(d)), this ratio decreased to 0.87. These results indicate that the MCH spacer has displaced some of the As-O and As-N undesired bonding.

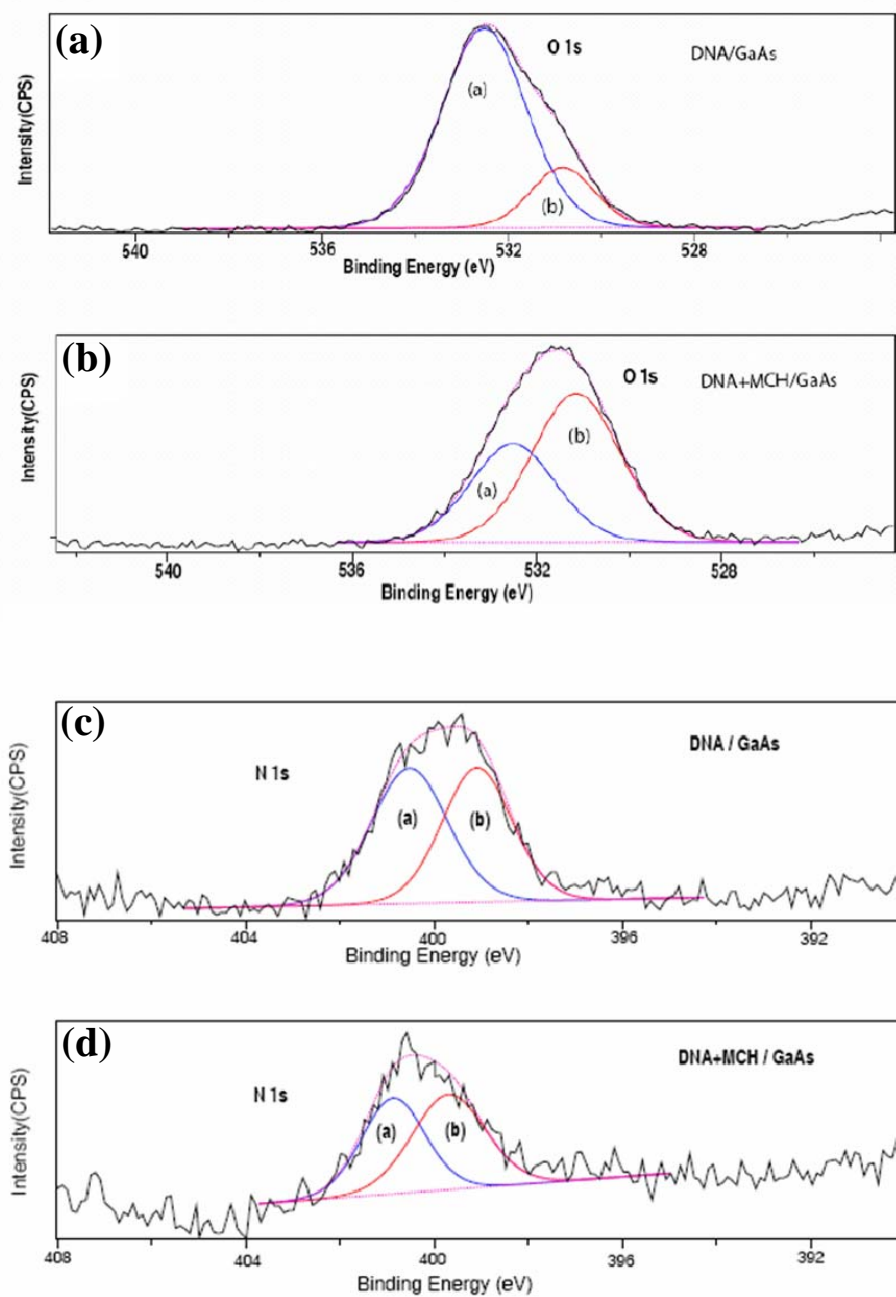


Figure 3.12 Comparison of Oxygen (1s) XPS peaks from the DNA/GaAs samples (a) without MCH and (b) with MCH spacer and for Nitrogen (1s) XPS peaks from the DNA/GaAs samples (c) without MCH and (d) with MCH spacer.

### **3.5 Effects of DNA and MCH Concentration on the Immobilization of a DNA layer on GaAs Surface**

I investigated quantitatively the role of the thiol group laced at the 5' end of the rods on the morphology of the brush like structure. This role stemmed from the fact that S-As bonds displace the O-As and N-As bonds. Figure 3.13 shows the effect of the concentration of the thiolated DNA on the S-, N-, and O- bonding with the As of the GaAs obtained from XPS. As expected the S-As bonding is preferable over the N-As and O-As bonding as the [ss-SH-DNA] increases. Initially, the ratio of S-As increases while the N-As, and O-As decrease and eventually all three curves reach a plateau at around  $60 \mu\text{mol L}^{-1}$ . This result suggests that displacement reactions have occurred by the thiol, removing some of the N and O from the As-terminated GaAs surface and producing S-As bonds instead. It is not surprising that the fractions of N-As and O-As bonds do not decrease further with increasing [ss-SH-DNA] because of the steric effect.

In an attempt to achieve the right-angled brush like structure we introduced MCH into the system after the attachment of the DNA as shown in Figure 3.14. Since the MCH molecules are smaller than the 8 base DNA and, more importantly, they do not have N and only have one O per molecule it is expected that the steric effect will be decreased. XPS data from samples with  $60 \mu\text{mol L}^{-1}$  and different [MCH] showed further reduction in the fraction of N-As and O-As bonds and an increase in the S-As bonds as expected. These results indicate that the MCH spacer has displaced some of the As-O and As-N undesired bonding.

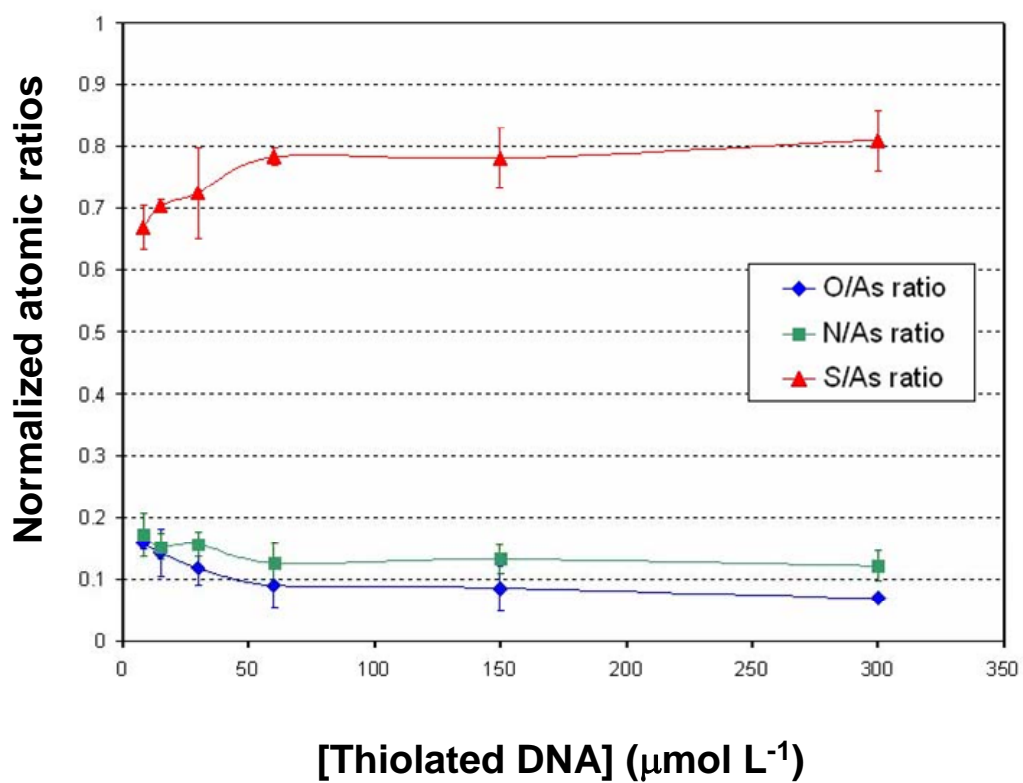


Figure 3.13 Normalized atomic ratios of S-As, O-As, and N-As from XPS spectra as a function of concentration of ssDNA

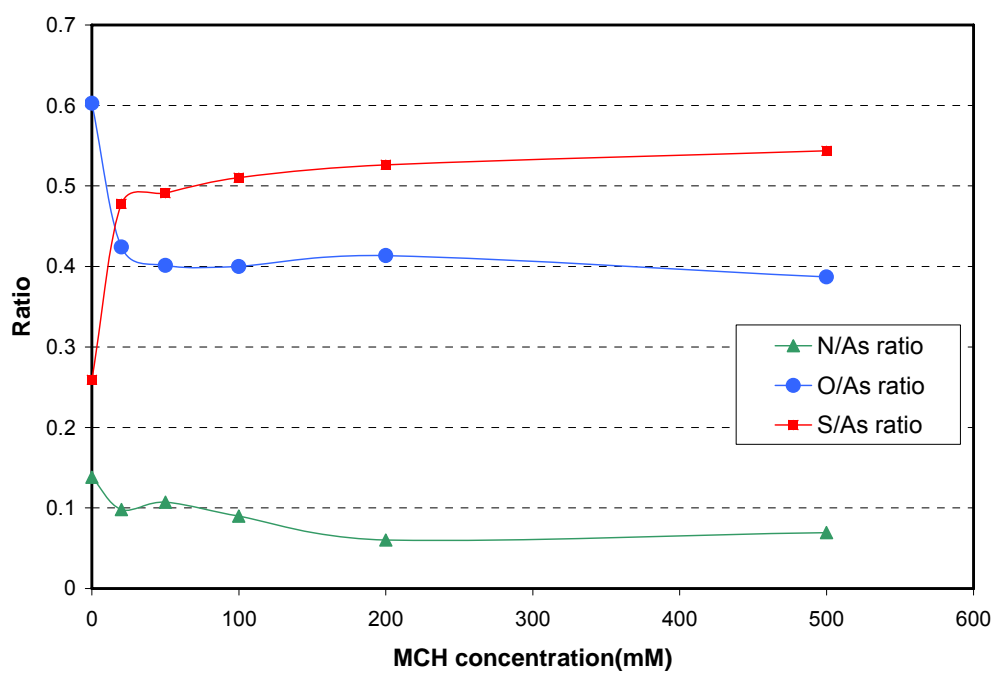


Figure 3.14 Normalized atomic ratios of S-As, O-As, and N-As from XPS spectra as a function of treated concentration of MCH on 60 $\mu$ M DNA samples.

### **3.6 Environmental Effects on the Immobilization of DNA layer on GaAs Surface**

DNA biosensors for the detection of target molecules usually operate in solution. Therefore, the properties of the dry-wet interface in the DNA / GaAs system are key issue in biosensor technology. To investigate the environmental effects on the morphology of the immobilized DNA layer, a fluid cell kit for the AFM was employed. The samples were imaged in solution in tapping mode using silicon nitride (resonance frequency: 8~15 kHz, spring constant: 0.06N/m; DNP-S, Veeco, USA) tips. Images were taken at rates of 0.5~1 kHz which the frequency was optimized for best image quality and the applied force was minimized as much as possible. Figure 3.15 shows a schematic of the experimental setup for the liquid cell AFM used to obtain images of ssDNA probes layer on GaAs in solution. Typical temperature was about 26°C during the scan.

Figure 3.16 shows the change of morphology of the DNA in the presence of aqueous buffer solution. Attempts to remove the DNA from a small region of the sample in aqueous solution using the AFM tip as done for the dried samples were not successful because of sticking of some DNA molecules on the AFM tip. Therefore, we expect the measured height of the DNA brush obtained from the samples in aqueous solution to be shorter than the real value. In any case there is a significant increase in the height ( $\sim 3.7 \pm 0.6$  nm) of the DNA layer compared to the dry samples. The average diameter of the bundles of DNA is reduced to  $6.6 \pm 2.5$  nm in the presence of water. Based on the contour length of 4.621 nm this result indicates that

the DNA oligos orient at an angle of  $>53.4^\circ$  with respect to the surface of the GaAs.

For  $60\ \mu\text{M}$  DNA treated with  $60\text{mM}$  MCH (Figure 3.17), the average height of DNA bundles is  $4.4 \pm 0.4\ \text{nm}$  which is slightly increased compared to the sample with DNA only. The size of the bundles was  $7.6 \pm 3.0\ \text{nm}$ .

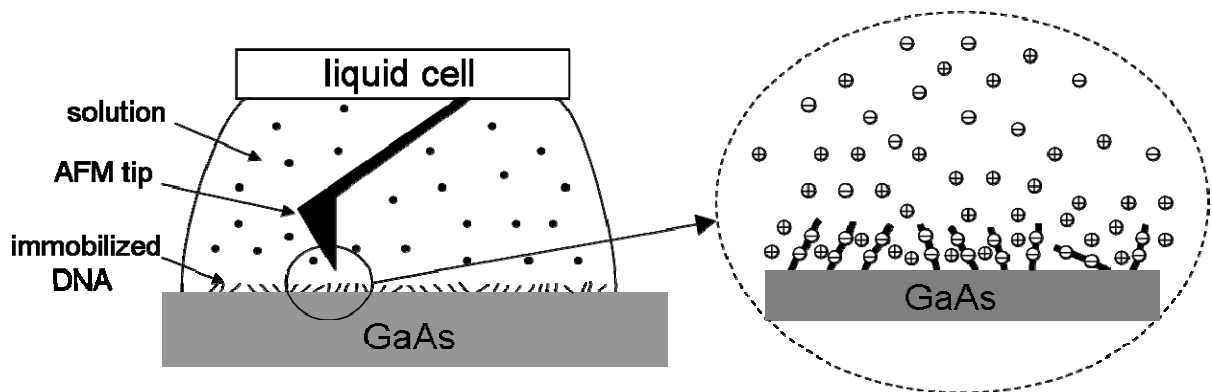


Figure 3.15 Schematic of the experimental setup for liquid cell AFM study of ssDNA probes layer on GaAs. In the zoom image on the right, the schematic represents counterions ( $\oplus$ ) that are localized within the DNA brush layer.

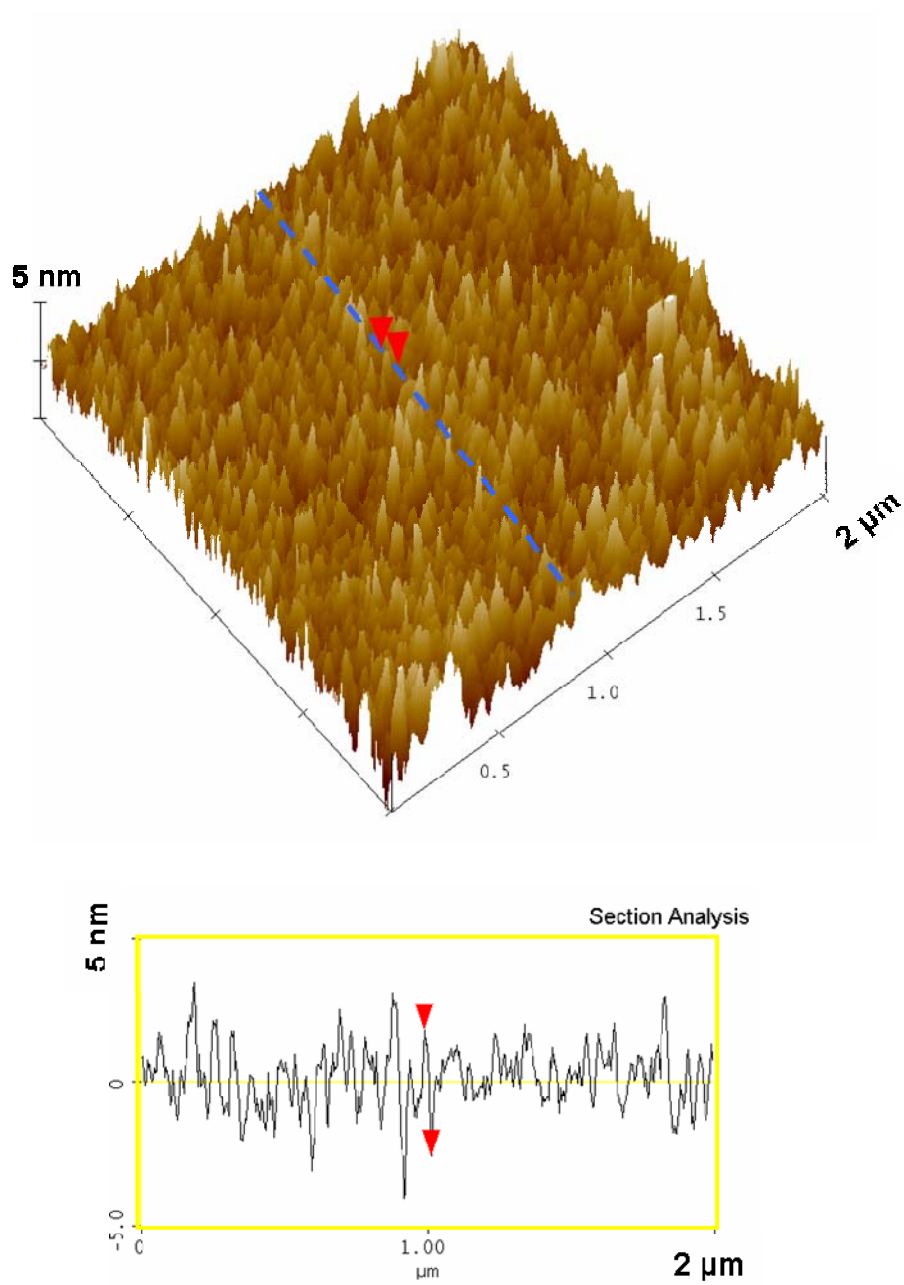


Figure 3.16 AFM image of  $60 \mu\text{mol L}^{-1}$  DNA on As-terminated GaAs (001) substrate in DI water.

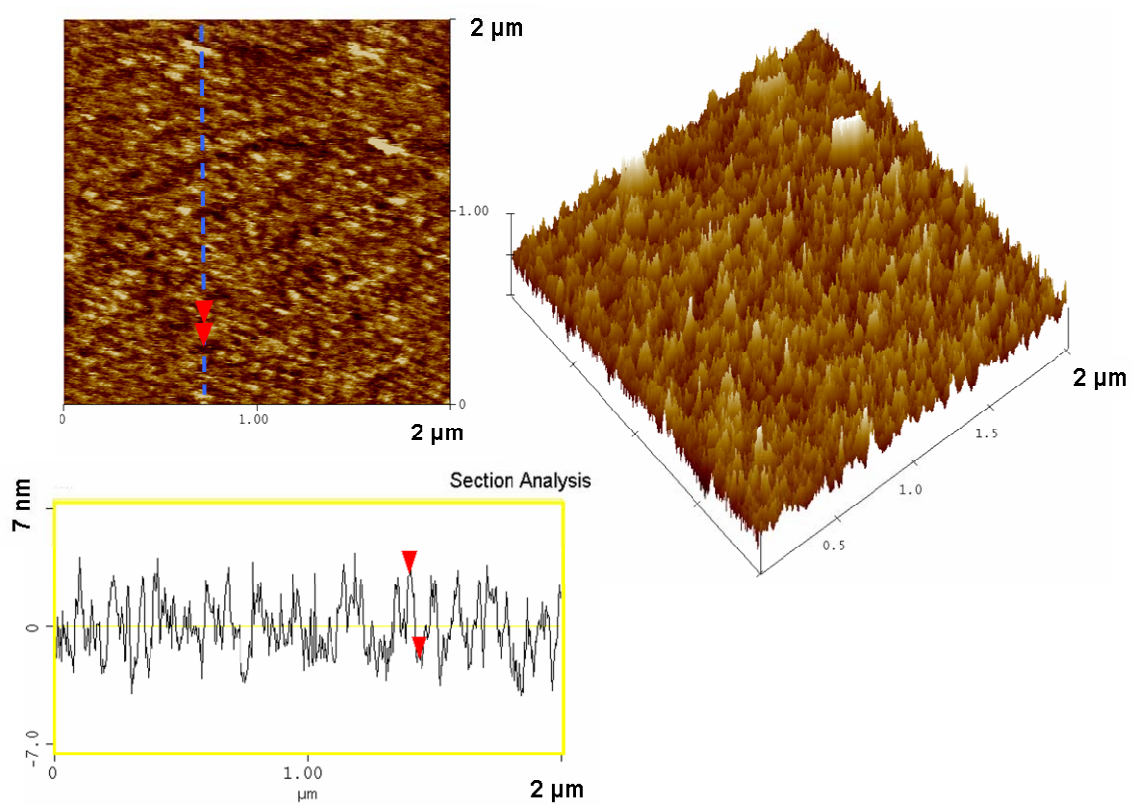


Figure 3.17 AFM image of  $60 \mu\text{mol L}^{-1}$  DNA and post treated mercaptohexanol (MCH) on As-terminated GaAs (001) substrate in DI water.

An important parameter to determine from the AFM images is the grafting density. However, this is difficult to obtain because the images of the DNA bundles represent the collapsed DNA oligos on each other in the absence of a good solvent as well as  $\pi$ - $\pi$  stacking. Furthermore, some collapse is also expected in the presence of water because of the osmotic pressure due to the counter ions.

Taking into account the distance of 0.7 nm between As-As dimmers, and the approximate diameter of the ss-DNA of 0.6-0.7 nm we expect that the closest separation between adjacent DNA oligos would be 0.7 nm corresponding to one DNA molecule per unit cell of GaAs. From our AFM images the diameter of the DNA bundle is in average 14.6 nm (dry) and 6.6 nm (in water). These values correspond to an average of  $\sim 527$  (dry) and  $\sim 107$  (in water) oligos/bundle. These reduce to  $\sim 421$  (dry) and 86 (in water) oligos/bundle taking into account the fact that from our XPS results 80% of the bonding to As is through S and 20% through N and O. Therefore, within a bundle the grafting density is  $\sim 2.5$  oligos/nm<sup>2</sup> both dry and in water. This value is the upper limit value of the grafting density within a bundle. Based on the AFM images, the bundle density is  $\sim 3,440/\mu\text{m}^2$  (dry) and  $8,480/\mu\text{m}^2$  (in water). The fraction of GaAs surface covered by DNA bundles is  $\sim 58\%$  (dry) and  $\sim 29\%$  (in water). The lower coverage in water indicates that some of the bundles become smaller than the lateral resolution of our AFM which is  $\sim 3$  nm.

### **3.7 Effect of Electrolyte on Immobilization of DNA layer on GaAs**

#### **Surface**

DNA is a polyelectrolyte because of the negative charges on the phosphate in the backbone of the DNA. When DNA is anchored on a substrate, there is electrostatic repulsion between neighboring DNA probes that can affect the hybridization reaction between probe and target molecules. In aqueous solution, the architecture of the DNA layer is determined by the chain elasticity and the osmotic pressure produced by the counterions. Therefore, the ionic strength in the solution is one of the major factors in determining the quality of DNA probes and the efficiency of any biosensor fabricated with them. In this section, the effect of electrolyte on the immobilized ssDNA layer on GaAs is investigated using AFM in solutions with different ionic strength.

Figure 3.18 (a) shows AFM images of immobilized ssDNA layer (60  $\mu\text{M}$  concentration) on GaAs using a fluid cell in a solution of DI water. The immobilized ssDNA chains are stretched along the normal orientation to the substrate surface in DI water. In this case an electrostatic repulsion exists between the DNA molecules with negative charge in the phosphate backbone. The addition of NaCl into the solution increased the osmotic pressure in the system preventing the swelling of the grafted polyelectrolyte layer (see Figure 3.18 (b)).

The effects of ionic strength should be investigated more systematically to gain better understanding of the behavior of the immobilized ssDNA layer in a buffer composition. These results will shed light into biological requirements for the application of these materials as biosensors. For this purpose, the sample was scanned in solution after adding different concentrations of monovalent salts, such as NaCl. Figure 3.18 (b) shows the same sample of Figure 3.18 (a) scanned after adding in 1M NaCl solution. The average height of ssDNA layer slightly decreased from  $3.7 \pm 0.6$  nm for the case of pure DI water to  $3.5 \pm 0.5$  nm for the solution with NaCl. The average diameter of the bundles of ssDNA increases from  $6.6 \pm 2.5$  nm to  $9.8 \pm 1.1$  nm after the addition of NaCl. These dimension changes indicate that increased concentration of  $\text{Na}^+$  shield negatively charge of the phosphate backbone of ssDNA causing of the repulsive forces between DNA molecules. As a result, the bundle size increases. For the height difference, Pincus (1991) predicted that a polyelectrolyte brush height shrinks with increasing salt concentration as a relatively weak power law in  $C_s^{-1/3}$  ( $C_s$ : salt concentration) . Considering that the 8-base ssDNA molecule is a rigid rod, the shrinkage of the brush height is very small. The dimension of the brush is determined by a balance between the counterion entropy and the chain elasticity. Pincus also predicted that higher grafting densities of polyelectrolytes are less sensitive to added electrolytes. We investigated the behavior of higher coverage of ssDNA on the surface in a solution containing salt. For this study, 200 $\mu\text{M}$  concentration of ssDNA was used. Figure 3.19 (b) shows the surface morphology after immobilization of 200 $\mu\text{M}$  ssDNA by AFM in dry mode. The average brush height and width of the bundles are  $3.4 \pm 0.3$  nm and  $10.2 \pm 1.2$  nm. Comparing 60

$\mu\text{M}$  and  $200 \mu\text{M}$  cases, the brush height was slightly increased and the bundle size was decreased. This results is in agreement with Pincus prediction that high coverage of ssDNA on the surface helps to stretch the ssDNA polyelectrolyte to form a brush-like structure of ssDNA. After soaking in NaCl 0.1M solution for two hours and washing with DI water, the AFM image shows the ssDNA layer slightly collapsed in dry mode (Figure 3.19 (c)). The height in this case is reduced to  $2.7 \pm 0.7 \text{ nm}$ . The bundle size is increased to  $14.3 \pm 1.3 \text{ nm}$ . A summary of the statistical measurements of ssDNA probe dimensions is presented in Table 3.2.

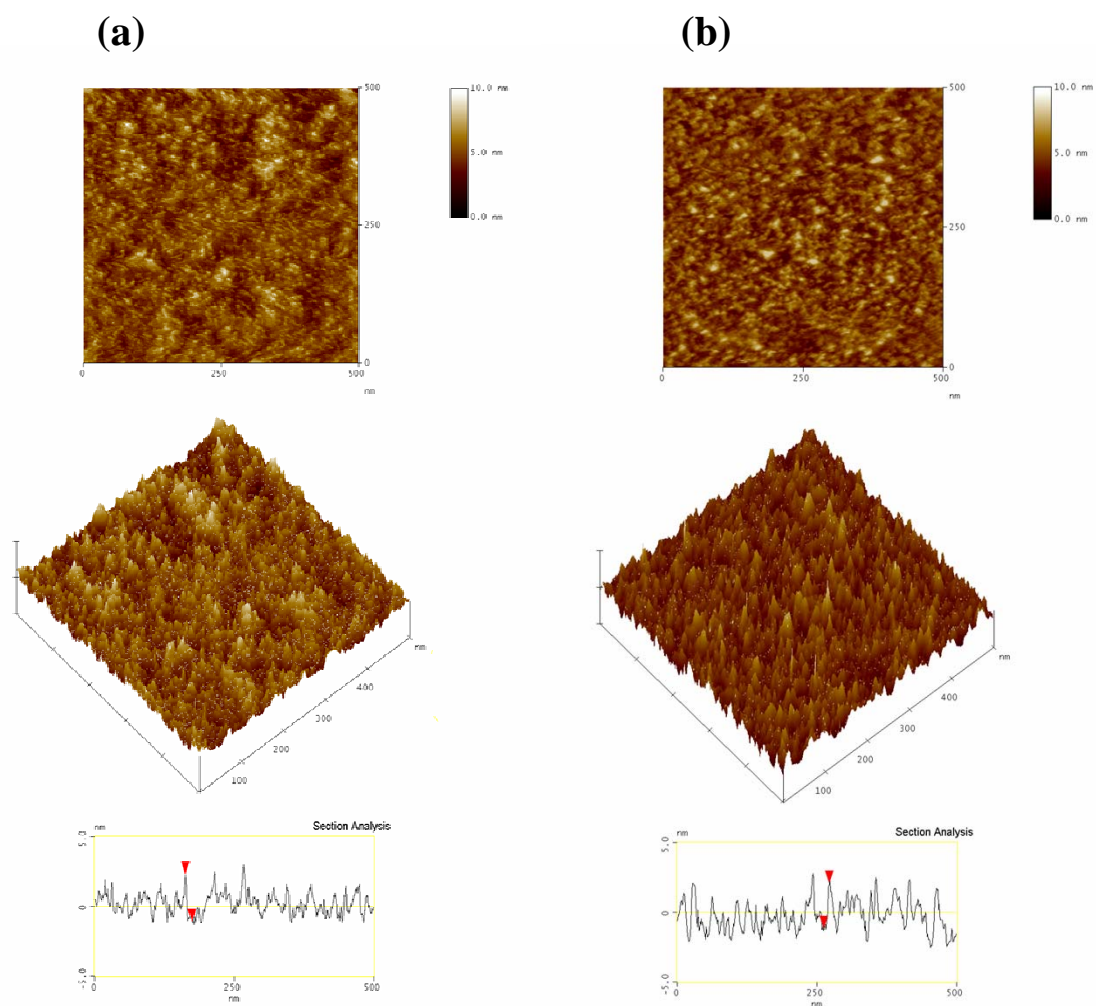


Figure 3.18 AFM tapping mode topography images in (a) DI water and (b) a solution with NaCl 1M after attachment of  $60\mu\text{M}$  DNA on GaAs substrate. The Scan area in the images is  $500 \times 500$  nm. The cross-sectional analysis of each image is also provided.

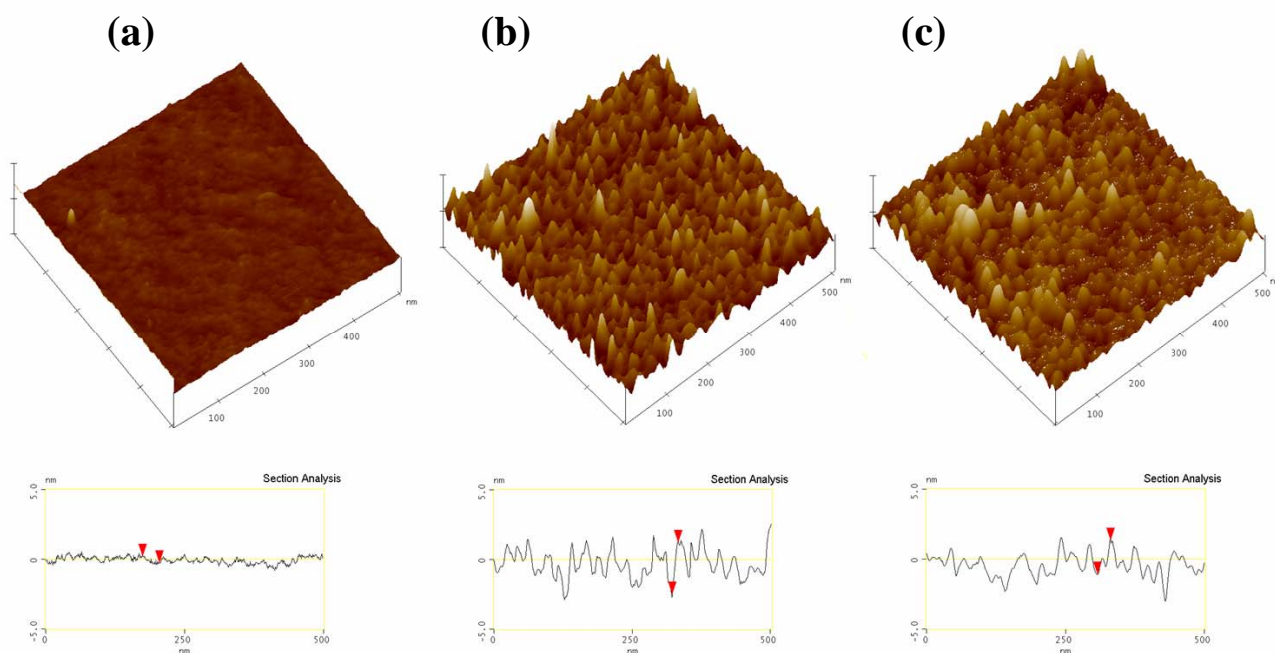


Figure 3.19 AFM tapping mode topography images in air of (a) bare GaAs surface, (b) before and (c) after soaking in NaCl 0.1 M solution for two hours after attachment of 200 $\mu$ M DNA. The samples were rinsed and sonicated in deionized water, and dried with Ar gas. The scan area in the images is 500 x 500 nm.

Table 3.2 Statistical measurements of ssDNA probe dimensions

	60 $\mu$ M sample (dry)	60 $\mu$ M sample (DI water)	60 $\mu$ M sample (NaCl 1M solution)	200 $\mu$ M sample (dry)	200 $\mu$ M sample (dry after NaCl 0.1 M solution)
av height (nm)	$2.2 \pm 0.4$	$3.7 \pm 0.6$	$3.5 \pm 0.5$	$3.4 \pm 0.3$	$2.7 \pm 0.7$
av width (nm)	$14.6 \pm 2.6$	$6.6 \pm 2.5$	$9.8 \pm 1.1$	$10.2 \pm 1.2$	$14.3 \pm 1.3$

### 3.8 Attachment of Longer Oligonucleotides on GaAs Surface

Longer DNA oligonucleotides have more genetic information than shorter strands. However, as the length increases, the molecules become more flexible and more polymeric like as far as their configurations. Flexible, coil-like polymer chains are expected for low surface coverage. Biosensor devices with low coverage of long chains are thus, expected to have low sensitivity. Steel et al. proposed that chains with 24 to 48 nucleotides are in a transition regime between rod like and flexible coil model [28]. In this chapter, I have investigated immobilization of 100-base thiolated ssDNA, flexible coil-like polymer for comparison with the more rigid 8-base ssDNA.

Figure 3.20 shows AFM images of an immobilized layer of 100-base ssDNA (60 $\mu$ M) on GaAs. These results reveal significant changes in surface morphology compared to the 8-base DNA presented in section 3.3.2. The lower magnification image (Figure 3.20 (a)) shows that the surface is covered by big clusters of circular shape. The diameter of the clusters is 330~440 nm, and their height is  $9.5 \pm 2.2$  nm. The density of the clusters is 3 ~ 4 bundles/ $\mu\text{m}^2$ . These aggregations could be explained by  $\pi$ - $\pi$  stacking between the bases of adjacent DNA molecules, and hydrophobic interactions of the bases. When the length of DNA is increased, these interactions become dominant in determining the morphology of the immobilization. Figure 3.20 (d) shows that there still exist some small bundles of DNA probes in the regions between the big clusters. The width of the small bundles is  $28 \pm 3.4$  nm, and the height was  $1.2 \pm 0.3$  nm.

When MCH is applied to this sample (see Figure 3.21), a displacement reaction of the N-As and O-As bond is expected. The dimensions of the big bundles are reduced with diameter of (290~340 nm) and height ( $6.6 \pm 1.7$  nm). In addition, for the small bundles are also changed. The width is reduced to  $24 \pm 2$  nm, and the height increased to  $2.8 \pm 0.7$  nm. These results indicate that MCH spacer is still affective in the immobilized 100-base DNA layer, even though a much larger number of non-desired bonds through the larger number of bases occurred between the DNA and the As atoms on the surface. This is because of an increase in entropic penalty to stretch the chains. FESEM results for both samples are shown in Figure 3.22. In both cases, big bundles cover the surface as in the AFM images. Also, the bundle size matched fairly well that obtained from the AFM results

To understand the behavior of the immobilized 100-base DNA layers in solution, the fluid cell of AFM was used in DI water and 1M NaCl solution. Figure 3.23 (a) is the surface morphology of 100-base DNA layer in DI water by AFM tapping mode. The diameter of the DNA bundles is reduced to  $17.5 \pm 2.9$  nm. The height of the DNA layer significantly increased to  $8.7 \pm 1.0$  nm compared to the dried sample. These results indicate that the chains stretch in the normal direction of the surface in the presence of water. The height is reduced to half ( $\sim 4 \pm 0.8$  nm) when the sample was immersed in the 1M NaCl solution, whereas the width increased about 2 times to  $32 \pm 4.3$  nm. This result is expected because of the osmotic pressure of the counterions in the layer is reduced by the added salt.

Figure 3. 24 shows X-ray scattering results for flexible 100 bases ssDNA (60  $\mu$ M) on GaAs. X-ray was performed from 0.1 degrees to 5 degrees in  $2\theta$ . The data shown were extracted from the rough data by comparing the high and low intensities produced by a wide angle mesh in  $\theta \sim 2\theta$ . There was not evidence for the radius of gyration determined by Tinland et al of  $R_g = 0.38N^{1/2}$  which is equal to  $3.8 \pm 0.1$  nm[111]. There are peaks that seem to correspond to harmonics of the 32 nm spacing observed in AFM. The harmonics correspond to  $23 \pm 1$  nm,  $12 \pm 0.5$  nm, and  $7 \pm 0.5$  nm. The structure corresponds to an arrangement of small crystallites, since the peaks can be fit with a Gaussian as illustrated in the lower figure.

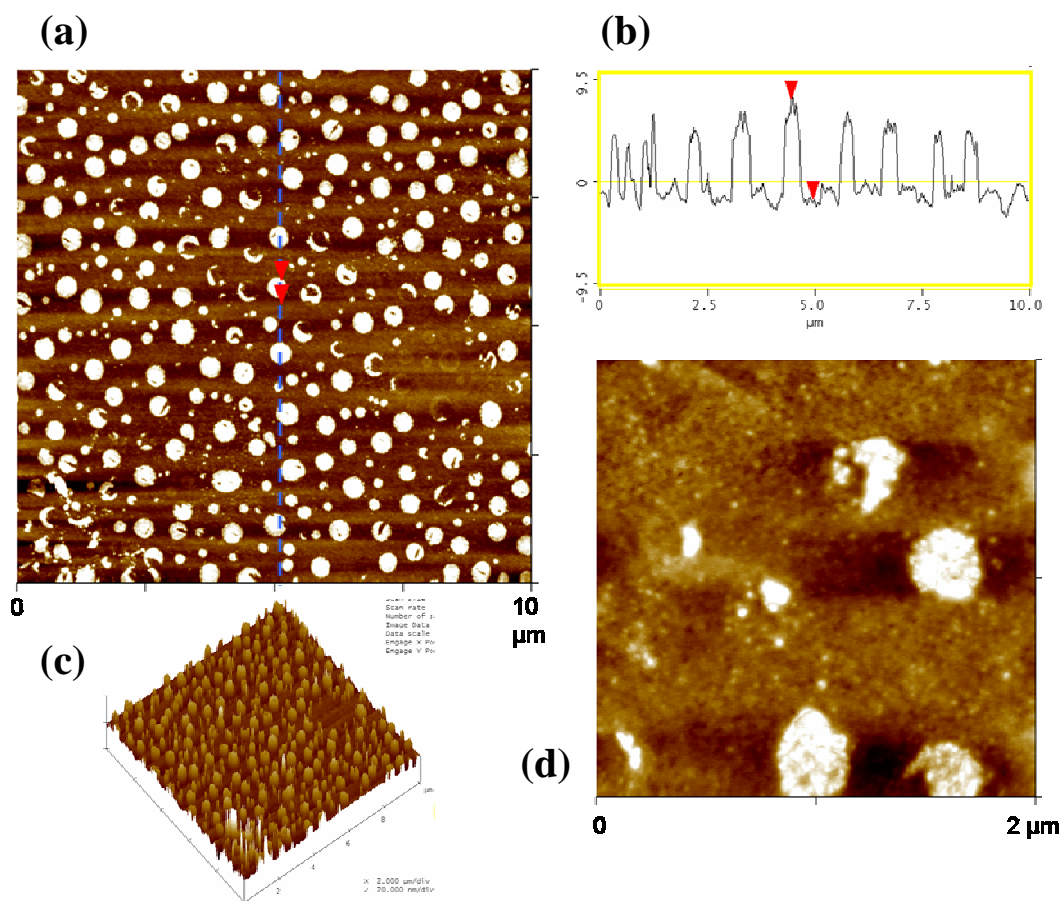


Figure 3.20 AFM image in dry of  $60 \mu\text{mol L}^{-1}$  100-base DNA on As-terminated GaAs (001) substrate. Plane view ( $10 \times 10 \mu\text{m}$ ) (a), line profile (b), three dimensional view (c), and plane view ( $2 \times 2 \mu\text{m}$ ) (d).

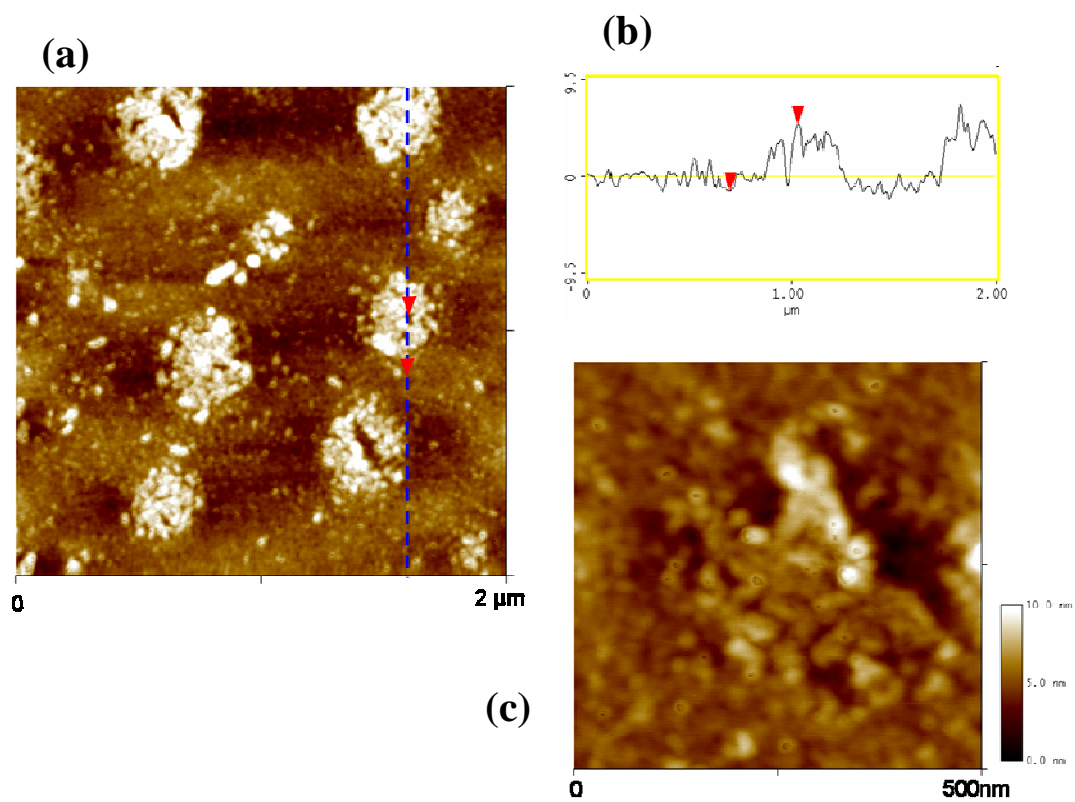


Figure 3.21 AFM image in dry of  $60 \mu\text{mol L}^{-1}$  100-base DNA and after treatment with MCH on As-terminated GaAs (001) substrate. Plane view ( $2 \times 2 \mu\text{m}$ ) (a), line profile (b), and plane view ( $500 \times 500 \text{ nm}$ ) (c).

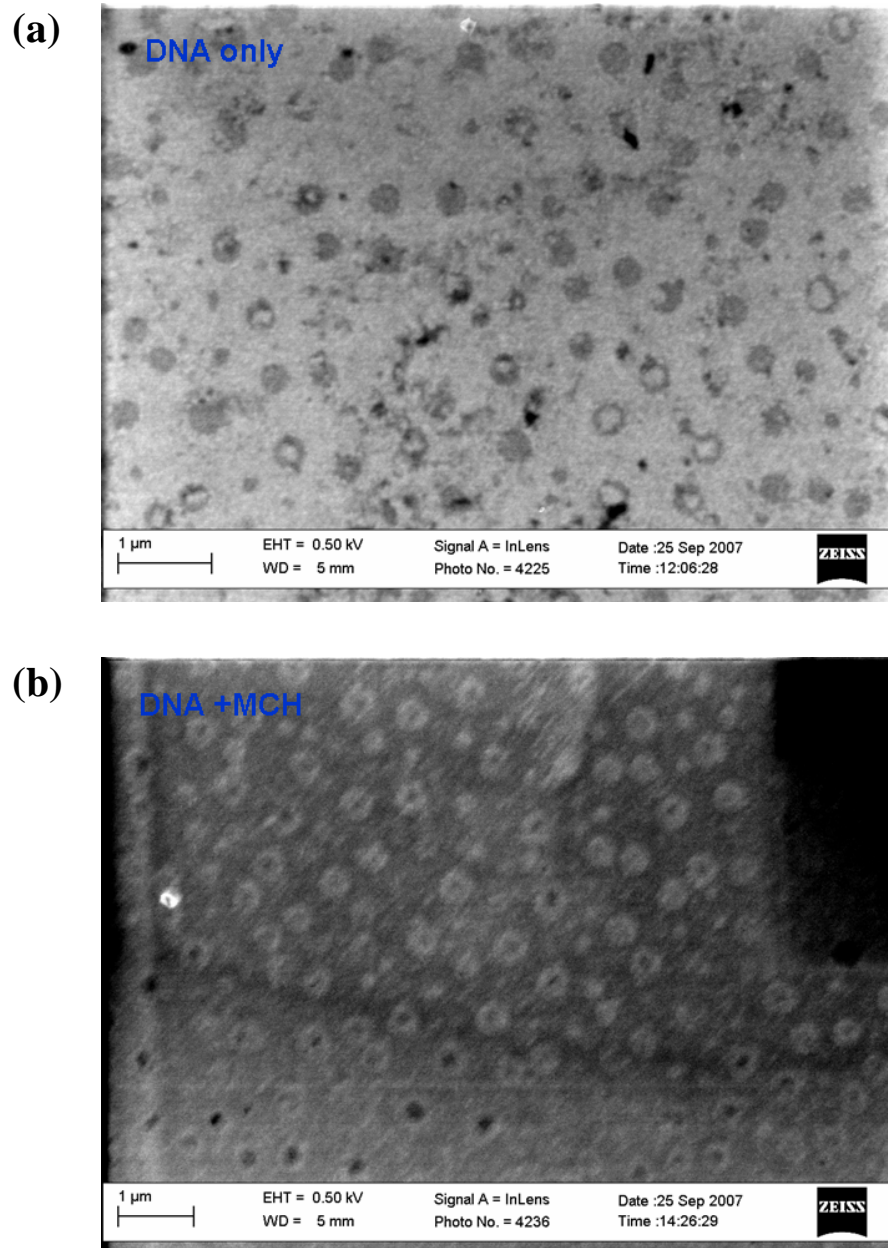


Figure 3.22 Surface morphology of FESEM images (a) thiolated 100-base ssDNA layer (b), and after treatment with MCH of (b) sample.

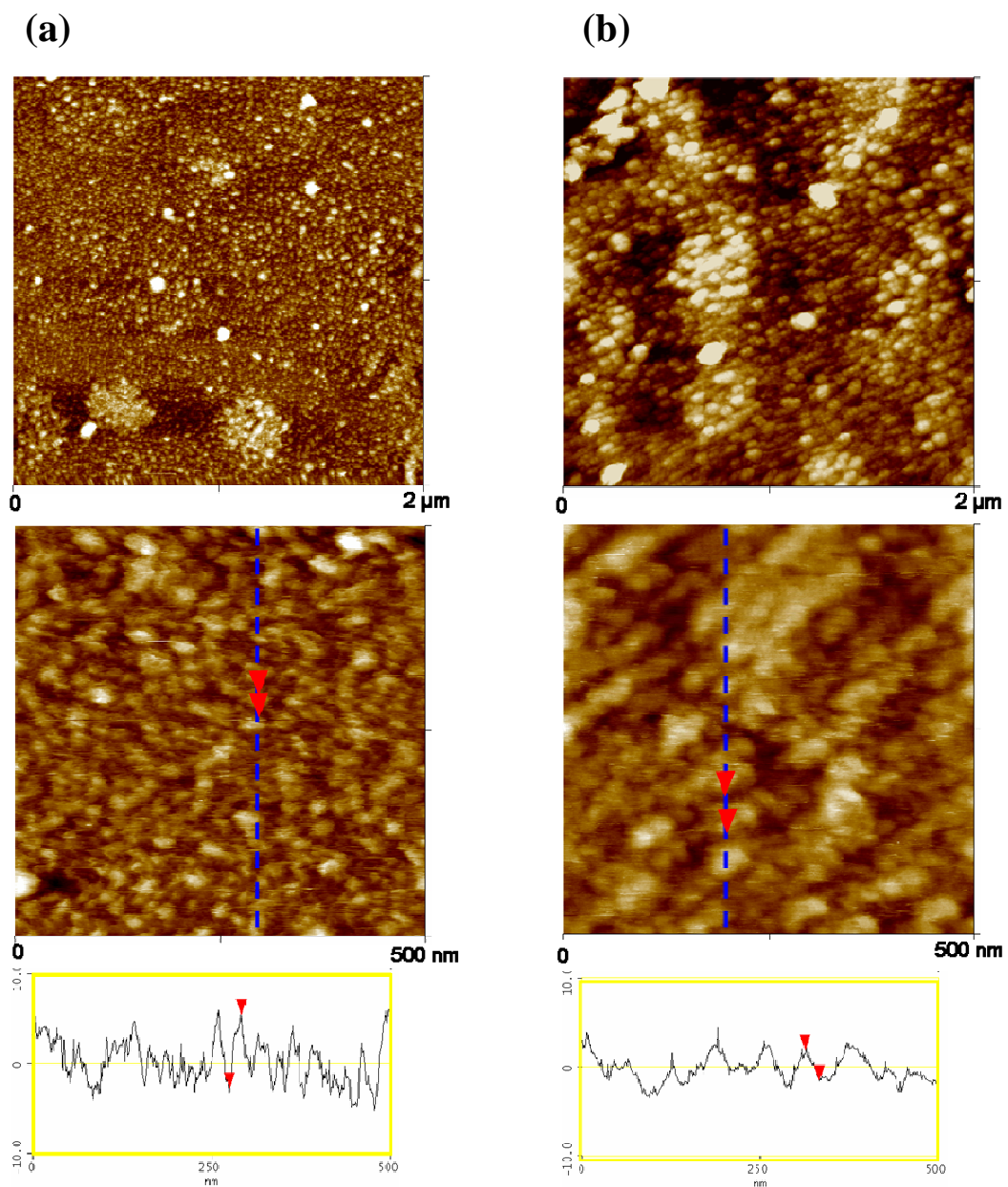


Figure 3.23 AFM image of  $60 \mu\text{mol L}^{-1}$  100-base DNA on As-terminated GaAs (001) substrate in DI water (a) , and in 1M NaCl solution (b): Plane view ( $2 \times 2 \mu\text{m}$ ), ( $500 \times 500 \text{ nm}$ ) and line profile for each image are shown in the middle and bottom of the figure, respectively.

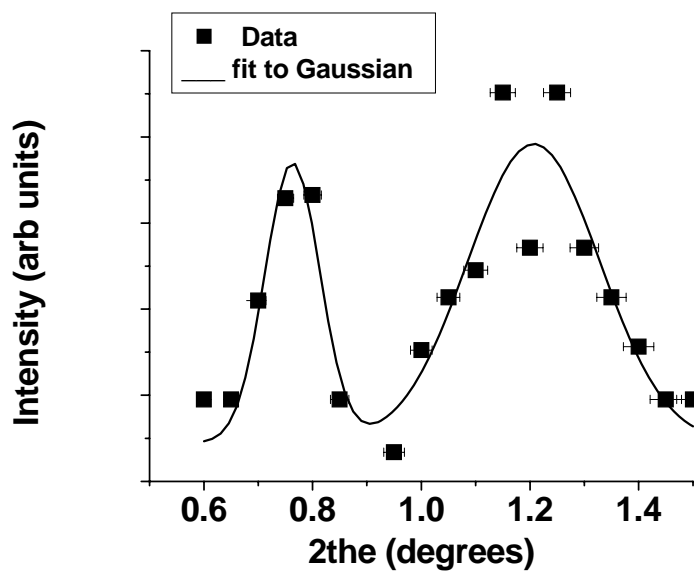
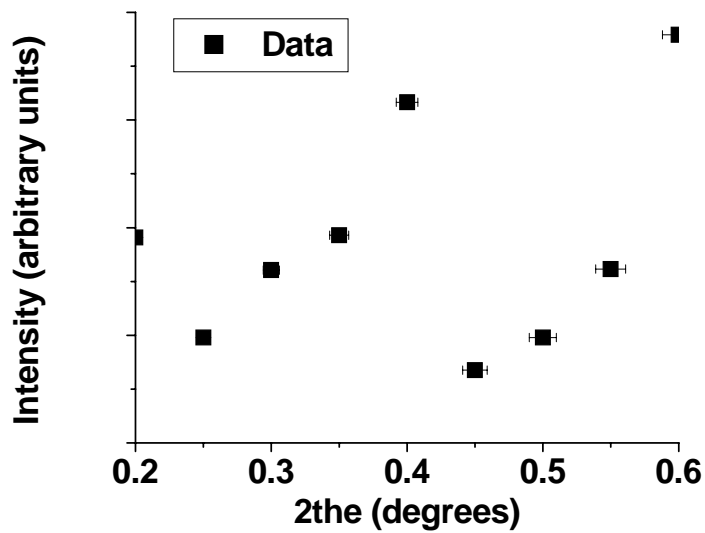


Figure 3.24 X-ray scattering scans for 100 bases ssDNA (60 $\mu$ M) on GaAs.

## **Chapter 4.**

### **4. Toward the Development of DNA Biosensors**

#### **4.1 Introduction**

A biosensor is a device that couples electronic machinery to biological molecules. There are three major types of biosensors : bimolecular sensor, a solid phase platform, and electronic transducer. The transducer detects and measures a physio-chemical change produced by interactions between the biological sensor and the target molecules. The bimolecular sensor can be based on by enzymes, antibodies, or ssDNA depending on the desired type of interaction (DNA-DNA, DNA-protein, or protein-protein). For the electronic transducer, there are three different types of strategies which are currently utilized electrochemical, optical and piezoelectric technique. In the electrochemical method, DNA based biosensors normally involve immobilized single-stranded DNA at an electrode surface. The hybridization can be detected by monitoring changes in the redox properties of an electroactive indicator. Other development of DNA biosensors are optical transduction techniques including fluorescence spectroscopy, fiber optics and surface Plasmon resonance (SPR). The third type of biosensor utilizes piezoelectric or acoustic wave sensor which is a device sensitive to mass variation during hybridization. This method has the advantage of being a direct detection method and does not require labelling.

A biosensor should have high sensitivity, reliability, short response time, low cost, and miniaturization as well as direct detection method (label-free) to avoid any undesired reaction of the sample with the attached labels.

DNA can be damaged by ionizing radiation and this led to an interest in aerospace field and the radiation industry. In space, the background level of radiation is many times higher than on Earth which is protected by the atmosphere. DNA biosensors are excellent tools for detection of DNA damage by ionizing radiation. In this chapter, I present preliminary results of the damage of ionizing radiation to DNA probes and detection of hybridization reaction between the probes and targets using AlGaAs resonator.

## **4.2 Effects of Irradiation on an Immobilized DNA layer on GaAs**

The DNA biosensor composed of a thiolated ssDNA layer on GaAs surface has great potential for monitoring radiation. Several degrees of damage to the DNA layer should be considered when a DNA biosensor is exposed to high levels of ionizing radiation. First, radiation can damage DNA by production random scissions on the back bone of the DNA. Second, rupture can occur in the anchoring bond between the DNA and the As atom on the surface (N-As, O-As, and S-As). This can make DNA molecules leave the surface. Finally, radiation can cause cross-linking between adjacent thymine or cytosine bases, creating a so-called pyrimidine dimer.

Thymidine dimer is shown in Figure 4.1[112, 113]. This dimerization prevents hybridization.

M. Al-Sheikhly et. al investigated the damage induced by ionizing irradiation to the DNA probes on GaAs using by XPS [67]. They observed a decrease in atomic concentration of thiol after irradiation, which means that cleavage and rupture of the anchoring group had taken place upon irradiation. In this section, the observation of surface morphology changes of the DNA layer immobilized on GaAs after irradiation was carried out using AFM technique

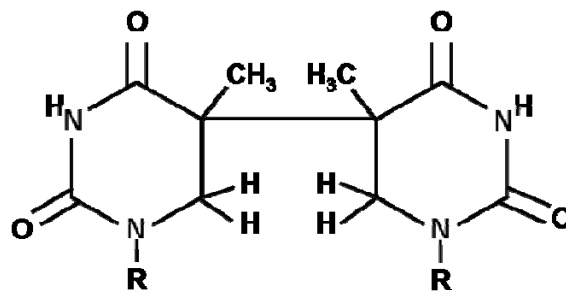


Figure 4.1 Formula of the C(5)-C(5) linked dihydrodimer of thymidine

The AFM images in Figure 4.2 show the dramatic change of surface morphology after 47 MGy electron beam radiation of 8-base ssDNA probes (60  $\mu$ M) on GaAs. Figure 4.2 (a) shows the scan image in dry mode. Comparing with Figure 3.6, before irradiation, the surface roughness decreased and needle-like circular shape of the DNA bundles is not observed any more. The height of the DNA layer before and after irradiation changed from  $2.2 \pm 0.4$  nm to  $0.8 \pm 0.3$  nm. The whole surface became fairly smooth and flat. This result indicates that the ssDNA layer collapsed completely by irradiation. The bundle size of the DNA probes increased almost 2 times from  $14.6 \pm 2.6$  nm to  $29.8 \pm 4.8$  nm. This increasing bundle size can be explained the by collapse of DNA probes as well as the dimerization of thymine-thymine dimers through the formation of covalent bond between two thymine bases in adjacent DNA molecules. Figure 4.2 (b) is an AFM image in DI water from the same sample as Figure 4.2(a). The bundle size remains almost same as in dry mode size ( $27.3 \pm 5.8$  nm). However, the height of the DNA layer increased to  $2.92 \pm 1.1$  nm. In addition, some areas of the sample did not show any bundle shape of DNA. This is probably because some DNA probes were removed from the surface of the substrate in DI water after the rupturing of the anchoring group (mainly S-As covalent bond) by the irradiation. M Al-Shekhily et al. noted that the dose on the DNA dose is 50 % greater than the dose received by the GaAs the backscattering phenomenon from the GaAs. They also observed 40 % reduction of atomic concentration of bounded sulfur at thiol after irradiation[67].

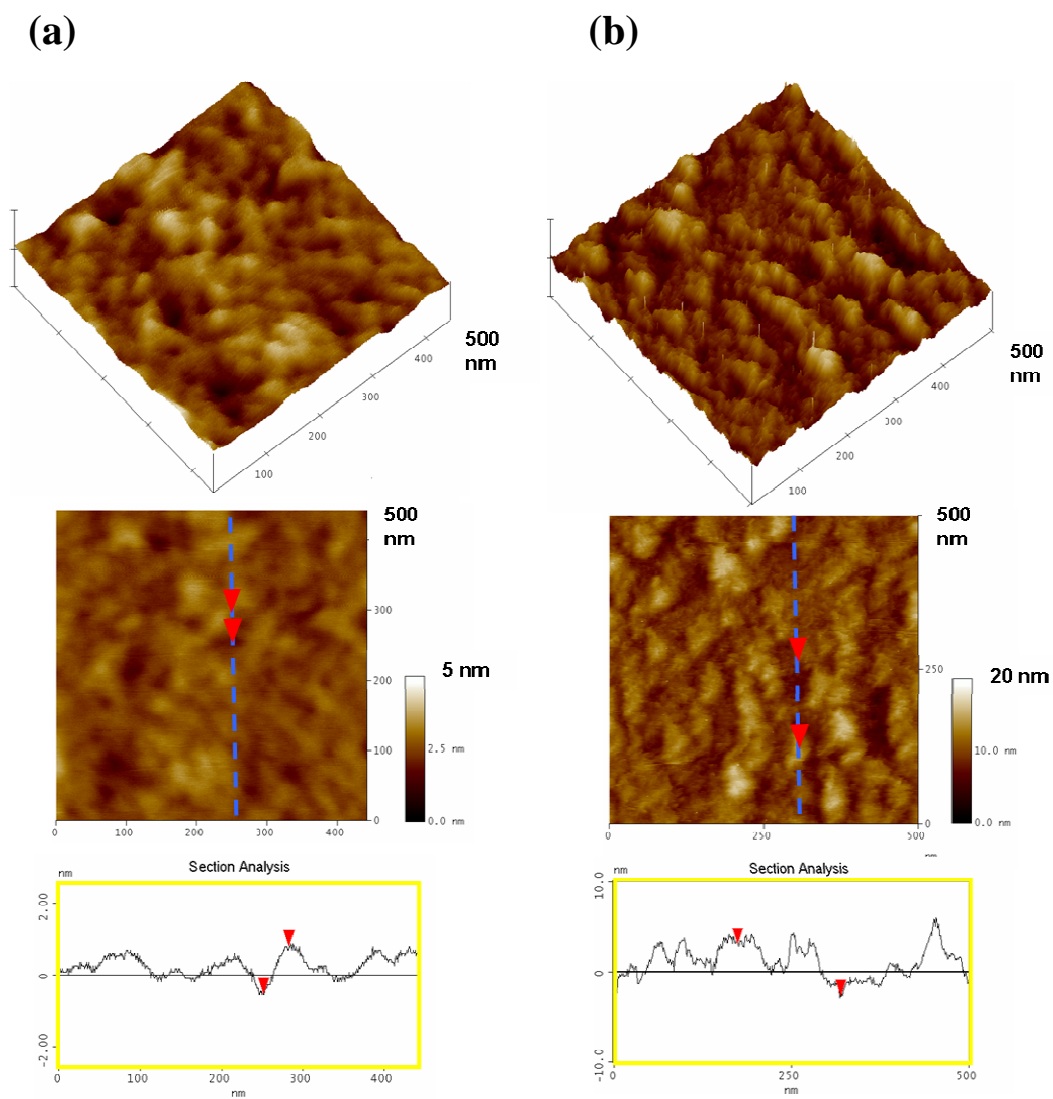


Figure 4.2 Three-dimensional and plane view AFM images and linear profile of immobilized ssDNA layer on GaAs after irradiation by e-beam with 47MGy dose level. (a) scanned in air and (b) scanned in DI water. Dimensions are 500 X 500 nm, z scale is 5 nm.

## 4.3 AlGaAs Resonator Biosensor

### 4.3.1 Introduction

More recently, resonant mass sensors have been created on a single chip by microfabrication technology. The chip works in resonant mode which could detect resonant frequency shift by interaction between target and probe molecules that are functionalized on the sensor surface. The mass change is calculated by resonance frequency shift using Sauerbrey Equation.

$$\Delta f = \frac{-2 \Delta m f_0^2}{A \sqrt{\rho_q \mu_q}} \quad (4.1)$$

Where  $f_0$  is resonant frequency of the material,

$A$  : active area

$\rho_q$  : density of material

$\mu_q$  : shear modulus of material

$\Delta f$  : change frequency

$\Delta m$  : change mass

Ilic et al. demonstrated resonant mass sensors using 150 nm polysilicon cantilever[114]. However, low quality factors of silicon based resonators at atmospheric pressures require vacuum operating system to obtain acceptable mass resolution. The active piezoelectric materials for resonant mass sensor have been

studied to overcome the limitation of silicon resonator system. Several resonant mass sensors based on piezoelectric materials have recently been demonstrated [115, 116]. Although piezoelectric materials have low values of motion resistance with small bias voltage, higher internal loss and big damping effect caused metal electrodes can reduce the overall Q of a resonator.

Don DeVoe et al. have recently demonstrated a fabrication process for resonators based on multilayer of single crystal piezoelectric  $\text{Al}_{0.3}\text{Ga}_{0.7}\text{As}$  and Si-doped  $\text{Al}_{0.3}\text{Ga}_{0.7}\text{As}$  electrodes. Figure 4.3 shows a cross-sectional of a typical device. These  $\text{Al}_{0.3}\text{Ga}_{0.7}\text{As}$  resonators showed Q value as high as 25,390 in vacuum, and 11,200 in air [117]. These high Q values can make the establishment system without a vacuum environment.

#### **4.3.2 Detection of Hybridization Using AlGaAs Resonator**

The disk type AlGaAs microresonator was fabricated by Don DeVoe group members for detecting the change in frequency of a resonator upon hybridization of 8-base ssDNA probes with its complementary target ssDNA. Thiolated 8-base ssDNA (60  $\mu\text{M}$ ) probes immobilized by same method described in Chapter 2. After immobilization of probes, the resonator was washed with DI water and measured its resonance frequency in air.

Then the resonator immersed to complementary DNA solution (60 $\mu$ M) at room temperature for 24 hours for hybridization. After 24 hours, the resonator was washed with DI water and measured its resonance frequency again in air. Figure 4.4 shows the dried surface morphology of a DNA layer on AlGaAs before (a) ssDNA and after (b) dsDNA hybridization with complementary DNA obtained using AFM. AFM data revealed that the bundle size increased from  $\sim$ 10-30 nm to  $\sim$ 40-60 nm after hybridization. This increase in size is expected from the bigger diameter of dsDNA. The relatively uniform increase in size shows that hybridization successfully occurred over the whole area. As shown in Figure 4.5, the completion of the hybridization reaction produced a change in resonance frequency  $\Delta f$  of 16.773 kHz. Using Sauerbrey's equation and taking into account the density of AlGaAs of 4.852 g/cm<sup>3</sup>, the shear modulus of AlGaAs of  $3.223 \times 10^{11}$  dyn/cm<sup>2</sup>, and assuming that hybridization occurs on the top and bottom sides of the 60  $\mu$ m diameter resonator, I obtained a change in mass of  $\sim$ 25pg. These results indicate that 10fmol of the 8 bses ssDNA underwent hybridization. This shows that the resonator method is capable of detecting very low changes in mass due to chemical interactions.

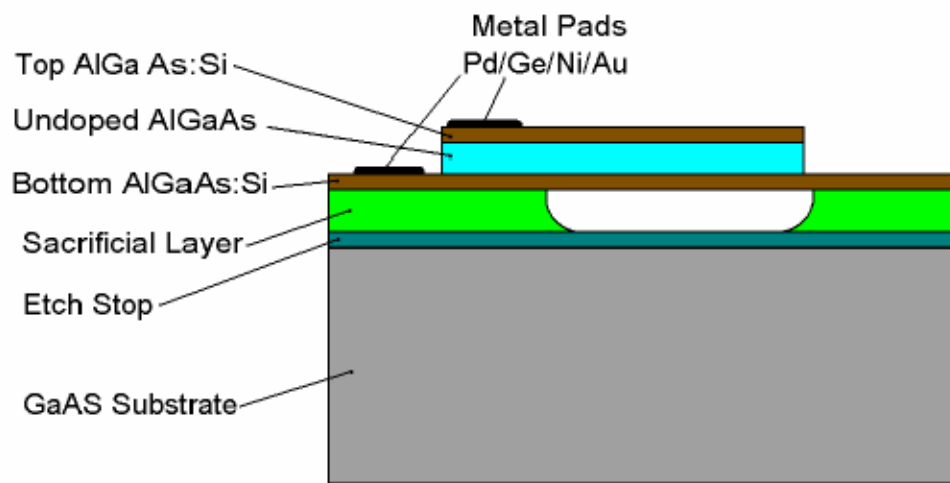


Figure 4.3 Cross-sectional schematic of an AlGaAs microresonator

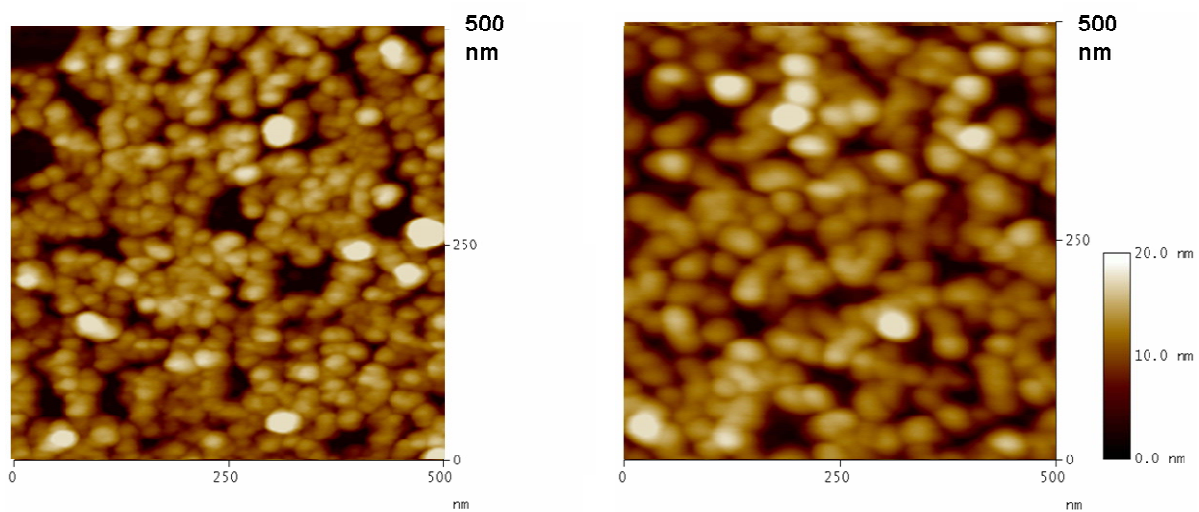


Figure 4.4 AFM plane view images of immobilized ssDNA layer on  $\text{Al}_{0.3}\text{Ga}_{0.7}\text{As}$  surface (a) before hybridization and (b) after hybridization with complementary DNA (cDNA). Dimensions are 500 X 500 nm, z scale is 20 nm.

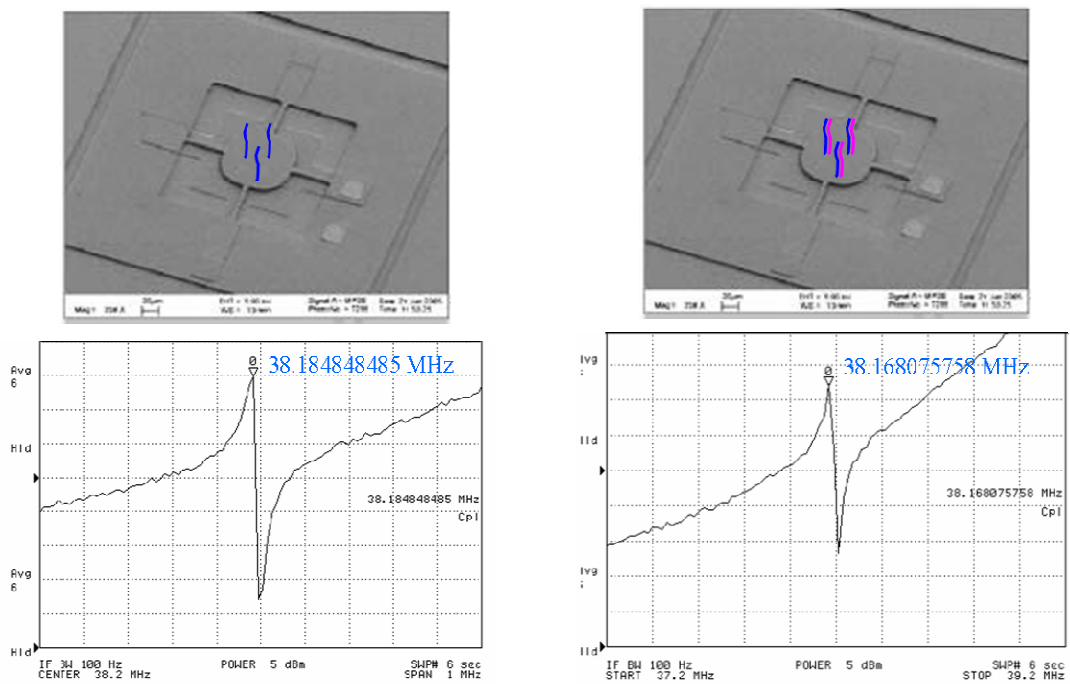


Figure 4.5 SEM images and frequency shift ( $\Delta f = 16.773$  kHz) before (a) and after (b) hybridization with complementary DNA on a disk type AlGaAs resonator. The SEM images have schematics of the ssDNA (a) and hybridized DNA (b) on the resonator.

## Chapter 5

### 5. Discussion and summary

In this work, thiolated ssDNA probes were immobilized on GaAs-base semiconductors via covalent bonding between the thiol group, the N or O in the bases and the As of the GaAs substrate. A series of characterization techniques have been carried out to understand the structure and behavior of the immobilized DNA layer on GaAs (001) surfaces as well as to investigate the surface chemical bonds between the DNA molecules and the As atoms of the GaAs surface. In a different set of experiments, the effect of irradiation and the detection of DNA hybridization using AlGaAs resonator we are also performed.

The effects of modification of unmodified and modified 8-base DNA molecules have been characterized using AFM and FESEM after immobilization of the DNA probes using the same procedure. The results indicate that non-modified DNA molecules prefer to lay down along the As-rich dimer row direction [110] because the nitrogen and oxygen atoms in the bases of ssDNA with As atoms on the surface. In addition, the AFM line profile shows that some interactions ( $\pi$ - $\pi$  stacking), caused aggregation of DNA molecules, in spite of the negative charge on the backbone of the DNA. The tethering density in this system was high enough to give rise to overlap between molecules' chains as predicted by the scaling theory. In the regime with low tethering density, called mushroom regime, the equilibrium height of

the coils is expected to be close to the radius of gyration of the molecules. In the thiol modified DNA molecules case, the AFM result shows that circular shape bundles of the DNA probes about 14 nm diameters covered the surface. Using contact mode in AFM, the DNA layer was partially removed over an area and the surface revealed the thickness of the layer ( $\sim 2.2$  nm). Considering the contour length of the 8-base ssDNA molecules and the fact that 8-base DNA oligos behave as rod-like molecules, the DNA probes lie at an angle of  $\sim 28.4^\circ$  with respect to the surface of the GaAs. Similarly to the non-modified DNA case, the thiolated DNA bundles orient along the trenches in the 2x direction of the GaAs (2 x 4) reconstructed surface.

To achieve a better quality layer of the brush-like structure MCH method was employed to the immobilized ssDNA layer. After MCH treatment, the height of the layer was increased by approximately 1nm as characterized by AFM. XPS results shows reduction the bonded nitrogen and oxygen peaks after MCH treatment. These results indicated that the sulfur in MCH substituted the nitrogen- and oxygen – for bonding with arsenic atoms. The MCH treatment provided a brush-like layer with the oligos at a higher angle with respect to the surface of the GaAs by displacing the non-specific bonds and/or adsorption.

When the DNA probes are immersed in solution, their behavior is complicated because of the complexity of interpreting the electrostatic interaction within the polyelectrolyte brush and the effects of the counterions from the added salt. As a result, the morphology of the polyelectrolyte strongly depends on concentration of added salt

and the elasticity of the polyelectrolyte. Namely the energy balance is to describe the behavior of the polyelectrolyte layer (ssDNA probes layer in this work) is a function of counterion osmotic pressure and chain elasticity as proposed by Pincus in 1991. Without or for very low concentration of salts in a good solvent, such as water, the DNA layer swells and stretches as a result of the counterion entropy or osmotic pressure. The fluid cell AFM results obtained in this work shows that the height of the layer increased in solution compare to dry form. This direct observation of conformational change is important to understand an efficiency of hybridization. Electrostatic repulsion between the DNA by a negative charge in the backbone of DNA probes could affect hybridization in low salt concentration because of the reduced accessibility of the target molecules to the probes. On the other hand, under high concentration of salt, the screening of the counterions reduces the osmotic pressure. Pincus proposed that the polyelectrolyte brush collapses as the salt concentration increases (  $L \approx C_s^{-1/3}$  ) (see Table 3.2). Therefore, a design of a biosensor with better efficiency for hybridization should consider an appropriate the concentration of salt.

In this work, long (100-base) of DNA was also studied to investigate if the morphology of a longer molecules in dry mode and in solution was the same as for the shorten oligos. For designing a biochip, optimization of the length of the immobilized DNA probes has to be addressed. In theory, a longer, a molecule carries more genomic information. Also, it is easier for a long probe DNA to identify and bind to the target DNA. Furthermore, the stability of the system after hybridization

would be higher. However, higher probe surface coverage reduces the distance between neighbor tethered molecules thus increasing the length of the DNA because the DNA molecules behave like flexible chains instead of rod-shape. Also, increasing probe length gives rise to increase of entropic penalty associated with ordering structure. Our AFM results reveal that for long DNA relatively big size of clusters as well as small bundles of DNA covered the surface of the GaAs. The size and shape of clusters were relatively regular. That indicates that the system is in there are some equilibrium. This equilibrium could depend on factors, such as hydrophobicity and  $\pi$ - $\pi$  interaction. To get a better understanding of the behavior of long DNA tethered at one end, further studies should be performed including low concentration of DNA solution, determination of the radius of gyration of the DNA molecules in solution, and the quality of the DNA solution. At this moment, I can only expected that  $\pi$ - $\pi$  stacking interaction is the dominant interaction because of the increasing in the number of bases and aromatic rings. Even though MCH effects will be insensitive as the length of the molecules increases, I observed MCH influence to the height of ssDNA layer. The level of the collapse was higher than for short DNA at in high salt concentration.

In the preliminary experiments for possible applications of DNA anchored to GaAs for biosensors, the effect of irradiation was observed by AFM. After irradiation of the ssDNA layer, the surface became smother indicating complete collapse of the DNA layer. In addition, valleys were found during the AFM scan in water. The valleys could be the result of the removal of DNA from the surface because the S-As

bonds were broken by strong radiation energy. This change can be detected using DNA biosensor. Using an AlGaAs disk resonator, 10fmol of the 8-base target DNA was detected. This preliminary result shows that a very low mass change due to hybridization can be detected by AlGaAs resonator.

## Chapter 6.

### 6. Suggestions for Future Work

In this work, I investigated the morphology immobilized DNA probes on GaAs-based semiconductors in dry form and in solution and its application. Additional studies for the understanding of this system could be achieved by employing other characterization techniques, such as neutron reflectivity (NR), transmission electron microscopy (TEM), and ellipsometry. Neutron reflectivity (NR) could be used to provide in depth understanding of the attachment and density profile of the DNA at the surface in an aqueous environment [116]. NR can provide high resolution information on the density profile normal to the substrate surface (1 nm resolution or better) and through the use of D<sub>2</sub>O can provide better contrast between the DNA chains and the aqueous environment than with comparable experiments using x-rays. In particular, NR can reveal how far the DNA extends into the solution which will allow comparison to the expected extension for DNA molecules and allow the determination of whether the DNA is collapsed as the result of nonspecific bonding with the surface. In addition, NR can provide insight into the role of the MCH spacer in lifting the DNA off the surface by potentially minimizing the existing nonspecific interactions between the DNA and the surface. The neutron data will complement the x-ray data. Finally, NR may provide some insight into the DNA hybridization and the effect of MCH on this process. The density profile measured by NR should be changed by the hybridization process and this data will be useful in the

evaluation of the DNA attachment to GaAs as a route to the fabrication of a DNA chip. The NR data will complement the AFM, GIXS and XPS results and provide a more complete picture of the attachment process and enable the transformation of this research into practical applications.

To obtain more detailed, structural information, TEM could be used. For the TEM studies, both plan view and cross section samples should be prepared to obtain complementary information. However, the preparation of the TEM samples will be challenging since the samples have a very soft organic (DNA) material on a relatively hard inorganic (semiconductor) material. Cryotechniques for TEM sample could also be used to reduce the damage caused by the electron beam. Also, for greater contrast of TEM images, M-DNA could be used. M-DNA is a type of metalated DNA containing Zn, Ni, and Co, with the metals placed in between each base pair [118, 119]. Some preliminary results of TEM images and diffraction patterns from 8-base DNA samples are presented in the appendix.

Ellipsometry is a highly sensitive optical technique for surface information and thin films. The shape and orientation of the ellipse strongly depend in the angle of incidence and the reflection of the light. Ellipsometry gives thickness information of the thin film on the surface when the reflection properties, thickness or chemical composition, are changed [120, 121].

Some preliminary results using short length DNA were obtained using AlGaAs resonator in this study. This type of biosensor should be studied in more detail with different lengths of DNA. In addition, as discussed in chapter 4.2, the effect of irradiation on the DNA layer should be applied to the AlGaAs resonator technique. Finally, the study for the design of *in-situ* detection solution should be carried out for next generation of DNA biosensor.

## Appendices A

Some example of XPS spectra for As under different conditions are presented below

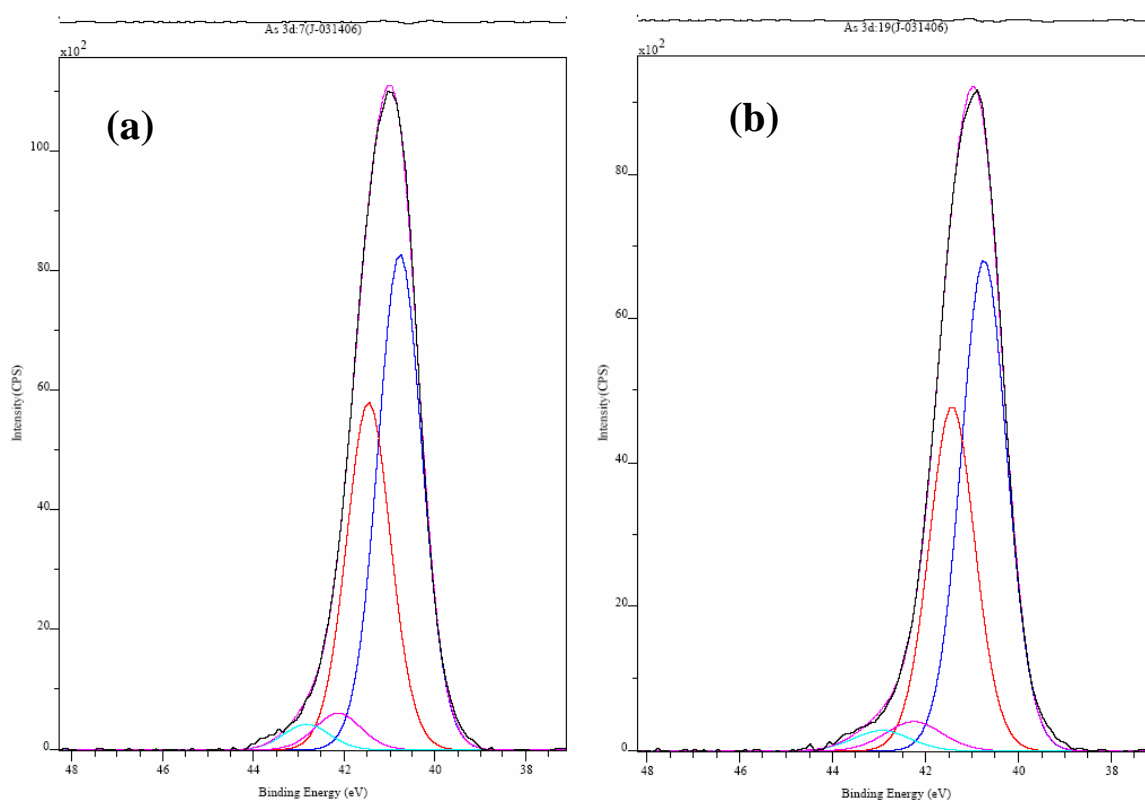


Figure A.1 High resolution XPS As 3d spectrum before (a) and after (b) immersion in acetone for 30 minutes of the immobilized 8-base ssDNA layer on GaAs substrate.

No appreciable change is observed.

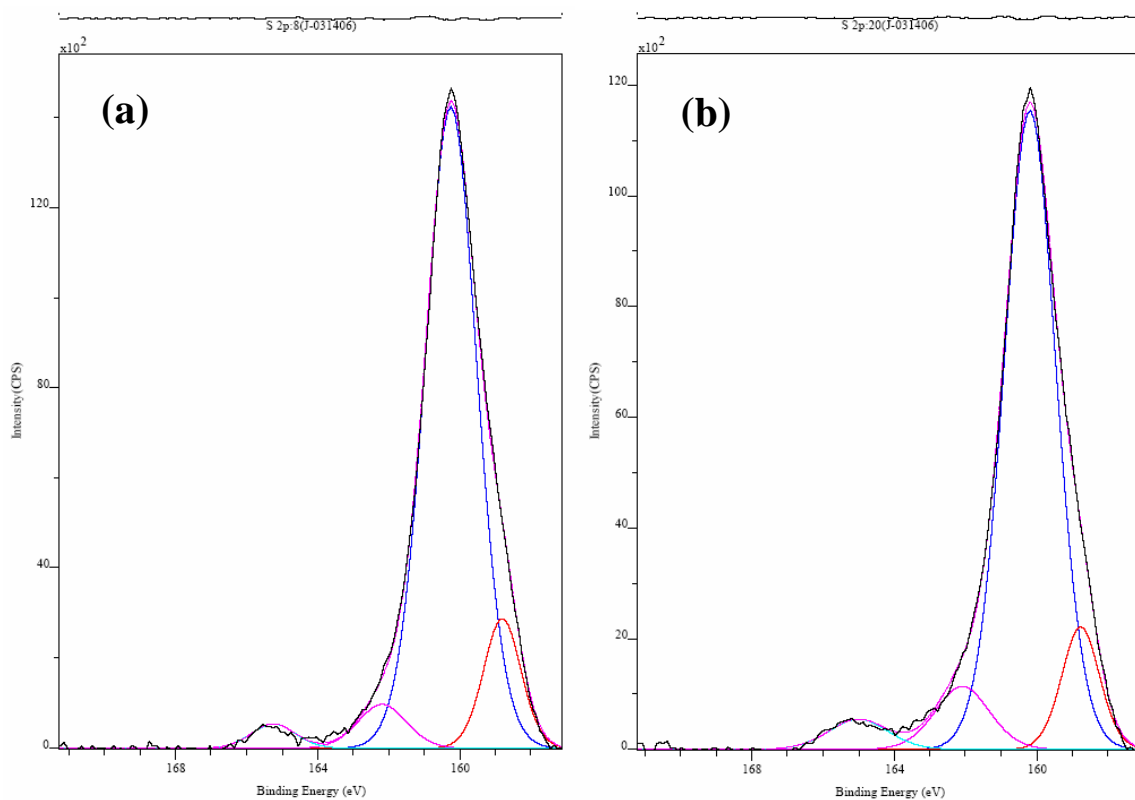


Figure A.2 High resolution XPS S 2p spectrum before (a) and after (b) immersion acetone for 30 minutes of the immobilized 8-base ssDNA (60  $\mu\text{M}$ ) layer on GaAs substrate. No appreciable change is observed.

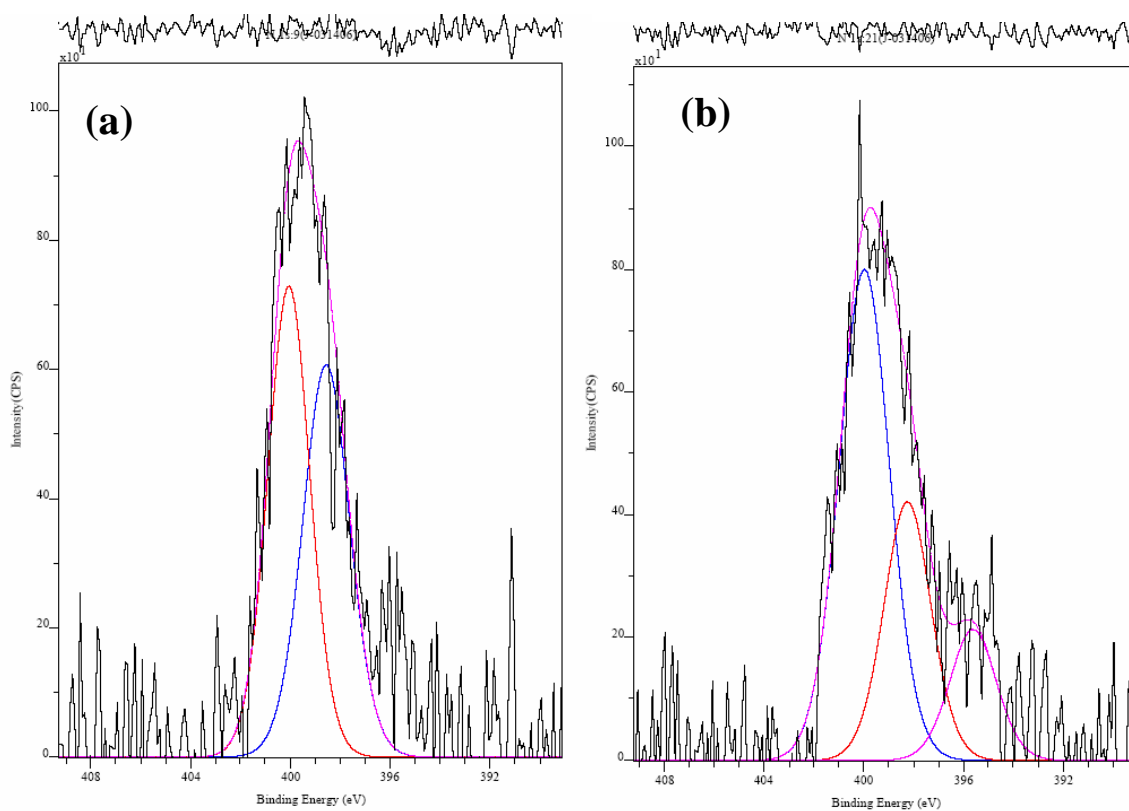


Figure A.3 High resolution XPS S 2p spectrum before (a) and after (b) immersion acetone for 30 minutes of the immobilized 8-base ssDNA (60  $\mu\text{M}$ ) layer on GaAs substrate. Some change is observed in the relative intensities of the high and low energy peaks.

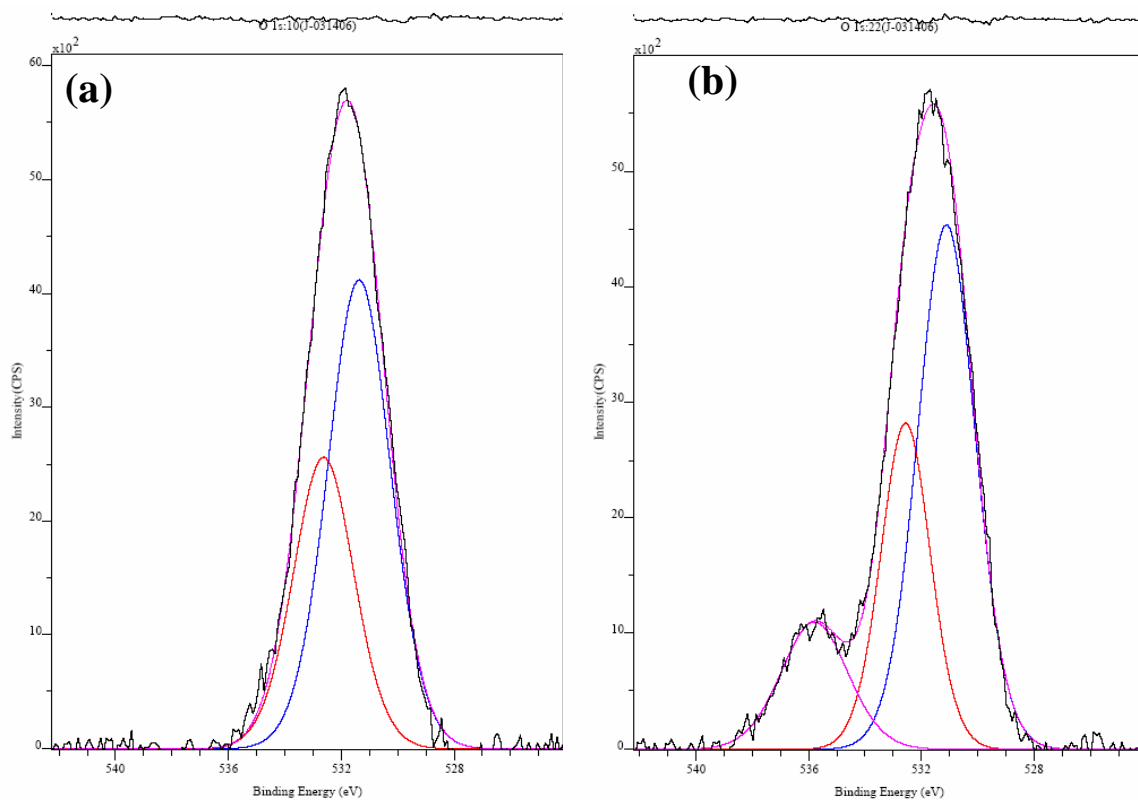


Figure A.4 High resolution XPS O 1s spectrum before (a) and after (b) immersion acetone for 30 minutes of the immobilized 8-base ssDNA (60  $\mu$ M) layer on GaAs substrate. A new peak is observed at  $\sim$  536 eV after immersion in acetone. This peak is probably due to C=O bond of acetone.

**(a)**

Peak	Position BE (eV)	FWHM (eV)	Raw Area (CPS)	RSF	Atomic Mass	Atomic Conc %	Mass Conc %
As 3d a 5/2	40.780	1.125	10287.4	0.745	74.922	5.41	18.17
As 3d a 3/2	41.470	1.125	7201.2	0.745	74.922	3.79	12.72
As 3d b 5/2	42.138	1.172	792.3	0.745	74.922	0.42	1.40
As 3d b 3/2	42.828	1.172	554.6	0.745	74.922	0.29	0.98
S 2p a	160.251	1.689	26408.3	0.723	32.065	14.40	20.68
S 2p b	158.805	1.218	3872.1	0.723	32.065	2.11	3.03
S 2p ( good )	162.195	1.582	1706.2	0.723	32.065	0.93	1.34
S 2p d	165.279	1.434	863.1	0.723	32.065	0.47	0.68
N 1s a	398.594	2.172	1452.8	0.505	14.007	1.18	0.74
N 1s b	400.074	1.954	1567.5	0.505	14.007	1.28	0.80
O 1s a	531.406	2.580	11704.5	0.736	15.999	6.87	4.92
O 1s b	532.659	2.490	7020.6	0.736	15.999	4.12	2.96
C 1s a	284.600	1.499	20911.2	0.318	12.011	26.29	14.14
C 1s b	281.727	2.994	14346.4	0.318	12.011	18.03	9.70
C 1s c	286.198	2.253	8020.8	0.318	12.011	10.09	5.43
C 1s d	288.345	2.304	3420.5	0.318	12.011	4.30	2.32

**(b)**

Peak	Position BE (eV)	FWHM (eV)	Raw Area (CPS)	RSF	Atomic Mass	Atomic Conc %	Mass Conc %
As 3d a 5/2	40.752	1.147	8618.5	0.745	74.922	4.76	16.77
As 3d a 3/2	41.443	1.147	6032.8	0.745	74.922	3.33	11.74
As 3d b 5/2	42.258	1.414	636.5	0.745	74.922	0.35	1.24
As 3d b 3/2	42.948	1.414	445.8	0.745	74.922	0.25	0.87
S 2p a	160.205	1.687	21418.4	0.723	32.065	12.25	18.48
S 2p b	158.761	1.226	2991.6	0.723	32.065	1.71	2.58
S 2p good	162.115	1.769	2221.2	0.723	32.065	1.27	1.92
S 2p c	165.043	1.920	1157.5	0.723	32.065	0.66	1.00
N 1s a	399.978	2.344	2058.3	0.505	14.007	1.76	1.16
N 1s b	398.282	2.179	1010.7	0.505	14.007	0.86	0.57
N 1s c	395.638	2.174	510.4	0.505	14.007	0.43	0.29
O 1s a	531.113	2.380	11863.6	0.736	15.999	7.30	5.50
O 1s b	532.591	2.034	6326.0	0.736	15.999	3.90	2.93
O 1s c	535.829	2.763	3350.1	0.736	15.999	2.07	1.56
C 1s a	284.600	1.583	21836.7	0.318	12.011	28.79	16.27
C 1s b	281.636	2.922	11044.5	0.318	12.011	14.56	8.23
C 1s c	288.535	2.156	7335.6	0.318	12.011	9.68	5.47
C 1s d	286.494	1.708	4604.8	0.318	12.011	6.07	3.43

Table A.1 Quantification report before (a) and after (b) immersion acetone for 30 minutes of the immobilized 8-base ssDNA (60  $\mu$ M) layer on GaAs substrate.

## Appendices B

### Preliminary Results using TEM

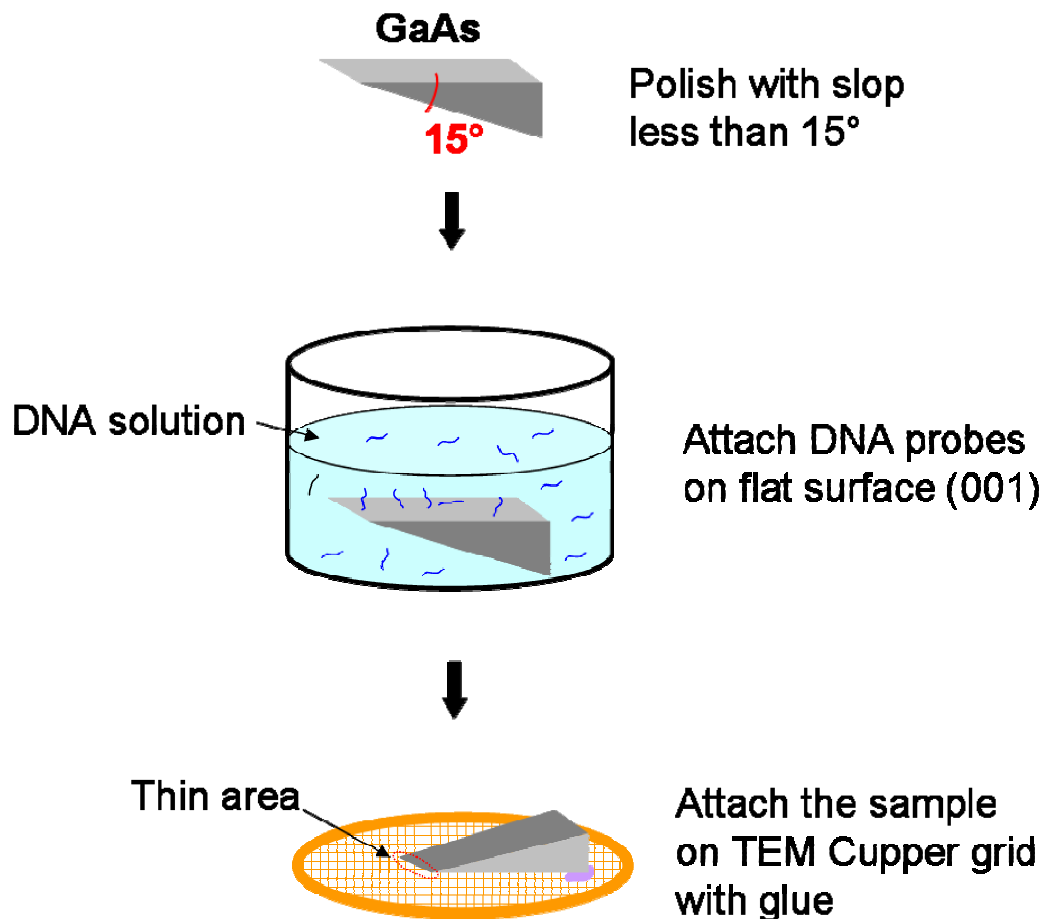


Figure B.1 Schematic representation of the procedure followed for preparing edge specimens

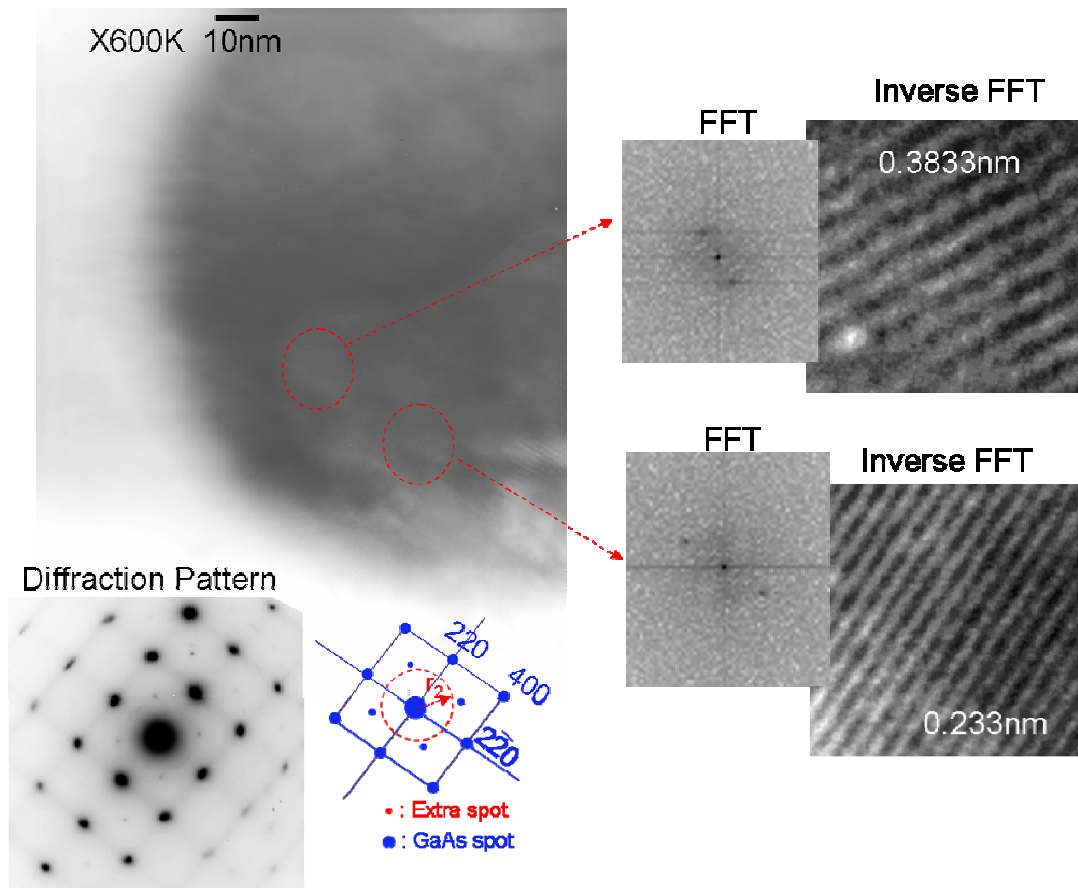


Figure B.2 High resolution TEM image of the immobilized 8-base ssDNA (60  $\mu$ M) layer on GaAs substrate. Diffraction pattern shows extra spot besides the GaAs spots. The Fast Fourier Transforms show two different line spacing.

## References

1. Alexander, S., *Polymer Adsorption on Small Spheres - Scaling Approach*. Journal De Physique, 1977. **38**(8): p. 977-981.
2. Pincus, P., *Colloid Stabilization with Grafted Polyelectrolytes*. Macromolecules, 1991. **24**(10): p. 2912-2919.
3. Crick, F.H.C., *The Complementary Structure of DNA*. Proceedings of the National Academy of Sciences of the United States of America, 1954. **40**(8): p. 756-758.
4. Patil, S.A., V.S. Gomase, and K.V. Kale, *DNA electronics: A nanotechnology approach*. Current Nanoscience, 2007. **3**(2): p. 161-165.
5. Jiang, L., et al., *Self-assembled molecular electronic devices*. Progress in Chemistry, 2005. **17**(1): p. 172-179.
6. Hush, N.S., *An overview of the first half-century of molecular electronics*. Molecular Electronics Iii, 2003. **1006**: p. 1-20.
7. Kohata, N., et al., *Evolutionary computation for intelligent agents based on chaotic retrieval and soft DNA*. Simulated Evolution and Learning, 1999. **1585**: p. 251-259.
8. Dubois, L.H., *Self-Assembled Monolayers as Models for Organic-Surfaces*. Abstracts of Papers of the American Chemical Society, 1992. **204**: p. 92-Phys.
9. Hyndman, D., et al., *Protein Immobilization to Alumina Supports .I. Characterization of Alumina-Organophosphate Ligand Interactions and Use in the Attachment of Papain*. Biotechnology and Bioengineering, 1992. **40**(11): p. 1319-1327.
10. Boland, T. and B.D. Ratner, *2-Dimensional Assembly of Purines and Pyrimidines on Au(111)*. Langmuir, 1994. **10**(10): p. 3845-3852.
11. Zimmermann, R.M. and E.C. Cox, *DNA Stretching on Functionalized Gold Surfaces*. Nucleic Acids Research, 1994. **22**(3): p. 492-497.
12. Peterlinz, K.A., et al., *Observation of hybridization and dehybridization of thiol-tethered DNA using two-color surface plasmon resonance spectroscopy*. Journal of the American Chemical Society, 1997. **119**(14): p. 3401-3402.
13. Levicky, R., et al., *Using self-assembly to control the structure of DNA monolayers on gold: A neutron reflectivity study*. Journal of the American Chemical Society, 1998. **120**(38): p. 9787-9792.

14. Yang, M.S., H.C.M. Yau, and H.L. Chan, *Adsorption kinetics and ligand-binding properties of thiol-modified double-stranded DNA on a gold surface*. Langmuir, 1998. **14**(21): p. 6121-6129.
15. Sheen, C.W., et al., *A New Class of Organized Self-Assembled Monolayers - Alkane Thiols on Gaas(100)*. Journal of the American Chemical Society, 1992. **114**(4): p. 1514-1515.
16. Zhao, Y.D., et al., *DNA-modified electrodes .2. Electrochemical characterization of gold electrodes modified with DNA*. Journal of Electroanalytical Chemistry, 1997. **431**(2): p. 203-209.
17. Strother, T., et al., *Synthesis and characterization of DNA-modified silicon (111) surfaces*. Journal of the American Chemical Society, 2000. **122**(6): p. 1205-1209.
18. Strother, T., R.J. Hamers, and L.M. Smith, *Covalent attachment of oligodeoxyribonucleotides to amine-modified Si (001) surfaces*. Nucleic Acids Research, 2000. **28**(18): p. 3535-3541.
19. Linford, M.R., et al., *Alkyl Monolayers on Silicon Prepared from 1-Alkenes and Hydrogen-Terminated Silicon*. Journal of the American Chemical Society, 1995. **117**(11): p. 3145-3155.
20. Yang, M.S., et al., *Covalent immobilization of oligonucleotides on modified glass/silicon surfaces for solid-phase DNA hybridization and amplification*. Chemistry Letters, 1998(3): p. 257-258.
21. Mohaddes-Ardabili, L., et al., *Attachment of DNA probes on gallium arsenide surface*. Applied Physics Letters, 2003. **83**(1): p. 192-194.
22. Nuzzo, R.G. and D.L. Allara, *Adsorption of Bifunctional Organic Disulfides on Gold Surfaces*. Journal of the American Chemical Society, 1983. **105**(13): p. 4481-4483.
23. Nelles, G., et al., *Two-dimensional structure of disulfides and thiols on gold(111)*. Langmuir, 1998. **14**(4): p. 808-815.
24. Bain, C.D. and G.M. Whitesides, *Formation of Monolayers by the Coadsorption of Thiols on Gold - Variation in the Length of the Alkyl Chain*. Journal of the American Chemical Society, 1989. **111**(18): p. 7164-7175.
25. Bain, C.D., et al., *Formation of Monolayer Films by the Spontaneous Assembly of Organic Thiols from Solution onto Gold*. Journal of the American Chemical Society, 1989. **111**(1): p. 321-335.

26. Bain, C.D., H.A. Biebuyck, and G.M. Whitesides, *Comparison of Self-Assembled Monolayers on Gold - Coadsorption of Thiols and Disulfides*. Langmuir, 1989. **5**(3): p. 723-727.
27. Herne, T.M. and M.J. Tarlov, *Characterization of DNA probes immobilized on gold surfaces*. Journal of the American Chemical Society, 1997. **119**(38): p. 8916-8920.
28. Steel, A.B., et al., *Immobilization of nucleic acids at solid surfaces: Effect of oligonucleotide length on layer assembly*. Biophysical Journal, 2000. **79**(2): p. 975-981.
29. Gennes, P.G.D., *Stabilization of Foams by Polymer-Solutions*. Comptes Rendus Hebdomadaires Des Seances De L Academie Des Sciences Serie B, 1979. **289**(5): p. 103-106.
30. Hariharan, R., C. Biver, and W.B. Russel, *Ionic strength effects in polyelectrolyte brushes: The counterion correction*. Macromolecules, 1998. **31**(21): p. 7514-7518.
31. Hariharan, R., et al., *Ionic strength and curvature effects in flat and highly curved polyelectrolyte brushes*. Macromolecules, 1998. **31**(21): p. 7506-7513.
32. Ruth, J., R.D. Smith, and R. Lohrmann, *DNA Affinity Supports Using Modified Oligonucleotides Attached to Nylon Membranes*. Federation Proceedings, 1985. **44**(5): p. 1622-1622.
33. Kainz, P. and V. Kainz, *Nick Translation of DNA Immobilized on Nylon Membranes*. Analytical Biochemistry, 1989. **178**(2): p. 260-262.
34. Hopp, H.E., et al., *Development and Application of a Nonradioactive Nucleic-Acid Hybridization System for Simultaneous Detection of 4 Potato Pathogens*. Journal of Virological Methods, 1991. **31**(1): p. 11-29.
35. Gillmann, T. and T. Weeber, *Silver Oxide-Assisted Palladium-Catalyzed Cross-Coupling of Methyl 2-Halo-2,3-Butadienoates with Arylboronic Acids*. Synlett, 1994(8): p. 649-650.
36. Kinoshita, N., et al., *Interaction between dental metals and antioxidants, assessed by cytotoxicity assay and ESR spectroscopy*. Anticancer Research, 2002. **22**(6C): p. 4017-4022.
37. Chen, Z.H., et al., *Applications of silicon nanowires functionalized with palladium nanoparticles in hydrogen sensors*. Nanotechnology, 2007. **18**(34): p. -.

38. Schepinov, M.S., et al., *Selectively Cleavable Synthetic Oligodeoxyribonucleotides for the Reversible Immobilization of DNA*. Bioorganicheskaya Khimiya, 1994. **20**(8-9): p. 955-966.
39. Caruso, F., et al., *Quartz crystal microbalance study of DNA immobilization and hybridization for nucleic acid sensor development*. Analytical Chemistry, 1997. **69**(11): p. 2043-2049.
40. Ueda, M., et al., *Atomic force microscopy observation of deoxyribonucleic acid stretched and anchored onto aluminum electrodes*. Japanese Journal of Applied Physics Part 1-Regular Papers Short Notes & Review Papers, 1999. **38**(4A): p. 2118-2119.
41. Kim, J.M., et al., *Near-field optical imaging of abasic sites on a single DNA molecule*. Febs Letters, 2003. **555**(3): p. 611-615.
42. Pang, D.W., et al., *Modification of glassy carbon and gold electrodes with DNA*. Journal of Electroanalytical Chemistry, 1996. **403**(1-2): p. 183-188.
43. Yan, F., et al., *Electrochemical DNA biosensor for the detection of specific gene related to Microcystis species*. Electrochemistry Communications, 2001. **3**(5): p. 224-228.
44. Tombelli, S., G. Marrazza, and M. Mascini, *Recent advances on DNA biosensors*. International Journal of Environmental Analytical Chemistry, 2001. **80**(2): p. 87-99.
45. Kertesz, V., et al., *Surface titration of DNA-modified gold electrodes with a thiol-tethered anthraquinone*. Journal of Electroanalytical Chemistry, 2000. **493**(1-2): p. 28-36.
46. Huang, E., et al., *Surface structure and coverage of an oligonucleotide probe tethered onto a gold substrate and its hybridization efficiency for a polynucleotide target*. Langmuir, 2001. **17**(4): p. 1215-1224.
47. Holmberg, M., et al., *Hybridisation of short DNA molecules investigated with in situ atomic force microscopy*. Ultramicroscopy, 2003. **97**(1-4): p. 257-261.
48. Chrisey, L.A., G.U. Lee, and C.E. OFerrall, *Covalent attachment of synthetic DNA to self-assembled monolayer films*. Nucleic Acids Research, 1996. **24**(15): p. 3031-3039.
49. Morozov, V.N., et al., *New polyacrylamide gel-based methods of sample preparation for optical microscopy: Immobilization of DNA molecules for optical mapping*. Journal of Microscopy-Oxford, 1996. **183**: p. 205-214.

50. Rogers, Y.H., et al., *Immobilization of oligonucleotides onto a glass support via disulfide bonds: A method for preparation of DNA microarrays*. Analytical Biochemistry, 1999. **266**(1): p. 23-30.
51. Decher, G., et al., *New Nanocomposite Films for Biosensors - Layer-by-Layer Adsorbed Films of Polyelectrolytes, Proteins or DNA*. Biosensors & Bioelectronics, 1994. **9**(9-10): p. 677-684.
52. Jenison, R., et al., *Interference-based detection of nucleic acid targets on optically coated silicon*. Nature Biotechnology, 2001. **19**(1): p. 62-65.
53. Cavic, B.A., et al., *High surface density immobilization of oligonucleotide on silicon*. Analyst, 2001. **126**(4): p. 485-490.
54. Lenigk, R., et al., *Surface characterization of a silicon-chip-based DNA microarray*. Langmuir, 2001. **17**(8): p. 2497-2501.
55. Sun, B., et al., *Single crystal silicon surface as a novel substrate of gene-chip*. Acta Physico-Chimica Sinica, 2002. **18**(7): p. 581-584.
56. Zhu, X.Y., *Organic monolayers on silicon: Microprinting, micromachines, and microarrays*. Acta Physico-Chimica Sinica, 2002. **18**(9): p. 855-864.
57. Deng, C.H., M.H. Shen, and C.X. Zhao, *Covalent immobilization of oligonucleotides onto solid substrates in the manufacturing of DNA chips*. Chinese Journal of Organic Chemistry, 2002. **22**(12): p. 943-950.
58. Manning, M., et al., *A versatile multi-platform biochip surface attachment chemistry*. Materials Science & Engineering C-Biomimetic and Supramolecular Systems, 2003. **23**(3): p. 347-351.
59. Charles, P.T., et al., *Fabrication and surface characterization of DNA microarrays using amine- and thiol-terminated oligonucleotide probes*. Langmuir, 2003. **19**(5): p. 1586-1591.
60. Volle, J.N., et al., *Enhanced sensitivity detection of protein immobilization by fluorescent interference on oxidized silicon*. Biosensors & Bioelectronics, 2003. **19**(5): p. 457-464.
61. Jin, L., A. Horgan, and R. Levicky, *Preparation of end-tethered DNA monolayers on siliceous surfaces using heterobifunctional cross-linkers*. Langmuir, 2003. **19**(17): p. 6968-6975.
62. Soderkvist, J. and K. Hjort, *The Piezoelectric Effect of Gaas Used for Resonators and Resonant Sensors*. Journal of Micromechanics and Microengineering, 1994. **4**(1): p. 28-34.

63. Beck, R.G., et al., *Measuring the mechanical resonance of a GaAs/AlGaAs cantilever using a strain-sensing field-effect transistor*. Semiconductor Science and Technology, 1998. **13**(8A): p. A83-a85.
64. Choi, J.R. and S. Park, *Integration of sensors and GaAs electronic circuits on a single chip*. Mechatronics, 1998. **8**(5): p. 441-458.
65. Mohaddes-Ardabili, L., et al., *Preferred orientation of DNA oligonucleotide probes on the (2x4) reconstructed surface of (001)GaAs (vol 95, pg 6021, 2004)*. Journal of Applied Physics, 2005. **97**(1): p. -.
66. Mohaddes-Ardabili, L., et al., *Preferred orientation of DNA oligonucleotide probes on the (2x4) reconstructed surface of (001) GaAs*. Journal of Applied Physics, 2004. **95**(11): p. 6021-6024.
67. Al-Sheikhly, M., et al., *Radiation-induced failure mechanisms of GaAs-Based biochips*. Ieee Transactions on Device and Materials Reliability, 2004. **4**(2): p. 192-197.
68. Haga, Y., S. Miwa, and E. Morita, *Fine-Structure of the Gaas(001) Surface*. Journal of Vacuum Science & Technology B, 1994. **12**(3): p. 2107-2110.
69. Jiang, X.P., et al., *Chemiluminescent biosensor for nucleic acid*. Chinese Journal of Analytical Chemistry, 2000. **28**(1): p. 12-16.
70. Cai, X.H., et al., *Evaluation of different carbon electrodes for adsorptive stripping analysis of nucleic acids*. Electroanalysis, 1996. **8**(8-9): p. 753-758.
71. Dill, K., S.D.H. Chan, and T.W. Gibbs, *Detection of plasmids using DNA and RNA probes and the light-addressable potentiometric sensor*. Journal of Biochemical and Biophysical Methods, 1997. **35**(3): p. 197-202.
72. Wang, J., et al., *Carbon fiber microelectrodes for adsorptive stripping analysis of trace nucleic acids*. Journal of Electroanalytical Chemistry, 1998. **441**(1-2): p. 167-172.
73. Fan, C.H., et al., *Voltammetric response and determination of DNA with a silver electrode*. Analytical Biochemistry, 1999. **271**(1): p. 1-7.
74. Ozsoz, M., et al., *Electrochemical biosensor for the detection of interaction between arsenic trioxide and DNA based on guanine signal*. Electroanalysis, 2003. **15**(7): p. 613-619.
75. Vanickova, M., M. Buckova, and J. Labuda, *Voltammetric determination of azepine and phenothiazine drugs with DNA biosensors*. Chemia Analityczna, 2000. **45**(1): p. 125-133.

76. La-Scalea, M.A., S.H.P. Serrano, and I.G.R. Gutz, *DNA-modified electrodes: A new alternative for electroanalysis*. *Quimica Nova*, 1999. **22**(3): p. 417-424.
77. Graham, C.R., D. Leslie, and D.J. Squirrell, *Gene Probe Assays on a Fiberoptic Evanescent Wave Biosensor*. *Biosensors & Bioelectronics*, 1992. **7**(7): p. 487-493.
78. Pandey, P.C. and H.H. Weetall, *Detection of Aromatic-Compounds Based on DNA Intercalation Using an Evanescent-Wave Biosensor*. *Analytical Chemistry*, 1995. **67**(5): p. 787-792.
79. Hutchinson, A.M., *Evanescent-Wave Biosensors - Real-Time Analysis of Biomolecular Interactions*. *Molecular Biotechnology*, 1995. **3**(1): p. 47-54.
80. Stimpson, D.I., et al., *Real-Time Detection of DNA Hybridization and Melting on Oligonucleotide Arrays by Using Optical-Wave Guides*. *Proceedings of the National Academy of Sciences of the United States of America*, 1995. **92**(14): p. 6379-6383.
81. Mauro, J.M., et al., *Fiber-optic fluorometric sensing of polymerase chain reaction-amplified DNA using an immobilized DNA capture protein*. *Analytical Biochemistry*, 1996. **235**(1): p. 61-72.
82. Abel, A.P., et al., *Fiber-optic evanescent wave biosensor for the detection of oligonucleotides*. *Analytical Chemistry*, 1996. **68**(17): p. 2905-2912.
83. Lim, D.V., *Detection of microorganisms and toxins with evanescent wave fiber-optic biosensors*. *Proceedings of the Ieee*, 2003. **91**(6): p. 902-907.
84. Rolfe, P., F. Scopesi, and G. Serra, *Advances in fibre-optic sensing in medicine and biology*. *Measurement Science & Technology*, 2007. **18**(6): p. 1683-1688.
85. Nilsson, P., et al., *Real-Time Monitoring of DNA Manipulations Using Biosensor Technology*. *Analytical Biochemistry*, 1995. **224**(1): p. 400-408.
86. Kruchinin, A.A. and Y.G. Vlasov, *Surface plasmon resonance monitoring by means of polarization state measurement in reflected light as the basis of a DNA-probe biosensor*. *Sensors and Actuators B-Chemical*, 1996. **30**(1): p. 77-80.
87. Gambari, R., et al., *Surface plasmon resonance for real-time detection of molecular interactions between chromomycin and target DNA sequences*. *International Journal of Oncology*, 1997. **11**(1): p. 145-149.

88. Healey, B.G., R.S. Matson, and D.R. Walt, *Fiberoptic DNA sensor array capable of detecting point mutations*. Analytical Biochemistry, 1997. **251**(2): p. 270-279.
89. Rutigliano, C., et al., *Surface plasmon resonance for real-time monitoring of molecular interactions between a triple helix forming oligonucleotide and the Sp1 binding sites of human Ha-ras promoter: Effects of the DNA-binding drug chromomycin*. International Journal of Oncology, 1998. **12**(2): p. 337-343.
90. Mariotti, E., M. Minunni, and M. Mascini, *Surface plasmon resonance biosensor for genetically modified organisms detection*. Analytica Chimica Acta, 2002. **453**(2): p. 165-172.
91. Shimizu, M., et al., *Self-assembly of electron transport protein using oligonucleotide hybridization*. Colloids and Surfaces B-Biointerfaces, 2002. **25**(1): p. 69-79.
92. Wang, R.H., et al., *Immobilisation of DNA probes for the development of SPR-based sensing*. Biosensors & Bioelectronics, 2004. **20**(5): p. 967-974.
93. Storri, S., T. Santoni, and M. Mascini, *A piezoelectric biosensor for DNA hybridisation detection*. Analytical Letters, 1998. **31**(11): p. 1795-1808.
94. Tombelli, S., et al., *Coupling of a DNA piezoelectric biosensor and polymerase chain reaction to detect apolipoprotein E polymorphisms*. Biosensors & Bioelectronics, 2000. **15**(7-8): p. 363-370.
95. Mannelli, I., et al., *Quartz crystal microbalance (QCM) affinity biosensor for genetically modified organisms (GMOs) detection*. Biosensors & Bioelectronics, 2003. **18**(2-3): p. 129-140.
96. Minunni, M., *Biosensors based on nucleic acid interaction*. Spectroscopy-an International Journal, 2003. **17**(2-3): p. 613-625.
97. Skladal, P., et al., *Piezoelectric biosensors for real-time monitoring of hybridization and detection of hepatitis C virus*. Journal of Virological Methods, 2004. **117**(2): p. 145-151.
98. Mannelli, F., et al., *Direct immobilisation of DNA probes for the development of affinity biosensors*. Bioelectrochemistry, 2005. **66**(1-2): p. 129-138.
99. Kumar, P., et al., *Fabrication of piezoelectric Al<sub>0.3</sub>Ga<sub>0.7</sub>As microstructures*. Sensors and Actuators a-Physical, 2004. **115**(1): p. 96-103.
100. Li, L., et al., *Piezoelectric AlGaAs bimorph microactuators*. Journal of Micromechanics and Microengineering, 2006. **16**(5): p. 1062-1066.

101. Deng, K., et al., *Piezoelectric disk resonators based on epitaxial AlGaAs films*. Journal of Microelectromechanical Systems, 2007. **16**(1): p. 155-162.
102. Rickert, J., et al., *A new affinity biosensor: Self-assembled thiols as selective monolayer coatings of quartz crystal microbalances*. Biosensors & Bioelectronics, 1996. **11**(6-7): p. 591-598.
103. Hunter, C.A., *Sequence-Dependent DNA-Structure - the Role of Base Stacking Interactions*. Journal of Molecular Biology, 1993. **230**(3): p. 1025-1054.
104. Matta, C.F., N. Castillo, and R.J. Boyd, *Extended weak bonding interactions in DNA: pi-stacking (base-base), base-backbone, and backbone-backbone interactions*. Journal of Physical Chemistry B, 2006. **110**(1): p. 563-578.
105. Szeri, A.J., et al., *Heat and mass transfer during the violent collapse of nonspherical bubbles*. Physics of Fluids, 2003. **15**(9): p. 2576-2586.
106. Krefting, D., R. Mettin, and W. Lauterborn, *High-speed observation of acoustic cavitation erosion in multibubble systems*. Ultrasonics Sonochemistry, 2004. **11**(3-4): p. 119-123.
107. Arivuoli, D., et al., *Nanoindentation studies of MOVPE grown GaAs/InP heterostructures*. Materials Chemistry and Physics, 2000. **66**(2-3): p. 207-212.
108. Patriarche, G. and E. Le Bourhis, *Nanoindentation of GaAs compliant substrates*. Philosophical Magazine a-Physics of Condensed Matter Structure Defects and Mechanical Properties, 2000. **80**(12): p. 2899-2911.
109. Grau, P., D. Lorenz, and A. Zeckzer, *Fundamentals of dislocation nucleation at nanoindentation*. Radiation Effects and Defects in Solids, 2002. **157**(6-12): p. 863-869.
110. Le Bourhis, E. and G. Patriarche, *Effects of annealing on the structure of GaAs(001) nanoindentations*. Philosophical Magazine Letters, 2003. **83**(3): p. 149-158.
111. Tinland, B., et al., *Persistence length of single-stranded DNA*. Macromolecules, 1997. **30**(19): p. 5763-5765.
112. Pezeshk, A., et al., *Electron addition to thymine dimers and related compounds: A mimic of natural repair*. Journal of Physical Chemistry, 1996. **100**(50): p. 19714-19718.
113. Aida, M., *Quantum chemical approach to radiation-induced DNA damage*. Seikagaku, 2000. **72**(12): p. 1417-1420.

114. Ilic, B., Y. Yang, and H.G. Craighead, *Virus detection using nanoelectromechanical devices*. Applied Physics Letters, 2004. **85**(13): p. 2604-2606.
115. Hara, M., et al., *Surface micromachined AlN thin film 2 GHz resonator for CMOS integration*. Sensors and Actuators a-Physical, 2005. **117**(2): p. 211-216.
116. Wu, J.C., et al., *Neutron and X-ray reflectivity studies on DNA adsorption on mixed DPPC/DC-cholesterol monolayers*. Physica B-Condensed Matter, 2006. **385-86**: p. 841-844.
117. DeVoe, D.L., *Piezoelectric thin film micromechanical beam resonators*. Sensors and Actuators a-Physical, 2001. **88**(3): p. 263-272.
118. Liu, B., et al., *Scanning electrochemical microscopy. 51. Studies of self-assembled monolayers of DNA in the absence and presence of metal ions*. Journal of Physical Chemistry B, 2005. **109**(11): p. 5193-5198.
119. Moreno-Herrero, F., et al., *Topographic characterization and electrostatic response of M-DNA studied by atomic force microscopy*. Nanotechnology, 2003. **14**(2): p. 128-133.
120. Legay, G., et al., *Measurements of thickness dispersion in bilayers by scanning force microscopy and comparison with spectroscopic ellipsometry analysis*. Ultramicroscopy, 2007. **107**(10-11): p. 1111-1117.
121. Bally, M., et al., *Optical microarray biosensing techniques*. Surface and Interface Analysis, 2006. **38**(11): p. 1442-1458.